

PHYSICAL LAYER RELIABILITY ASPECTS IN INDUSTRIAL OPTICAL  
WIRELESS COMMUNICATION

vorgelegt von  
M. Sc.  
Pablo Rafael Andreas Wilke Berenguer  
ORCID: 0000-0001-8624-576X

von der Fakultät IV - Elektrotechnik und Informatik  
der Technischen Universität Berlin  
zur Erlangung des akademischen Grades  
Doktor der Ingenieurwissenschaften  
-Dr.-Ing.-  
genehmigte Dissertation

Promotionsausschuss:

Vorsitzender:	Prof. Dr. rer. nat. Anatolij Zubow	(TU Berlin)
Gutachter:	Prof. Dr.-Ing. Ronald Freund	(TU Berlin)
Gutachter:	PD Dr. rer. nat. Volker Jungnickel	(TU Berlin)
Gutachter:	Professor Dominic O'Brien	(Oxford University)

Tag der wissenschaftlichen Aussprache: 14. Juni 2019

Berlin 2019



## PREFACE

---

The present work is a summary of research I conducted at Fraunhofer Heinrich Hertz Institute (HHI) between November 2015 and July 2018. I started working on the topic of optical wireless communication (OWC) in industrial production environments because PD Dr. rer. nat. Volker Jungnickel needed someone who would perform link-level simulations for the standardization activities in the IEEE P802.15 working group. After being introduced to this topic through simulations, however, I was intrigued by its potential in experimental analyses, which could in turn pave the way for the design and development of an OWC system suitable for reliable mobile communication in industrial production environments. Throughout my work I thus cared to identify the effects which most significantly compromise reliability of an OWC system and provide experimentally verified solutions to mitigate them. This mindset, I believe, is reflected in the structure of this thesis and explains its strong focus on experimental work.

For giving me the chance to work on this very interesting topic not only with a large portion of creative freedom, but also with well-served advisory help, I would like to express my deepest gratitude to PD Dr. rer. nat. Volker Jungnickel. Additional thanks go to him, Prof. Dr.-Ing. Ronald Freund and Professor Dominic O'Brien for taking time and sharing their expertise in reviewing this work.

Although he is not part of the team of reviewers, I would like to thank Dr.-Ing. Johannes Karl Fischer, who has taught me the proper analysis and presentation of research results in publications and at conferences. I also owe a very big *thank you* to all my other (temporary) colleagues at HHI. Although I will not mention each individually<sup>1</sup>, I cannot deny the help I have received through fruitful discussions, either during coffee or lunch breaks, project meetings, or business trips such as the multiple measurement series at BMW. I do, however, owe particular thanks to my colleagues from the electronics group Jonas Hilt and Peter Hellwig. Without their expertise, my design considerations for the optical front ends and combing circuitry discussed in this work, would have never left the realm of ideas and sketches. Among all colleagues, I would also like to pay my distinguished respects to Dr. Felix simply for the great times we have had so far in- and outside of HHI.

Outside the work environment, I would also like to thank my family, friends and flatmates, who have always successfully made sure that I could clear my mind even after long-lasting and tedious laboratory sessions. I cannot express how much I appreciate the loving and joyful environment they have provided throughout the years.

Within the present manuscript, the reader may notice an occasional use of the pronoun *we*. While their help and support are highly appreciated, this *we* does not attempt to incorporate my colleagues, but rather the reader. When suitable, I have thus made use of a less formal language, which hopefully

---

<sup>1</sup> Admittedly, this is in parts due to a preemptively felt fear of possibly forgetting someone.

allows to include the reader in my personal thought processes without the barrier of an omnipresent passive voice. With this being said, I wish the reader a pleasant read.

*Pablo Wilke Berenguer*  
Berlin, March 2019

## ABSTRACT

---

In the past centuries, production processes have impressively evolved from mostly hand-made goods of small quantities to almost fully automated large scale productions. Three significant jumps are commonly referred to as *industrial revolutions*, which have brought first mechanization, then electrification, and in this century, partial automation to the production processes. The currently ongoing step towards highly flexible, fully automated and interconnected factories is envisioned to be the fourth industrial revolution. For such factories, wireless communication systems, which support autonomous mobile units throughout the production sites, are expected to play an important role.

This thesis therefore discusses the use of optical wireless communication (OWC) as a wireless technology for industrial production environments. With this application, stringent requirements with respect to reliability and latency are imposed, which must be taken into account in the design of an OWC system. The content of this thesis thus focuses on aspects of the physical layer design, which are crucial for a reliable operation of an OWC system tailored to the needs of industrial wireless communication.

At first, known concepts of optical communication based on intensity modulation (IM) and direct detection (DD) and its implications for mobile communication are briefly reviewed. In order to support mobile communication with large coverage, the use of non-directed multiple-input multiple-output (MIMO) transmission is investigated.

The impact of low received signal powers on the signal-to-noise ratios (SNRs) due to non-directed transmission, is mitigated by using increased transmit signal powers. Since these can in turn result in nonlinear distortions at the transmitter (Tx) and receiver (Rx), a nonlinear equalization scheme is proposed and evaluated in laboratory experiments.

In order to understand the optical wireless channel seen in a production environment, first channel measurements were performed at BMW. Their analysis reveals a strong spatial selectivity of the optical wireless channels.

It is then suggested to use such MIMO channels with antenna diversity schemes, which improve overall reliability of the communication system. Adaptations of these schemes for OWC are discussed and verified in single- and multi-carrier transmission experiments.

Possible simplifications are derived and applied in order to allow for the first real-time implementation of an OWC system, which supports reliable mobile communication. The evaluation of such a communication system deployed at BMW is presented towards the end of this thesis.

## ZUSAMMENFASSUNG

---

Produktionsweisen haben sich in den letzten Jahrhunderten beeindruckend von Handarbeitsfertigungen mit geringer Stückzahl zu nahezu vollständig automatisierten Produktionen im großem Maße weiterentwickelt. Hierbei werden drei bedeutende Sprünge als *Industrielle Revolutionen* bezeichnet, welche erst die Mechanisierung, dann die Elektrifizierung und in diesem Jahrhundert die teilweise Automatisierung der Produktionsschritte mit sich gebracht haben. Der heutzutage stattfindende Schritt in Richtung flexibler, vollständig automatisierter und vernetzter Fabriken wird als vierte industrielle Revolution angesehen. In derartigen Fabriken ist zu erwarten, dass drahtlose Kommunikationssysteme, die die Anbindung autonomer und mobiler Einheiten innerhalb der Produktionsstätten unterstützen, eine bedeutende Rolle spielen werden.

Die vorliegende Arbeit beschäftigt sich daher mit der optischen drahtlosen Übertragung (OWC) als eine potenzielle drahtlose Technologie im Umfeld der industriellen Fertigung. Diese Anwendung bringt jedoch strenge Anforderungen bezüglich Zuverlässigkeit und Latenz mit sich, die bei dem Entwurf eines OWC Systems berücksichtigt werden müssen. Diese Arbeit beschäftigt sich daher mit Aspekten der physikalischen Schicht, die ausschlaggebend für eine zuverlässige Funktionsweise eines OWC System sind, das auf die Bedürfnisse der industriellen Kommunikation maßgeschneidert ist.

Es werden zu Beginn bekannte Konzepte von auf Intensitätsmodulation (IM) und Direktempfang (DD) basierender optischer Kommunikation und resultierende Folgen für mobile Kommunikation kurz wiederholt. Mit dem Ziel mobile Kommunikation mit hoher Abdeckung zu unterstützen, wird die Verwendung von ungerichteter multiple-input multiple-output (MIMO) Übertragung untersucht.

Der Einfluss geringer Empfangsleistungen auf die Signal-Rausch-Verhältnisse (SNR) durch die Verwendung ungerichteter Übertragung wird durch den Einsatz höherer Sendeleistungen gemäßigt. Da diese wiederum nichtlineare Verzerrungen der Sender (Tx) und Empfänger (Rx) hervorrufen, wird ein nichtlinearer Entzerrer vorgeschlagen und in Laborversuchen evaluiert.

Mit der Absicht den in Produktionsstätten vorgefundenen optischen drahtlosen Kanal besser zu verstehen, wurden erste Kanalmessungen bei BMW durchgeführt. Diese weisen auf eine starke räumliche Selektivität der optischen drahtlosen Kanäle hin.

Daher wird die Ausnutzung der MIMO Kanäle mit Antennendiversitätsansätzen vorgeschlagen, welche die Zuverlässigkeit des Kommunikationssystems verbessern. Anpassungen dieser Ansätze für OWC werden untersucht und mit Ein- und Mehrträgerübertragungen experimentell verifiziert.

Mögliche Vereinfachungen werden hergeleitet und angewandt, die eine erste Echtzeitimplementierung eines OWC Systems erlauben, welches eine zuverlässige mobile Kommunikation unterstützt. Die Evaluierung eines solchen, bei BMW eingesetzten, Kommunikationssystems wird gegen Ende der Arbeit vorgestellt.

## CONTENTS

---

1	INTRODUCTION	7
1.1	Optical Wireless Communication . . . . .	7
1.2	Industrial Wireless Communication . . . . .	9
1.3	Scope of the Thesis . . . . .	10
2	FUNDAMENTALS	13
2.1	Transmitters and Receivers . . . . .	13
2.2	Optical Wireless Channel . . . . .	15
2.3	Waveforms and Digital Signal Processing . . . . .	26
3	NONLINEAR COMPENSATION	33
3.1	Nonlinear System Description and Estimation . . . . .	33
3.2	Nonlinear Post-Equalizer . . . . .	37
3.3	Conclusion . . . . .	45
4	MEASUREMENT OF THE OPTICAL WIRELESS MIMO CHANNEL	47
4.1	Measurement Setup . . . . .	47
4.2	Measurement Results . . . . .	51
4.3	Conclusion . . . . .	54
5	RELIABLE DATA TRANSMISSION OVER THE OPTICAL WIRE- LESS MIMO CHANNEL	57
5.1	Antenna Diversity . . . . .	57
5.2	Broadband Transmission . . . . .	59
5.3	Narrowband Transmission . . . . .	66
5.4	Analog Combining and Real-Time Implementation . . . . .	70
5.5	Conclusion . . . . .	82
	Conclusions and Outlook	83
A	APPENDIX	85
A.1	Noise Floors . . . . .	85
A.2	Radio- and Photometric Quantities . . . . .	86
A.3	Phase Optimization for Equal Gain Transmission . . . . .	87
	List of Acronyms	93
	List of Symbols	97
	Bibliography	103
	Author's Bibliography	115



## INTRODUCTION

---

### 1.1 OPTICAL WIRELESS COMMUNICATION

In the past decades, the increasing interest in mobile communication was mostly covered by technologies from the field of radio frequency (RF)<sup>1</sup> communication. The benevolent attenuation conditions in air for radio frequencies below 6 GHz contributed significantly to this technological development. However, emerging bandwidth-hungry services such as virtual reality, mobile video streaming, online gaming, machine-type communications and Internet of Things (IoT) devices have lead to an increased interest in higher carrier frequencies in the mm-wave, THz and optical domain.

Communication systems based on technologies that rely on optical carriers, such as optical wireless communication (OWC), Li-Fi<sup>2</sup>, visible light communication (VLC), and infrared wireless communication (IWC), have by far the largest reservoir of unused bandwidth and thus the largest potential to become future-proof technologies. The availability of low-cost, small-size and energy efficient light-emitting diodes (LEDs), as used in modern illumination infrastructure, have lead to an increased interest in these technologies over the past decades. This increased interest is visualized in Fig. 1.1, which shows the number of scientific publications related to OWC, Li-Fi, VLC and IWC for each year over the past decades<sup>3</sup>. Throughout the thesis we will mostly refer to OWC as the most general term for communication with optical carriers. When adequate, we make a differentiation between the use of visible wavelengths as in Li-Fi/VLC and infrared wavelengths IWC. The following paragraphs are dedicated to the introduction of the field's evolution so far and the placement of this thesis within the field.

The first proposal of an optical wireless local area network (WLAN) was made by Gfeller and Bapst in 1979 [1]. The potential of diffuse light propagation for indoor IWC was further explored in [2]. A highly directed architecture with tracking was introduced in [3]. These early studies already considered a mobile unit (MU), but the coverage of high data rates was limited by insufficient power of the optical sources so that directed transmission based on manual, mechanical or electronic tracking were investigated. Spot diffusing as a semi-directive technique was introduced for high-speed non-line-of-sight (nLOS) communication in [4] and extended to multiple spots in [5], [6]. A combined diffuse and directed link was proposed in [7], enabling

<sup>1</sup> A list of all acronyms can be found on page 93. A list of all symbols can be found on page 97.

<sup>2</sup> The term *Li-Fi* is a creation that reminds of the trademark *Wi-Fi*<sup>TM</sup>. Both terms are often interpreted as abbreviations of *light fidelity* and *wireless fidelity*, respectively, which in turn are references to the established terms *low fidelity* and *high fidelity* in audio technologies.

<sup>3</sup> The data was obtained from a search query on *web of science*<sup>TM</sup>. The query matched publications related to the topics of OWC, Li-Fi, VLC and IWC:

"TS=((optical AND wireless AND communication) OR (optical AND wireless AND communications) OR (OWC) OR (light AND fidelity) OR (lifi) OR (visible AND light AND communication) OR (visible AND light AND communications) OR (VLC) OR (infrared AND wireless AND communication) OR (infrared AND wireless AND communications))"

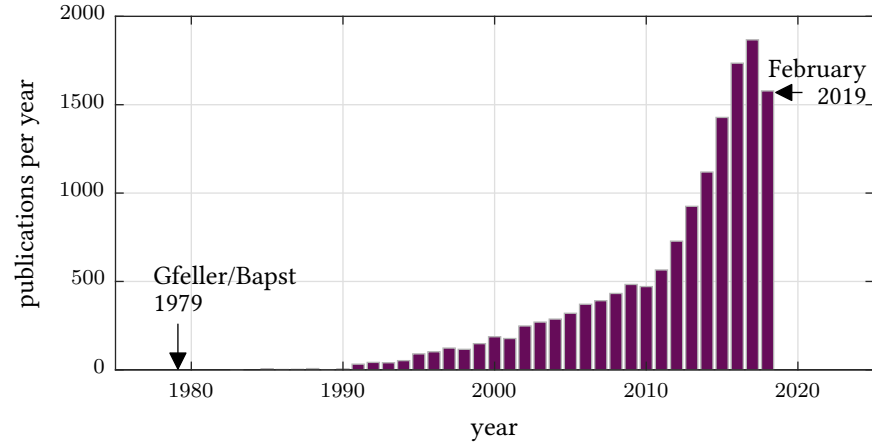


Figure 1.1: Popularity of field by number of publications per year. Since the underlying data was queried in February 2019, not all works published in 2018 were yet indexed and an additional increase may be expected.

indoor coverage at high data rates, however, with increased costs. All works stated thus far belong to the subfield of IWC. A few disruptive inventions stimulated research dominantly at the visible wavelengths:

An important technological advance was the availability of new types of light sources. The introduction of GaN LEDs [8] coated with white-light emitting phosphors [9] made powerful visible light sources available at a low cost due to their popular use for illumination. Such LEDs can be modulated at reasonably high speed and can be used for VLC. Early on, powerline communication (PLC) was proposed as a natural backbone for VLC [10]. Using the existing illumination infrastructure, in which incandescent light is increasingly replaced by LED luminaries, illumination and communication purposes could be fulfilled simultaneously. Another change was brought by the use of red-green-blue (RGB)-LEDs and red-green-blue-yellow (RGBY)-LEDs. The availability of three (RGB) or four (RGBY) colors, allowed for the parallel use of multiple optical carriers with independent signalling, also known as wavelength-division multiplexing (WDM) [11]–[14]. Due to their intrinsically higher modulation bandwidths, laser diodes (LDs) [15]–[17] and micro light-emitting diodes ( $\mu$ LEDs) [18]–[21] are attractive light sources for high-speed communication in the multiple gigabit per second regime.

The consideration of advanced waveforms such as orthogonal frequency-division multiplexing (OFDM), beneficial in the presence of limited bandwidth electronics and multipath optical channels, was part of the aforementioned record-breaking papers. Combined with an offset in amplitude to fulfill the non-negativity constraint of the intensity modulation (IM)/direct detection (DD) channel, the concept of direct-current biased optical (DCO)-OFDM was first proposed in [22]. An adaptation to multipath distortions with an OFDM based closed-loop adaptation was suggested independently by two groups in [23]–[26]. The feasibility of modulating a white LED’s intensity with DCO-OFDM was first validated experimentally for a limited bandwidth of 4 kHz in [27]. Since then, there has been a focus on waveforms designed to fulfill the IM/DD non-negativity constraint, both for single-carrier (SC) [14], [28]–[33]

and multi-carrier waveforms, such as asymmetrically clipped optical (ACO)-, Flip-, unipolar (U)- and enhanced unipolar (eU)-OFDM [34]–[37].

Further advances regarding OWC have been made in the field of communication theory that have led to tighter bounds on the capacity of the point-to-point (P2P) IM/DD Poisson [38] and Gaussian [39], [40] channels with non-negativity, peak and average power constraints. In VLC, where optical carriers serve mostly for illumination purposes and thus exhibit high optical powers, the latter are particularly interesting.

Albeit its various advances, OWC has continued to struggle finding its break-through into applications with large markets as a standalone technology. In case of WLANs, e.g., RF solutions such as *Wi-Fi*<sup>TM</sup> dominate this market segment. Thus, OWC is nowadays often considered an enhancing or supporting technology, to offload traffic from the crowded RF spectrum [41]–[43] and hybrid solutions have started to be investigated [44], [45]. The works in this thesis, however, are focused on a standalone OWC system with an optical wireless uplink (UL) and downlink (DL). The divergence from the just stated trend results from the industrial production environment, which this thesis focuses on. Before stating the goals of this thesis in detail, however, we briefly introduce the field of industrial (wireless) communication.

## 1.2 INDUSTRIAL WIRELESS COMMUNICATION

Nowadays, industrial facilities rely on digital communication for control and automation of its production processes. The programmable logic controllers are usually connected to the factories' machines (i.e., sensors, actuators, motors, switches, etc.) via so called fieldbuses. Fieldbuses may be seen as networks wired in a bus topology, whose protocols are standardized by the International Electrotechnical Commission (IEC) with a focus on the needs of industrial communication networks [46]. A classification of use cases for industrial communication is provided in [47]. Traditionally, distributed control systems constitute a large fraction of the applications. In those, data from distributed sensors is fed to a centralized control logic, which in turn steers distributed actuators. For control loops, low end-to-end delays, a low packet delay variation (PDV) and short cycle times are important. Data rates, on the contrary, are often low and only small packets, with a size of few byte (B), have to be transmitted [48]. Moreover, integrity must be guaranteed for virtually all packets as the control logic works only with continuous connection to sensors and actuators. Therefore, it is appropriate to optimize for high reliability, low cycle times and low latencies when designing industrial communication protocols [49].

It is important to note that the different applications within industrial communication networks do not all have the same requirements. While cycle times are not important for alarms, reliable transmission and low latency are crucial. Configuration and management traffic typically has more relaxed requirements, albeit an occasional need for higher throughputs, for example in case of file transmission. Further, novel and future applications such as industrial augmented reality [50] may simultaneously require high throughput and low latencies when offloading image processing to a pow-

erful server [51]. Machines functioning in an autonomous manner, which require a network connection only for configuration and management, have very low requirements for network performance and the focus lies on easy configuration of the network connection. This is expected to become more common through the paradigm of software-defined manufacturing in future flexible factories [52], [53].

Key innovations of the industrial revolutions:

1st (around 1800)  
steam engines and  
mechanization of  
production processes

2nd (around 1900)  
electrification and  
mass production

3rd (80's - ongoing)  
automation based on  
robots, electronics and  
information  
technology

4th (starting)  
Yet to be determined.  
Common descriptive  
terms include *IoT*,  
*artificial intelligence*,  
*quantum computing*,  
*augmented reality*,  
*autonomous vehicles*,  
*smart factories*

The latter examples are use cases envisioned to play an important role in the so-called *Industry 4.0* - the fourth industrial revolution<sup>4</sup>. One of its additional innovations is the disruptive change from static, mostly single-good producing factories towards flexible, highly automated ones. A fundamental requirement for such a factory of the future [47] is moving from wired field-buses to a reliable wireless communication system to interconnect MUs to the factory's network. In RF communication, steps in this direction have been taken, e.g., by adapting the Institute of Electrical and Electronics Engineers (IEEE) 802.15.4 standard into standards to be used for industrial wireless communication such as WirelessHART [56] and ISA100 [57]. Research and development activities have focused on potential future industrial radio technologies that fulfill more stringent performance requirements. Most approaches exploit diversity in one way or another. For temporary deep fades, automatic repeat request (ARQ) may be used to make use of temporal diversity. However, when required cycle times are shorter than the coherence time of a channel, ARQ schemes have proven ineffective [49], [58]–[60]. Cooperative relaying implemented on the medium access control (MAC) layer, such as e.g. *EchoRing*<sup>TM</sup>, additionally takes advantage of the spatial diversity of the wireless channel [60], [61]. On the physical layer, spatial diversity may also be used by means of multiple-input multiple-output (MIMO) processing [62]. Here, antennas are distributed in space, thus spanning multiple spatial channels simultaneously with higher probability of yielding a sufficiently good one. Most of these RF technologies rely on transmission in the license-free industrial, scientific and medical (ISM) bands, which due to likely interference impedes their ability to guarantee in-time packet delivery [53]. Therefore, the approach to use long term evolution (LTE) or subsequent technologies with dedicated and licensed frequencies recently gained interest [47], [63].

While RF communication in the sub 6 GHz bands continues to be an excellent medium for multiple applications, its crowded spectrum cannot guarantee transmission free of interference in the unlicensed bands or requires the application for and payment of expensive licenses. Thus, alternative frequency ranges are currently being investigated with the use of optical carriers being a potential candidate.

### 1.3 SCOPE OF THE THESIS

In this thesis the two previously introduced fields are merged and the application of OWC in an industrial production environment is studied. Interestingly,

<sup>4</sup> The term *Industry 4.0* originates from the strategy of the German government to modernize industrial production by means of digital innovations [54] and covers parts of the vision known as *Industrial Internet* in the United States of America [55].

the general idea was already born in 1988 [64]<sup>5</sup>. While we do not know exactly why it was never adopted in the factories of the past, we know that for the envisioned factories of the future, requiring reliable wireless communication at moderate data rates in the order of tens of Mb/s and reasonably low latencies in the order of a few milliseconds<sup>6</sup>, the properties of optical carriers continue to be of interest. Two important aspects are the spatial confinement of optical carriers and the license-free spectrum. While the first makes OWC robust against potentially malicious interference (e.g., jamming) or eavesdropping and hereby improves the networks security, the second allows for quick and independent deployment.

Starting at the bottom of every communication system, we focus on reliability aspects of the optical wireless *physical* layer. After this introductory chapter, we review basic concepts of IM/DD communication and its implications for mobile communication in Chapter 2. The objective is to provide a condensed source of prior existing knowledge, required to understand the content and interpretations in the following chapters. Chapter 3 discusses a first approach to improve reliability by compensation of nonlinear impairments of the OWC channel, which allows the use of increased signal powers. Chapter 4 focuses on the exploration of the optical wireless MIMO channel and presents channel measurements obtained in an industrial production environment. It lays the foundation for the subsequent Chapter 5, in which data transmission exploiting spatial diversity of such MIMO channels is studied experimentally. After the feasibility of the individual components and diversity concepts is tested in a laboratory setup, a real-time implementation is presented and ultimately put under test in a real production environment.

---

5 According to [65], the IWC concept presented in [64] coincidentally was also the first wireless fieldbus at all.

6 The exact required latencies vary with the application of the communication system and are therefore difficult to determine a priori. However, the order of a few milliseconds is a reasonable target unlocking multiple applications in industrial wireless communication.



This chapter serves as an introduction to known results and concepts regarding optical wireless communication (OWC) and presents the simulation and digital signal processing (DSP) toolchain used throughout the thesis.

## 2.1 TRANSMITTERS AND RECEIVERS

Unfortunately, there appears to be no *standard* transmitter (Tx) or receiver (Rx) in OWC, making it difficult to discuss them without imposing too many assumptions. We therefore introduce the basic building blocks most transceivers (TRxs) have in common, before explaining the particularities of the TRxs used for the experimental works presented in this thesis. For brevity, we will be referring to the latter as *our* TRxs. Figure 2.1 shows such basic building blocks for a point-to-point (P2P) system with a single Tx and a single Rx. Commonly,

1. a source generates information in the form of bits. From a physical layer point of view, these are likely to come from the data link layer and may represent any type of generic information. These bits are fed to a DSP unit of the Tx, which may, e.g., include the protection of bits via a forward error correction (FEC) scheme, an addition of known training sequences for channel estimation and the mapping into samples of a waveform suitable for transmission over an OWC channel. ↓ transmitter
2. A digital-to-analog converter (DAC) converts the resulting digital samples to the analog electrical domain, where
3. an analog pre-equalization circuit may compensate for the strong low-pass behavior of the following components. A broadband amplifier creates a current, approximately proportional to the desired signal waveform and drives an
4. electro-optical (E/O) conversion element, such as a light-emitting diode (LED) or laser diode (LD). The resulting optical beam can be shaped by optical elements such as lenses or spatial light modulators (SLMs). ↑ transmitter
5. At the Rx, the incident optical signal may be collected by an optical concentrator and converted back into the analog electrical domain with an opto-electrical (O/E) element, such as a positive intrinsic negative (PIN) photodiode (PD) or avalanche photodiode (APD). ↓ receiver
6. Subsequently, an analog post-equalization may be used to flatten the overall frequency-response. The following amplification stage is particularly important in a system with centralized processing, where the received signal must travel through long cables prior to
7. digitization with an analog-to-digital converter (ADC). ↑ receiver
8. The DSP at the Rx performs channel estimation and equalization and recovery of the originally transmitted bits, which are passed to the sink of the physical layer, likely the data link layer.

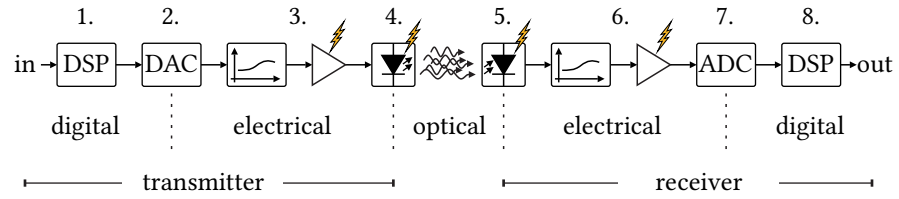


Figure 2.1: Generic block diagram of a P2P OWC system. Yellow flashes indicate components with potentially nonlinear behavior.

The optical front ends used in our TRxs, however, were built with low-cost, off-the-shelf electronics components and therefore use non-coherent light sources such as LEDs with intensity modulation (IM) for E/O conversion and silicon (Si) PIN PDs with direct detection (DD) for O/E conversion. The size of the PD lies in the order of multiple square millimeters and is thus multiple orders of magnitude larger than the wavelengths contained in the incident optical signal. Generally, the phase and magnitude of the optical field vary strongly along the spatial dimensions and deep fades occur at displacements with a magnitude in the order of wavelength of optical carriers. If detectors in that order of magnitude or smaller were used, these fades would be visible or behave similarly to multipath fading in radio frequency (RF) communication. However, the comparatively large detectors in use average out this effect and as a result, the current flowing through the PD in a first order approximation may be assumed proportional to the instant optical power [2].

Figure 2.2 shows the emission spectra of the LEDs [66], [67] built into our TxS in comparison to other light sources commonly found in indoor environments [1], [2] normalized to their respective peak values. By additionally displaying the responsivity of the PD used in our RxS as a dashed line [68], it becomes clear that the RxS in use capture light from most common light sources, with best O/E conversion efficiencies around the infrared (IR) range. While natural light sources emit with a mostly constant optical power, artificial light sources may exhibit fluctuations over time of up to a few hundred kHz [69], causing interference at these low frequencies. Both types of light sources, however, are potential sources of shot noise. When light is

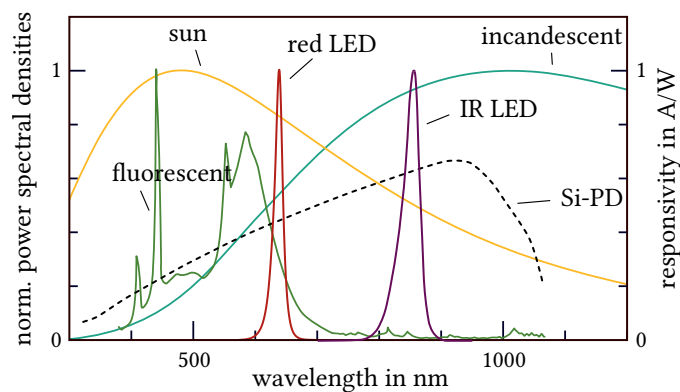


Figure 2.2: Power spectral densities of different light sources and the responsivity of a common Si-PD. Visible light ranges from approximately 390 to 700 nm.

interpreted as the sum of quantized units of optical energy, i.e. photons, shot noise describes the fluctuation of detected photons within a short time frame. In bright ambient light, shot noise is often considered to be the limiting noise in an OWC system [2], [70]. In order to determine which fundamental limitations are faced within the studied environments and with our TRxs, a small series of measurements was conducted. These are presented in Appendix A.1, where it is observed that the limiting noise is independent of the received signal and ambient light and in this respect behaves like thermal noise.

## 2.2 OPTICAL WIRELESS CHANNEL

This section is dedicated to effects occurring between one or more Tx and one or more Rx, i.e., the optical wireless channel. After an introduction to the concepts explaining the dominant geometrical losses, we continue with reflective multipath and multiple-input multiple-output (MIMO) channels.

### 2.2.1 Power Dispersion and Reception

The dominating losses in indoor OWC are geometrical losses arising from the fact that only a small fraction of the transmitted power dispersed into space is captured by the Rx. In order to understand the implications for building a reliable communication system, this section attempts to formalize the free-space propagation of an optical signal. An optical signal may be interpreted as the conglomerate of multiple photons, each with an energy proportional to its optical frequency  $\nu_{\text{ph}}$  or inversely proportional to its wavelength  $\lambda_{\text{ph}}$ :

$$E_{\text{ph}} = h \cdot \nu_{\text{ph}} = \frac{h \cdot c}{\lambda_{\text{ph}}} \quad (2.1)$$

Here,  $h$  is the Planck constant and  $c$  the speed of light in vacuum. Based on the energy of single photons, we may construct a time-dependent energy signal  $E(t)$  at time  $t$  as

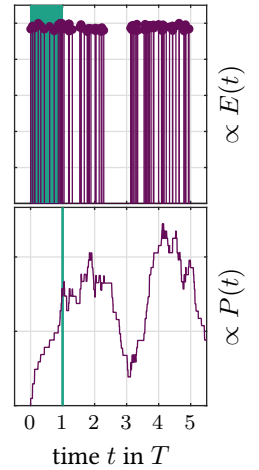
$$E(t) = \sum_{k=1}^{\infty} \delta(t - t_k) E_{\text{ph},k}, \quad (2.2)$$

where  $E_{\text{ph},k}$  is the energy of the  $k$ -th photon detected at the time instant  $t_k$ . This mathematical construct based on the Dirac delta function  $\delta(t)$  allows us to define the optical power  $P(t)$  observed up to a time instant  $t$  and within a preceding observation window  $T$  as:

$$P(t) = \frac{1}{T^2} \int_0^T E(t - \tau) d\tau \quad (2.3)$$

Note that Eq. (2.3) can be interpreted as the convolution of the energy signal with a rectangular function, hereby resulting in a low-pass behavior. For a communication system, it is thus of interest that the observation time is sufficiently small compared to the signal's bandwidth.

To describe the spatial dependence of the optical power defined in Eq. (2.3), we borrow a few useful terms from the field of radiometry<sup>1</sup> [71]. Since it is the



Purple lines show an exemplary energy and power signal. A green rectangle indicates the observation window corresponding to a time instant indicated by a green line.

<sup>1</sup> Since OWC also covers IR communication, we focus on *radiometry*, not *photometry*. For a brief differentiation between the two fields see Appendix A.2

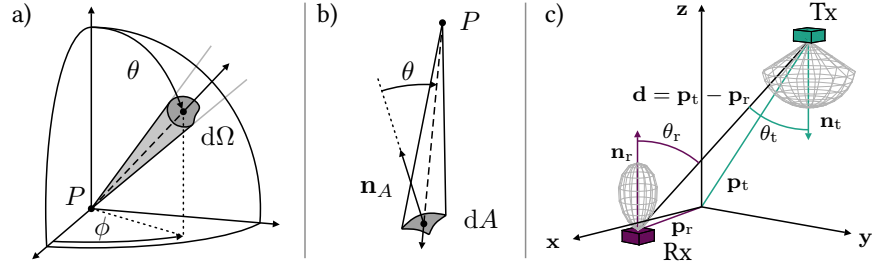


Figure 2.3: a) The fraction of optical power passing through a solid angle element  $d\Omega$  defines the *radiant intensity*. b) The fraction of optical power incident on a surface element  $dA$  defines the *irradiance*. c) Spatial relationship between a Tx/Rx pair.

field concerned with the measurement of power of electromagnetic radiation and the transfer thereof, the quantities are also useful to mathematically describe the signal power flows in wireless IM/DD systems.

The first useful quantity is the *radiant intensity*  $R$ , which is the fraction of *radiant power*<sup>2</sup> emitted, transmitted, received or reflected through an infinitesimally small element of solid angle  $d\Omega$  (see Fig. 2.3a):

$$R = \frac{dP}{d\Omega} \quad (2.4)$$

It is given in Watt per steradian, i.e., per square radian (W/sr). Throughout the thesis,  $\Omega$  is the solid angle and  $d\Omega = \sin(\theta) d\phi d\theta$  its differential. All angles, including the azimuthal and polar angles  $\phi$  and  $\theta$ , will be given in radian, unless denoted by the degree symbol  $^\circ$ . We will use the radiant intensity to describe the angular dependence with which the light source of a Tx radiates its total optical power  $P_t$  into space:

$$R(\phi_t, \theta_t) = P_t \cdot R_0(\phi_t, \theta_t) \quad (2.5)$$

The subscript t denotes the correspondence to a Tx throughout the thesis. The second useful quantity is the *irradiance*  $I$ , which is the fraction of optical power incident upon a surface element  $dA$  at an angle  $\theta$  with respect to the surface normal  $\mathbf{n}_A$  (see Fig. 2.3b):

$$I = \frac{dP}{\cos(\theta)dA} \quad (2.6)$$

We are interested in the irradiance resulting from the light emitted by a source located at point  $\mathbf{p}_t$  incident on a detector with area  $A$  positioned at point  $\mathbf{p}_r$ . The distance between this Tx/Rx pair is  $d = \|\mathbf{d}\|_2 = \|\mathbf{p}_t - \mathbf{p}_r\|_2$ , where  $\|\cdot\|_2$  denotes the Euclidean norm and the subscript r indicates the correspondence to a Rx. Figure 2.3c shows a sketch of the spatial relationship between this pair. For the indoor industrial environments investigated in this thesis, distances of interest are in the range of a few meters, while the detector areas lie in the range of one  $\text{cm}^2$ . For such  $A \ll d^2$ , the irradiance may be assumed constant with  $I = R(\phi_t, \theta_t)/d^2$  [1], [2]. Without a lens, the

<sup>2</sup> *Radiant power* or *radiant flux* are two commonly used term in radiometry. However, we will continue using the equivalent term *optical power*.

power received by a detector with physical area  $A$  depends on the irradiance  $I$  and the angle  $\theta_r$  with which a ray is incident in the following way:

$$\begin{aligned} P_r &= \int_A I \cdot \cos(\theta_r) dA \\ &= I \cdot A \cdot \cos(\theta_r) \\ &= \frac{1}{d^2} \cdot R(\phi_t, \theta_t) \cdot A \cdot \cos(\theta_r) \end{aligned} \quad (2.7)$$

When a Rx is used with a concentrator lens, its angular dependence is influenced by many factors such as a possible anti-reflective coating, the lens' and its surrounding material's refractive indices  $n_l$  and  $n_a$ , the geometry of the lens. For our purposes, it suffices to summarize these angular dependent terms into a resulting effective area  $A_{\text{eff}}$ :

$$P_r = I_r \cdot A_{\text{eff}}(\theta_r) \quad (2.8)$$

$$= \frac{1}{d^2} \cdot R(\phi_t, \theta_t) \cdot A_{\text{eff}}(\theta_r) \quad (2.9)$$

The optical gain of a lens  $G(\theta)$  is the ratio between the detected power  $P_r$  without and with lens [72]. The resulting optical gain is then simply given by

$$G(\theta) = \frac{A_{\text{eff}}(\theta)}{A \cdot \cos(\theta)}. \quad (2.10)$$

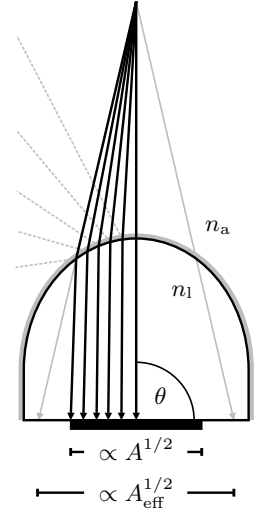
While it is possible to describe the effective areas for multiple types of concentrators such as ideal concentrators [1], truncated hemispherical lenses [72] or compound parabolic concentrators [73], we are mostly interested in a mathematical expression that describes the angular dependencies of our devices sufficiently well, such that the resulting models can be used in simulations. For such models, we will be assuming rotational symmetry of  $R$  and  $A_{\text{eff}}$  around their surface normals and thus drop dependencies on the azimuth angles  $\phi$ . Generalized Lambertian functions of order  $K$  were used in [1], [74] to describe  $R_0(\theta_t)$  with different focusing gains. Similarly, we may define them as follows:

$$L^{(K)}(\theta) \stackrel{\text{def}}{=} \begin{cases} \frac{K+1}{2\pi} \cos^K(\theta) & \text{for } 0 \leq \theta \leq \frac{\pi}{2}, \\ 0, & \text{otherwise.} \end{cases} \quad (2.11)$$

Note that  $\int L^{(K)} d\Omega = 1 \forall K$ . Reformulating Eq. (2.11), the half-power semi-angle (HPSA) is consequently given as  $\theta_{1/2} = \cos^{-1}(0.5)^{1/K}$ . In order to model a limitation to a maximum transmit/receive angle  $\theta'$ , e.g., due to packaging or other imperfections, a multiplication of the Lambertian functions with the rectangular function  $\square_{\theta'}(\theta)$  is possible. It is defined as

$$\square_{\theta'}(\theta) \stackrel{\text{def}}{=} \begin{cases} 1 & \text{for } \theta \leq \theta', \\ 0 & \text{otherwise.} \end{cases} \quad (2.12)$$

Measured angular dependencies for a pair of commonly used LEDs [66] and PDs [68] are shown as dashed lines in Fig. 2.4a. The solid lines represent



Shape, material and coating of a lens change a receiver's effective area  $A_{\text{eff}}(\theta)$  and thus optical gain.

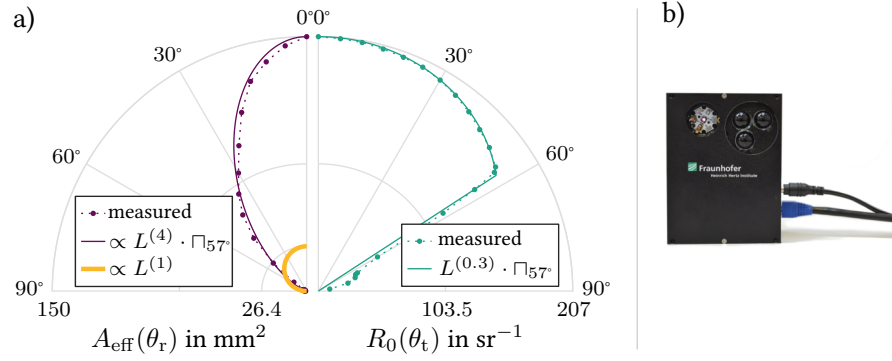


Figure 2.4: a) Measured angular dependencies of the Tx and the Rx used in the experiments and their approximations with Lambertian functions. The restriction to an approximate maximum angle of  $\theta' = 57^\circ$  results from the casing of the front ends, shown in b).

fitted directivities based on combinations of a Lambertian and a rectangular function. We may observe that  $R_0(\theta_t)$  is rather well approximated by

$$R_0(\theta_t) \approx L^{(0.3)}(\theta_t) \cdot \Gamma_{57^\circ}(\theta_t) \quad (2.13)$$

and the effective area with  $A_{\text{eff}}(0) = 150 \text{mm}^2$  [68] by

$$A_{\text{eff}}(\theta_r) \approx \frac{2\pi}{4+1} L^{(4)}(\theta_r) \cdot \Gamma_{57^\circ}(\theta_r) \cdot 150 \text{mm}^2. \quad (2.14)$$

The limitation to  $\theta' = 57^\circ$  results from the use of a casing similar to that shown in Fig. 2.4b, which could be improved if the LED and PD were not recessed in the casing. As a reference, the effective area of the same PD without an optical concentrator [75] is added to Fig. 2.4a as a yellow solid line, which reveals the known benefits of concentrators. While the Rx's HPSA is reduced when using a concentrator, the resulting  $A_{\text{eff}}$  is enlarged (purple lines) and thus the received optical power is boosted within the maximum receive angle  $\theta'$ . Along the surface normal of the detector, the increased effective area results in an optical power gain of 7.5 decibel (dB).

With the angular dependencies of our Tx/Rxs established, the line-of-sight (LOS) optical gain coefficient may be computed as

$$h_{r,t} = \frac{P_r}{P_t} = \frac{1}{d^2} \cdot R_0(\theta_t) \cdot A_{\text{eff}}(\theta_r). \quad (2.15)$$

This quantity describes the average channel gain between a Tx and Rx pair. Including the delay  $\tau = d/c$  due to free-space propagation over a distance  $d$  at the speed of light in vacuum<sup>3</sup>  $c$ , yields the LOS channel impulse response (CIR) between a single Tx and a single Rx:

$$h_{\text{LOS}}(t) = \delta(t - \tau) \cdot \frac{1}{d^2} \cdot R_0(\theta_t) \cdot A_{\text{eff}}(\theta_r) \quad (2.16)$$

For sufficiently slow changes in the order of multiple  $\mu\text{s}$ , which might result, e.g., from a spatial displacement of either Tx or Rx, the overall channel can

<sup>3</sup> In most cases the surrounding medium may not be vacuum and can be expected to be air with a refractive index of  $n_a \approx 1.0003$  and the speed of light is slightly reduced to  $c/n_a$ .

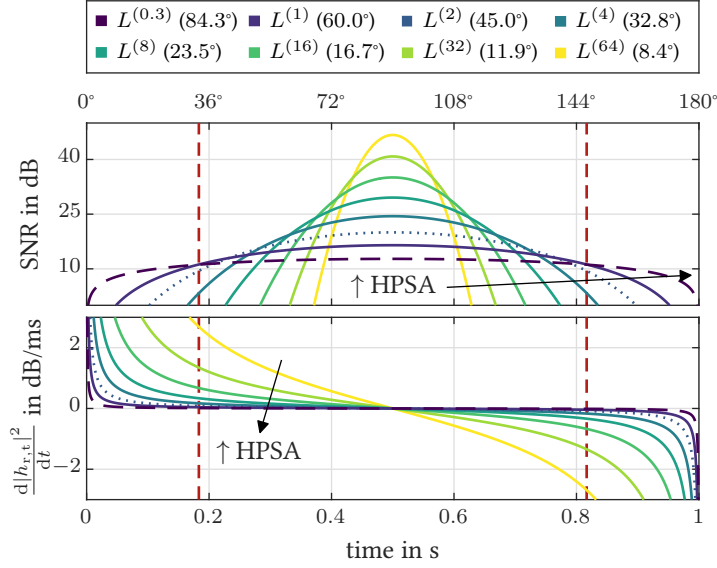


Figure 2.5: Changes in SNR (top) and the channel coefficients (bottom) due to a rotation of  $180^\circ/\text{s}$  for different Lambert orders and resulting HPSA (in parenthesis). The purple dashed lines correspond to  $L^{(0.3)}$ , which applies to the Tx used for simulations/experiments in Chapter 4 and Sections 5.1 to 5.3. The blue dotted lines correspond to  $L^{(2)}$ , which applies to the Tx used in the experiments of Chapter 3 and Section 5.4. The red dashed lines indicate the maximum transmit angle  $\theta' = 57^\circ$

be assumed to be time-invariant over the length of the CIR. In such cases, the transmission of a signal  $x(t)$  over the channel  $h_{\text{LOS}}(t)$  can be written as a linear convolution [76], in the following denoted by  $*$ :

$$y(t) = h_{\text{LOS}}(t) * x(t) + n(t) \quad (2.17)$$

At the Rx, the received signal  $y(t)$  is then composed of the distorted transmit signal and additive noise  $n(t)$ . As Eq. (2.5) indicates, a light source with a larger HPSA, yet fixed  $P_t$ , will disperse power more broadly into space, resulting in a smaller maximally achievable  $P_r$  for a given effective area of the Rx. For noise sources independent of the Tx-side radiant intensity, such as shot-noise from ambient light or thermal noise from the Rx circuitry, the use of Tx with larger HPSA results in a lower, maximally measurable signal-to-noise ratio (SNR).

This is illustrated by simulation results<sup>4</sup> in the upper graph of Fig. 2.5. Here, Tx with varying HPSAs undergo a rotation of  $180^\circ$ . At  $0^\circ$  and  $180^\circ$ , the Tx's surface normals  $\mathbf{n}_t$  are perpendicular to the surface normal  $\mathbf{n}_r$  of the Rx. After a rotation of  $90^\circ$ , the Tx/Rx pairs are perfectly aligned, which results in the largest channel coefficients and thus largest SNRs for all HPSAs. Peak values are obtained for Tx with high directivity, i.e., small HPSA. However, for reliable mobile communication, the availability of a sufficiently good SNR over a broad range of angles is particularly important.

<sup>4</sup> As a calibration step, an SNR of 20 dB was set to match the experimental results in Section 3.2.1, for an aligned Tx with  $R \propto L^{(2)}$  and a Rx with  $A_{\text{eff}} \propto L^{(4)}$  at  $d = 3$  m.

Furthermore, if we do not only consider a static case, but ascribe a constant speed of  $180^\circ/s$  to the rotation, the rotational displacement may be translated to a time variation of the channel coefficient in Eq. (2.15). The bottom graph in Fig. 2.5 shows the coefficient change in dB/ms when using TxS with varying HPSAs. It is noteworthy that TxS with high directivity, i.e. small HPSAs, show significant variations of the channel over time ( $>1$  dB/ms) for a large portion of the rotation. This becomes important when we consider that typical packet-based link rate adaptations take tens of ms between updates [77]–[79]. Thus, the channel coefficients may change between two updates by multiple tens of dB, making a mobile and reliable transmission impossible unless very large SNR margins are used. This effect peculiar to OWC has also been observed in [80], where it was combated by predictive estimation of the SNR evolution, thus allowing for faster rate adaptation. However, with the objective of an inherently more reliable physical layer design, this thesis focuses on the use of Tx and Rx with large HPSAs, resulting in larger coverage and slower channel changes. This comes at the cost of higher dissipation of optical power into space and consequently smaller received powers. The main body of this thesis thus discusses two approaches to deal with this effect in order to improve physical layer reliability for mobile OWC.

Since in OWC the term *power* may be used in different contexts, we now take a moment to differentiate between its uses. This hopefully avoids confusion in the later chapters of the thesis. So far, we have only considered *optical* powers  $P$  to explicitly refer to the power conveyed by an optical signal. In the previous paragraphs, the transmitted optical power  $P_t$  is assumed to be independent of time, while the received power  $P_r$  may vary over time due to spatial displacement. When modulated with an information-carrying signal,  $P_t$  also becomes a (quickly) time-varying quantity  $P_t(t)$ . It is then useful, both at the Tx and Rx, to explicitly differentiate between an average power  $\bar{P}$  and a quickly time-varying power  $\tilde{P}(t)$ . While  $\bar{P} = \frac{1}{T} \int_0^T P(t - \tau) d\tau$  may be assumed to be constant within a time window  $T$  of multiple  $\mu s$  around the time instant  $t$ ,  $\tilde{P}(t) = P(t) - \bar{P}$  is a quickly varying, time-dependent quantity. Both optical powers  $\tilde{P}(t)$  and  $\bar{P}$  face the same channel loss as given, e.g., by Eq. (2.15). While the average optical power  $\bar{P}$  is important, e.g., for illumination purposes when using visible light,  $\tilde{P}(t)$  is the information-carrying signal and will henceforth be referred to as *optical signal power*. We define the ratio of the Tx average optical power  $\bar{P}_t$  and the root-mean-square of the optical signal power  $\tilde{P}_t$  as the modulation index  $\mu = \sqrt{\frac{1}{T} \int_0^T \tilde{P}_t^2(t - \tau) d\tau} / \bar{P}_t$ . In a linear regime,  $\tilde{P}(t)$  is proportional to the quickly varying LED drive current. Hence, the Tx-side *electrical signal power*  $\tilde{P}_{e,t}$ , i.e., the power of the time-depending signal components only, defines the strength of the resulting optical signal power  $\tilde{P}(t)$ . At the Rx,  $\tilde{P}_{e,r}$  is the quantity defining the receive-side SNR.

### 2.2.2 Reflective Multipath Channel

In the previous section we have explained that for a reliable OWC system the use of non-directed transmission with large HPSA of Tx and Rx results in smaller channel variations and increased coverage. This was exemplarily

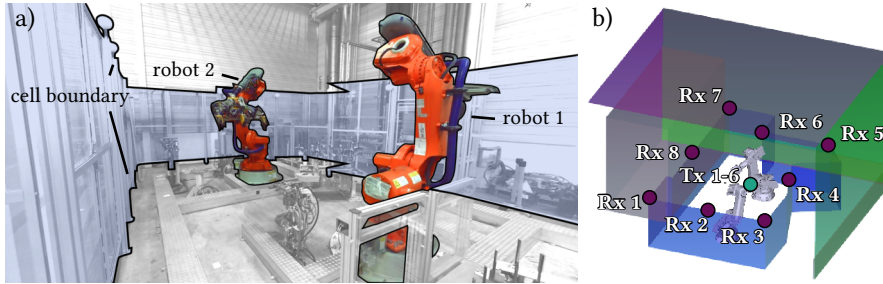


Figure 2.6: a) Photograph of the manufacturing cell that was scanned and used to provide a realistic simulations environment. b) Visualization of the simulated geometry in [95].

illustrated for a LOS channel. However, Rxs with large HPSAs also capture reflections of surrounding objects and walls, particularly when Txs with similarly large HPSAs are employed. We therefore consider the existence of reflective channels and discuss their impact on the design of an OWC system for industrial environments.

The multiple spatial paths resulting from reflective channels and the implicit multipath distortions due to inter-symbol interference (ISI) have long been studied in the OWC community [70], [81]–[85]. Mathematically, the overall CIR  $h(t)$  can be split into a LOS component and one resulting from the reflected, i.e. non-line-of-sight (nLOS), components:

$$h(t) = h_{\text{LOS}}(t) + h_{\text{nLOS}}(t) \quad (2.18)$$

While the LOS component given in Eq. (2.16) depends only on the spatial relationship between the Tx and Rx in terms of distance  $d$  and orientation, the nLOS component  $h_{\text{nLOS}}(t)$  additionally depends on the surroundings, i.e., the geometry of the room and the reflectivity of its walls or objects within the room. The variety of channel realizations is thus manifold and difficult to condense into a single channel model with only a few parameters.

Most attempts of modeling both components in Eq. (2.18) therefore assume at least a room geometry and reflectivity of its walls such as in [86], which presents a simulation framework that has since been refined continuously [85], [87]–[90]. A macroscopic abstraction of the indoor optical channel model to fewer parameter models was suggested in [83], [91] and allows for the simple calculation of an approximate channel response. The most detailed and site-specific approach for modelling Eq. (2.18) is that of raytracing based on Monte-Carlo simulations, which has been extensively studied in the field of computer graphics. However, for the computation of a CIR such as  $h(t)$ , rays must additionally be traced over time [92], [93]. When incorporated with wavelength-dependent reflectivities, it can recreate realistic CIRs with high accuracy also for visible light communication (VLC) [94].

In order to obtain realistic and standardized CIRs, a series of raytracing based channels have been proposed in the Institute of Electrical and Electronics Engineers (IEEE) P802.15 working group [95] and are available in [96]. One set of its CIRs is the result of extensive raytracing simulations, whose geometry was obtained from a laser scan of a real manufacturing cell. A photograph and the resulting geometrical model of this cell are shown

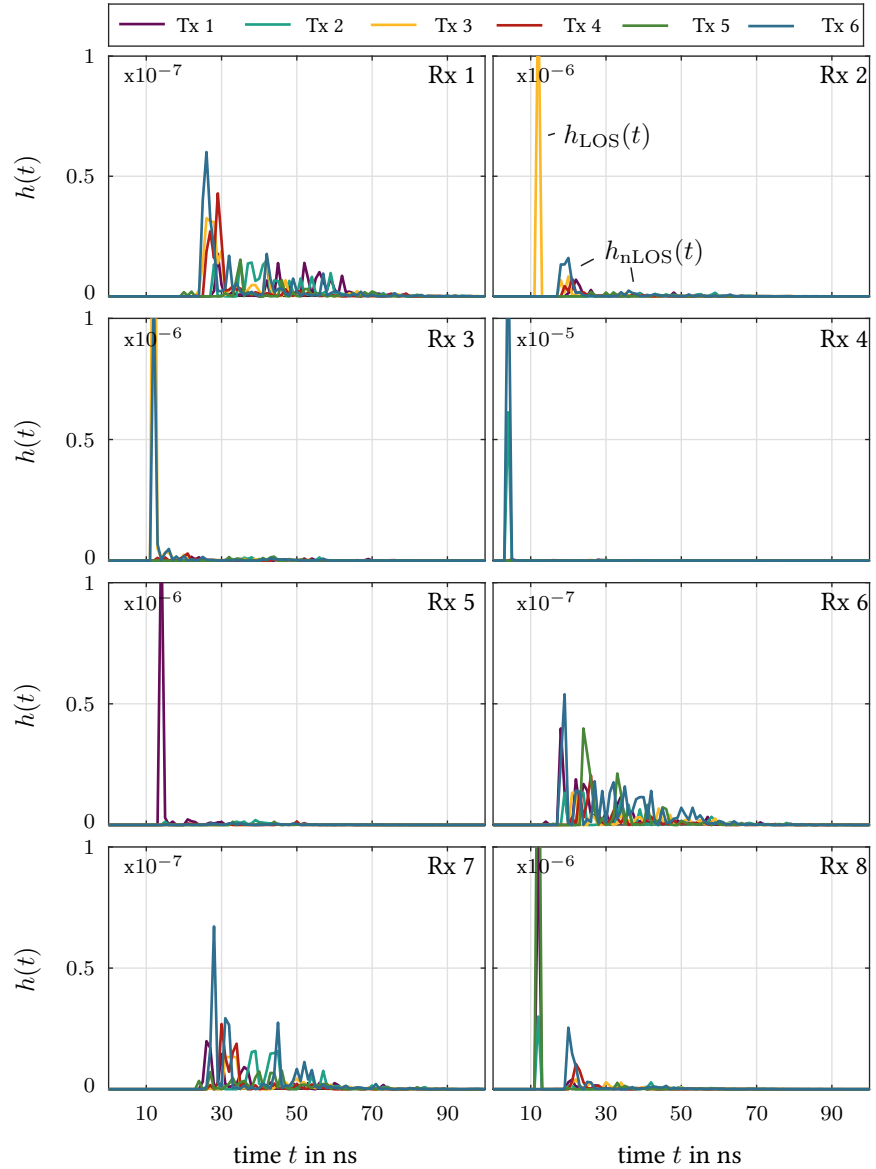


Figure 2.7: Time-domain samples of the simulation results in [95]. The graphs represent the CIRs resulting from the dispersed received optical power at multiple Rxs. Note the different scaling of the vertical axes as indicated in the upper left of each plot.

in Fig. 2.6a and Fig. 2.6b, respectively. Both show two production robots placed within a manufacturing cell, whose boundary is highlighted in blue. Raytracing was performed for six Txs mounted on the head of *robot 1* and eight Rxs positioned around the cell. Their positions are marked in Fig. 2.6b. Since the simulated scenario corresponds to an application of OWC in an industrial environment and therefore covers the same application this work is focused on, we now briefly analyse the published CIRs and their frequency-domain equivalents. With six Txs and eight Rxs a total of 48 individual spatial channels were simulated.

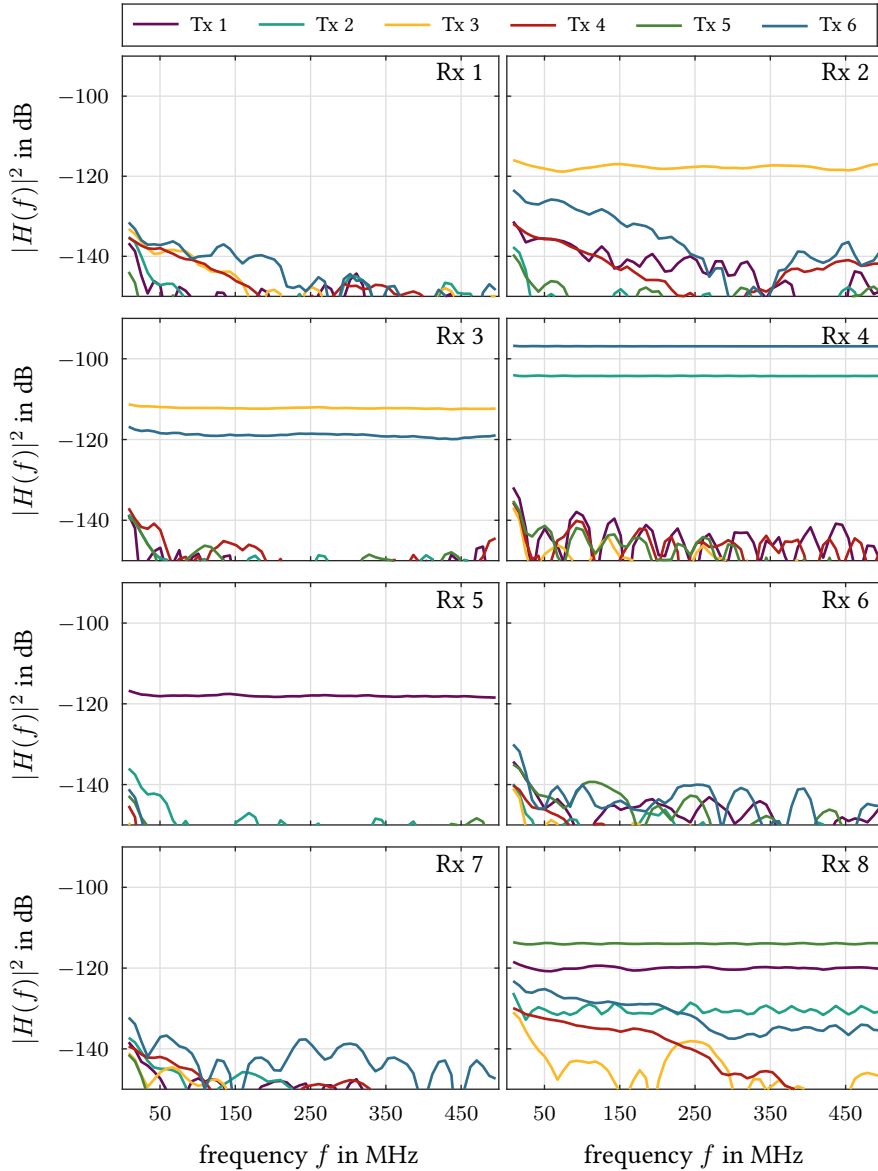


Figure 2.8: Frequency-domain representation of the simulation results in [95]. The graphs represent the frequency response as seen by multiple Rxs.

The resulting channel responses as given in [96] are shown in Fig. 2.7. The CIRs as seen by each of the eight Rxs are shown in separate subplots. Different colors indicate the source Tx. When a LOS is available, a significantly stronger peak can be observed (see Rxs 2, 3, 4, 5 and 8). Due to the proximity of the six Txs we may expect that LOS components arrive simultaneously at a single Rx, an effect that is visible for the Rxs 3, 4 and 8. Subsequent pulses as in the graphs of Rx 2 can be attributed to nLOS components. We observe that for non-zero LOS components, the power  $P_{\text{LOS}} \propto \int h_{\text{LOS}}(t)dt$  transported by the LOS component is significantly larger than the power  $P_{\text{nLOS}} \propto \int h_{\text{nLOS}}(t)dt$  transported by the nLOS component.

Figure 2.8 shows the magnitude of the frequency-domain responses in dB. Here, channels with a non-zero LOS component do not only show the largest

magnitudes, but additionally exhibit flat frequency responses over a large bandwidth. The large difference in magnitude between channels with a LOS component and pure nLOS channels, becomes increasingly important when considering LOS blocking elements encountered in factories. Considering detector diameters in the range of 1 cm and fast movement above 1 m/s, blocking can lead to abrupt channel changes in the order of multiple dB per millisecond. This can result in failed packet deliveries and thus potentially increased latencies. In case of the presented simulations, all LOS of Rx 1 are blocked by the Tx-carrying *robot 1* itself. For Rxs 6 and 7 blocking is caused by *robot 2*.

An important question, which will be left unanswered in this chapter, is whether weak signals undergoing a reflection are detectable or become indistinguishable from additive noise signals. As this depends on a multitude of factors, such as the transmit power, signal bandwidth, Rx noise and the geometrical and reflective properties of the environment, an answer would be site- and device-dependent. Nevertheless, for a similar manufacturing cell<sup>5</sup>, channel measurements were conducted with our front ends and the results presented in Chapter 4 indicate that only LOS channels were detectable.

### 2.2.3 Multiple-Input Multiple-Output Channel

The CIRs presented in the previous section were seen as a variety of individual channels between single TxS and single RxS. Alternatively, the union of these 48 exemplary spatial channels may also be interpreted as a single channel with multiple inputs and multiple outputs. Understandably, such channels are commonly referred to as multiple-input multiple-output (MIMO) channels. By indexing the multiple CIRs and TxS/RxS, we can extend Eq. (2.17) to describe the MIMO channel:

$$y_m(t) = \sum_{n=1}^N h_{m,n}(t) * x_n(t) + n_m(t) \quad (2.19)$$

For a total of  $N$  TxS and  $M$  RxS,  $n \in \mathbb{N} : 1 \leq n \leq N$  and  $m \in \mathbb{N} : 1 \leq m \leq M$  are used to index the TxS and RxS, respectively. Consequently,  $x_n(t)$  denotes the signal transmitted by the  $n$ -th Tx,  $h_{m,n}(t)$  the CIR from the  $n$ -th Tx to the  $m$ -th Rx and  $y_m(t)$  and  $n_m(t)$  denote the overall received signal and noise at the  $m$ -th Rx.

To ultimately result in a simpler notation, we now consider the discrete-time equivalent of Eq. (2.19), sampled at a rate  $R_s \geq 2B$ , where  $B$  is the bandwidth of the bandwidth-limited signals<sup>6</sup>. The sample period is  $T_s = 1/R_s$  and the discrete-time index is denoted by  $k$ :

$$y_m[k] = \sum_{n=1}^N h_{m,n}[k] * x_n[k] + n_m[k] \quad (2.20)$$

<sup>5</sup> The manufacturing cell shown in Fig. 2.6 had been disassembled at the time of the channel measurements and all measurements discussed in this thesis were conducted in a second cell introduced in Chapter 4.

<sup>6</sup> If the signals are not inherently bandwidth-limited, we assume bandwidth limitation with an anti-aliasing filter at the Rx.

The discrete-time equivalents result as  $y_m[k] = y_m(kT_s)$ ,  $n_m[k] = n_m(kT_s)$ ,  $x_n[k] = x_n(kT_s)$  and  $h_{m,n}[k] = h_{m,n}(kT_s)$ . For a CIR with finite memory  $N_{\text{IR}}$ , the discrete-time convolution in Eq. (2.20) can be applied in blocks of length  $N_{\text{DFT}} \geq N_{\text{IR}}$  with methods such as *overlap-add* or *overlap-save*, which can be implemented efficiently by computing the circular convolution within these blocks based on the discrete Fourier transform (DFT) [76]. Applied over  $N_{\text{DFT}}$  samples of the transmit signal  $x[k]$ , the DFT is defined as

$$X_m[l] = \sum_{k=1}^{N_{\text{DFT}}} x_m[k] e^{-\frac{2\pi j}{N_{\text{DFT}}}(k-1)(l-1)}, \quad (2.21)$$

with  $l \in \mathbb{N} : 1 \leq l \leq N_{\text{DFT}}$  and is computed analogously for the noise signal. After padding the CIR of length  $N_{\text{IR}}$  with  $N_{\text{DFT}} - N_{\text{IR}}$  zeros, its coefficients in the frequency-domain are given by

$$H_{m,n}[l] = \sum_{k=1}^{N_{\text{DFT}}} h_{m,n}[k] e^{-\frac{2\pi j}{N_{\text{DFT}}}(k-1)(l-1)}. \quad (2.22)$$

Making use of the periodic convolution property of the DFT [76], for each block of  $N_{\text{DFT}}$  samples, Eq. (2.20) results in

$$Y_m[l] = \sum_{n=1}^N H_{m,n}[l] X_n[l] + N_m[l], \quad (2.23)$$

where the capitalized variables are the DFT of the corresponding lower-case variables. Even though Eq. (2.20) and Eq. (2.23) look similar, note that the latter contains no convolution, but a simple multiplication. Therefore, Eq. (2.23) can also be written in matrix form:

$$\mathbf{y}[l] = \mathbf{H}[l]\mathbf{x}[l] + \mathbf{n}[l] \quad (2.24)$$

Here,  $\mathbf{H}$  is the  $M \times N$  channel matrix with  $H_{m,n}[l]$  as its entries. The signal vectors are given as  $\mathbf{x} = [X_1[l], \dots, X_N[l]]^T$ ,  $\mathbf{y} = [Y_1[l], \dots, Y_M[l]]^T$  and  $\mathbf{n} = [N_1[l], \dots, N_M[l]]^T$ , where  $[\cdot]^T$  denotes the matrix transpose. For a given sample rate  $R_s$  and DFT size  $N_{\text{DFT}}$ , Eq. (2.24) describes the MIMO channel as manifested at a physical frequency

$$f_l = \begin{cases} \frac{R_s}{N_{\text{DFT}}} \cdot (l-1), & \text{for } l \leq \left\lceil \frac{N_{\text{DFT}}}{2} \right\rceil, \\ \frac{R_s}{N_{\text{DFT}}} \cdot (1-l + N_{\text{DFT}}), & \text{otherwise.} \end{cases} \quad (2.25)$$

While Chapter 4 is dedicated to the measurement of  $\mathbf{H}$  within an industrial manufacturing environment, the subsequent Chapter 5 discusses how MIMO channels can be exploited to design an OWC system with increased physical layer reliability. Prior to the experimental validation in the laboratory and manufacturing environment, however, the proposed concepts are tested for feasibility with LOS-MIMO simulations. Since LOS components deliver most of the signal power, we expect the blocking thereof to have a severe impact on the reliability of the communication system and thus include a LOS blocking model in the simulations. Therefore Eq. (2.16) is expanded by a blocking

function, which incorporates the impact of LOS-blockage between the  $n$ -th Tx and the  $m$ -th Rx:

$$h_{m,n}(t) = \frac{1}{d_{m,n}^2} \cdot R_0(\theta_{t,n}) \cdot A_{\text{eff}}(\theta_{r,m}) \cdot \delta(t - \tau_{m,n}) \cdot B(\mathbf{p}_{t,n}, \mathbf{p}_{r,m}) \quad (2.26)$$

The function  $B(\mathbf{p}_{t,n}, \mathbf{p}_{r,m})$  is 1 when the LOS between the points  $\mathbf{p}_{t,n}$  and  $\mathbf{p}_{r,m}$  is unobstructed and 0 when an obstacle nulls the channel transmission coefficient. In raytracing, the interception of a ray with a spherical obstacle is calculated fairly easily. In order to keep the raytracing complexity of this simulator low, the functions  $B(\mathbf{p}_{t,n}, \mathbf{p}_{r,m})$  used for the simulations in this thesis, are determined thus solely by multiple spheres with variable radius.

### 2.3 WAVEFORMS AND DIGITAL SIGNAL PROCESSING

As mentioned in the introduction, OWC has triggered numerous publications related to the investigation of existing and creation of new waveforms compatible with the non-negativity constraint of the IM/DD channel. While some are designed for maximization of the IM/DD channel capacity [28]–[30], [33], others focus on the robustness against multipath distortion based on multi-carrier approaches [24], [25], [34], [36]. Simplicity is another focus, usually claimed by baseband modulation formats such as early used on/off keying (OOK) [1], [97]. However, the simplicity of OOK comes at the cost of limited adaption capabilities to the time-varying channel. In this work we consider the widely used direct-current biased optical (DCO) orthogonal frequency-division multiplexing (OFDM) and single-carrier (SC) quadrature amplitude modulation (QAM) at an intermediate frequency. They are both chosen, for being well understood and their property of generating direct-current (DC) free waveforms at the output of the DAC. This is particularly useful when handling alternating current (AC)-coupled devices, such as our TRxs. While DCO-OFDM provides robustness against multipath distortions, SC-QAM provides better peak-to-average power ratios (PAPRs).

In the following we briefly introduce these two waveforms, the associated DSP building blocks and its parametrization used for the simulations and experiments to follow.

#### 2.3.1 *Direct-Current Biased Optical Orthogonal Frequency-Division-Multiplexing*

A common and simple approach for OWC is the use of a multi-carrier approach such as DCO-OFDM, in which an OFDM signal is generated and a DC added to modulate the LED around a certain bias point. Even though this approach neglects the impact of clipping for negative values of the waveform, its advantage lies in the simplicity of its implementation based on the well-studied OFDM waveform.

Figure 2.9a outlines a P2P system concept based on IM/DD, which employs DCO-OFDM. Source bits are encoded with a low-density parity-check (LDPC) FEC of variable rate  $R_{\text{FEC}}$  [98] and serial-to-parallel (SP) conversion is performed. The parallel bit streams corresponding to different subcarriers,

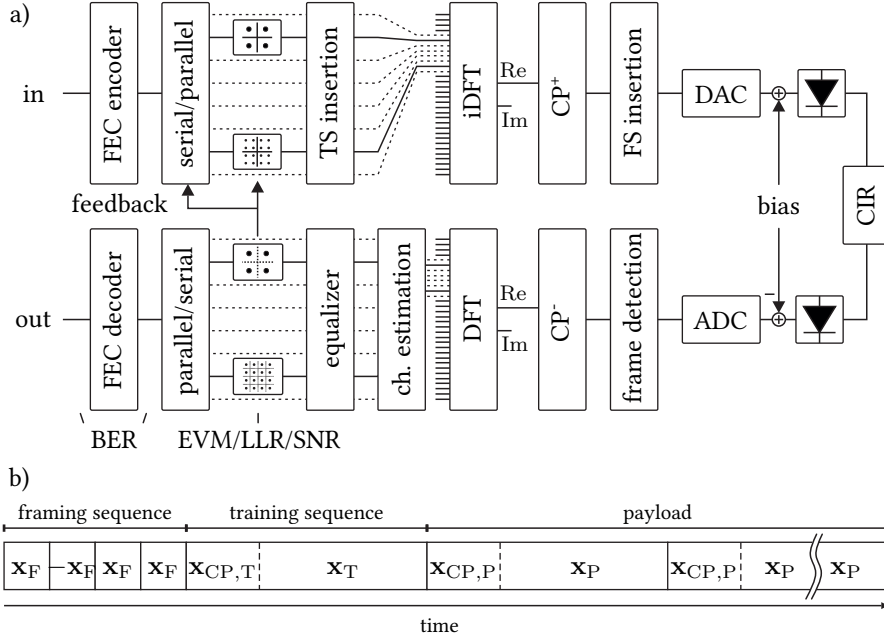


Figure 2.9: a) Block diagram of the DCO-OFDM DSP employed in the experiments and simulations. b) Structure of an OFDM frame, which starts with a FS for detection of the frame start and is followed by a TS for estimation of the CIR and the information-carrying payload.

are each (quasi-)Gray-mapped [99] onto complex constellations of unit power, commonly from the binary phase-shift keying (BPSK), quadrature phase-shift keying (QPSK) or QAM alphabets [100], [101]. This results in complex-valued payload symbols. For later channel estimation and channel equalization, training sequences (TSs) are inserted thereafter<sup>7</sup>. These consist of symbols from the QPSK alphabet and are known to the Rx. (De-)Multiplexing of different subcarriers is commonly performed by the DFT<sup>8</sup>. We define the DFT operating on the input signal  $x[k]$  and yielding the output  $X[l]$  identically to Eq. (2.21):

$$X[l] = \sum_{k=1}^{N_{\text{DFT}}} x[k] e^{-\frac{2\pi j}{N_{\text{DFT}}}(k-1)(l-1)} \quad (2.27)$$

Correspondingly, the inverse discrete Fourier transform (iDFT) is defined as

$$x[k] = \frac{1}{N_{\text{DFT}}} \sum_{l=1}^{N_{\text{DFT}}} X[l] e^{\frac{2\pi j}{N_{\text{DFT}}}(k-1)(l-1)}. \quad (2.28)$$

At the Tx, the complex symbols and TSs are fed to an iDFT. In order to create a real-valued waveform suitable for transmission over an IM/DD channel, a conjugate symmetry is often imposed on the inputs of the iDFT [25], [70], [101]. Alternatively, we can simply limit the Tx to use at most half of the subcarriers corresponding to either positive or negative frequencies and

<sup>7</sup> Here, only the P2P case is shown. However, MIMO TSs as in Section 4.1.2 may also be inserted.

<sup>8</sup> The DFT is commonly realized with the efficient implementation called fast Fourier transform (FFT). It is particularly efficient when the DFT size  $N_{\text{DFT}}$  is an integer power of two [101].

discard the output of the iDFT's imaginary part. Thus, whenever DCO-OFDM is employed in simulations or experiments, the subset of subcarriers  $\mathcal{S} \subset \{l \in \mathbb{N} : 1, \dots, N_{\text{DFT}}/2 - 1\}$  used for data transmission is stated. At the output of the iDFT, we obtain a block of  $N_{\text{DFT}}$  samples  $\mathbf{x}$ , whose entries  $x[k]$ <sup>9</sup> are

$$x[k] = 2 \cdot \text{Re} \left\{ \frac{1}{N_{\text{DFT}}} \sum_{l \in \mathcal{S}} X[l] e^{\frac{2\pi j}{N_{\text{DFT}}}(k-1)(l-1)} \right\}. \quad (2.29)$$

In order to make OFDM robust against ISI, a guard interval of  $N_{\text{CP}}$  samples in form of a cyclic prefix (CP) is prepended to the block of samples  $\mathbf{x}$ . For  $1 \leq N_{\text{CP}} \leq N_{\text{DFT}}$ , this results in the block of  $N_{\text{DFT}} + N_{\text{CP}}$  samples

$$\mathbf{x}' = \underbrace{[x[N_{\text{DFT}} - N_{\text{CP}} + 1], \dots, x[N_{\text{DFT}}]]}_{\mathbf{x}_{\text{CP}}} \underbrace{[x[1], \dots, x[N_{\text{DFT}}]]}_{\mathbf{x}}. \quad (2.30)$$

The block of samples  $\mathbf{x}'$  is called an OFDM symbol and for a sample rate  $R_s$  has a duration of  $T_{\mathbf{x}'} = (N_{\text{DFT}} + N_{\text{CP}})/R_s$ . For a finite memory of the CIR  $T_{\text{IR}}$ , the CP is ideally chosen such that  $N_{\text{CP}}/R_s \geq T_{\text{IR}}$ . Multiple OFDM symbols are prepended with a framing sequence (FS). We call this logical unit a *frame*, whose structure is shown in Fig. 2.9b. It contains OFDM symbols corresponding to the payload data, TSs and a FS, which are denoted by the subscripts P, T and F, respectively. The fraction of the frame occupied by the TS and FS with respect to the entire duration is called overhead (OH). The FS itself is a repetition of a single sub-sequence with varying sign. These known sign variations allow for a robust detection at the Rx by a modified auto-correlation [102]. We employ FSs inspired by the ITU-T G.hn recommendations [98], which are in essence a concatenation of a shorter OFDM symbol with varying sign and no CP.

The resulting digital samples are then converted into the analog domain, a DC bias is added and the overall signal is modulated onto the optical power of the LED, resulting in the DCO-OFDM waveform. After passing through a channel described by its CIR, the optical power is detected by a PD and hereby converted into the electrical domain. The DC bias is removed and the signal is digitized with an ADC.

Due to its high flexibility, we use the detector suggested in [102] to detect the FS and thus the beginning of a frame. Subsequently, the OFDM blocks are processed individually, starting with the removal of the CP, followed by the demultiplexing via an DFT. The first OFDM symbols are the TSs containing known complex pilot symbols its subcarriers. Based on these known symbols, channel estimation [103] and channel interpolation is performed [104]. Based on the estimated channel, single-tap zero-forcing (ZF) equalization is applied [103], followed by the demodulation of each subcarrier. Here, error-vector magnitude (EVM) and from it the SNR and log-likelihood ratios (LLRs) are derived. The SNR is fed back to the Tx and may be used for adaptation to the channel via bit and power loading (BPL). If employed, BPL is performed according to [105]. After serialization of the multiple streams, the LLRs are used to either calculate a pre-FEC bit error rate (BER) or post-FEC BER after soft-decision decoding.

<sup>9</sup> Note the *sans-serif* font to differentiate  $x$  in Eq. (2.29) from  $x$  in Eq. (2.28).

The simulations and experiments based on DCO-OFDM will follow the structure shown in Fig. 2.9a and differ only in the exact parameters used. Thus, at the beginning of a simulation or experimental test, the relevant parameters will be provided in a table:

Table 2.1: List of varying DCO-OFDM DSP parameters.

symbol	description	typical value(s)
$N_{\text{DFT}}$	size of DFT	2048
$\mathcal{S}$	subset of subcarriers used for transmission	5-1020
$N_{\text{CP}}$	size of CP	128
$\mathcal{M}$	cardinalities of constellations	2,4,16,32,64,128,512,1024,2048,4096
$R_s$	DAC/ADC sampling rate	500 MS/s
OH	DSP overhead	2-20%
BPL	type of BPL, if used	Krongold
FEC	type of FEC, if used	LDPC
$R_{\text{FEC}}$	FEC rate, if used	5/6
$G_{\text{phy,g}}$	gross physical layer throughput	up to 291 Mb/s

### 2.3.2 Single-Carrier on Intermediate Frequency

The second waveform of interest is that of a single-carrier (SC) modulated with a format such as QPSK or QAM and digitally upconverted to an intermediate frequency  $f_c$  in the MHz range. Its advantage lies in the reduced PAPR and thus higher *optical signal power*<sup>10</sup> compared to DCO-OFDM for equal peak-power constraint such as imposed by the limited dynamic range of an DAC or the non-negativity of the IM/DD channel. Just as with DCO-OFDM, a DC bias is added to avoid clipping due to the IM/DD channel.

Figure 2.10a outlines the P2P IM/DD system using a SC-QAM waveform. Source bits are encoded with a LDPC FEC or variable rate  $R_{\text{FEC}}$  [98]. The resulting bits are (quasi-)Gray-mapped [99] to a complex constellation, from the QPSK<sup>11</sup> and QAM symbol alphabets [100], [101]. For later channel estimation, a constant-amplitude zero-autocorrelation (CAZAC) TS [106] is inserted together with a FS for the detection of a frame and the extraction of the TS at the Rx. For SC-QAM, the subsequence of the FS is a sequence of QPSK symbols obtained from a pseudo-random bit sequence (PRBS). All symbols are shaped with a root-raised-cosine (RRC) pulse shape with a roll-off parameter  $\beta$  [100]. Here, pulse shaping includes up-sampling from an incoming symbol rate  $R_{\text{sy}}$  to the target sample rate  $R_s$ . The spectrally shaped complex-baseband signal is upconverted to the intermediate frequency  $f_c$ , which results in a real-valued, DC-free waveform. Note that the integration of the upconversion into the pulse shape, results in the equivalent carrier-less amplitude/phase modulation (CAP) format studied for OWC in [14], [31].

<sup>10</sup> See end of Section 2.2.1 for a differentiation between *optical signal power* and *average optical power*.

<sup>11</sup> As QPSK can be seen as a type of QAM, we will continue referring to the waveform as SC-QAM.

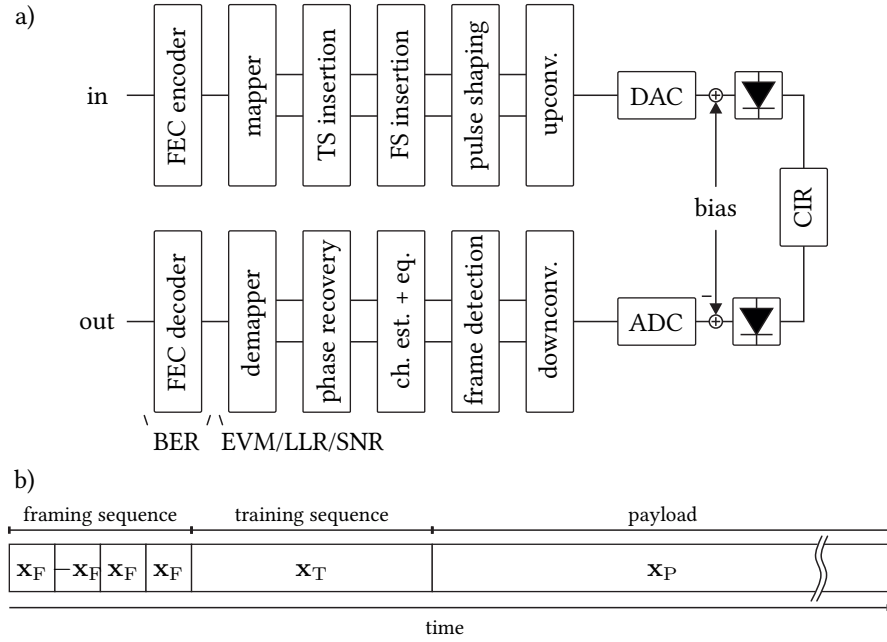


Figure 2.10: a) Block diagram of the SC-QAM DSP employed in the experiments and simulations. b) Structure of an SC-QAM frame, which starts with a FS for detection of the frame start and is followed by a TS for estimation of the CIR and the information-carrying payload symbols.

Conversion into the analog domain is performed by a DAC and a DC bias is added, to avoid clipping due to the IM/DD channel's non-negativity constraint. After E/O conversion with an LED, we obtain the SC-QAM waveform in the optical domain. After passing through a channel determined by its CIR, the optical power is detected by a PD and hereby converted into the electrical domain. The DC bias is removed and the signal is digitized with an ADC.

The signal is digitally downconverted back to the complex-baseband, where framing detection performed as for the OFDM toolchain with the detector suggested in [102]. Frequency-domain least squares (LS) channel estimation [107] is performed and minimum mean square error (MMSE) equalization is performed based on this estimate [108]. Although the baseband IM/DD channel is very frequency-stable and does not require any carrier frequency recovery, phase recovery is useful when Tx and Rx are not fully synchronized or when nonlinearly distorted TS result in a constant misalignment of the payload data. In that case a phase recovery as in [109] is employed. After phase recovery, demapping and EVM estimation is performed. This in turn is used for the estimation of SNR and LLRs. Subsequently, pre- and post-FEC BERs can be estimated.

The simulations and experiments based on SC-OFDM will follow the structure shown in Fig. 2.10a and differ only in the exact parameters used. Thus, at the beginning of a simulation or experimental test, the system defining parameters will be provided in a table:

Table 2.2: List of varying SC-QAM DSP parameters.

symbol	description	typical value(s)
$f_c$	intermediate frequency	$\approx R_s/4$
PS	pulse shape and roll-off	RRC
$R_{sy}$	symbol rate	$< R_s/2$
$\mathcal{M}$	cardinality of constellation	4,16,64,256
$R_s$	DAC/ADC sampling rate	500 MHz
BW	TRx bandwidths	20-200 MHz
OH	DSP overhead	2-20%
FEC	type of FEC, if used	LDPC
$R_{FEC}$	FEC rate, if used	5/6
$G_{phy,n}$	net physical layer throughput	1-200 Mb/s



In this chapter we look into the conceptually straight-forward approach of improving coverage by increasing the transmitter (Tx) *optical signal power*  $\tilde{P}$ . This optical signal power  $\tilde{P}$  may be increased by using larger *electrical signal powers*  $\tilde{P}_e$  to drive the Tx *light-emitting diode* (LED), which in turn may cause nonlinear excitation of the LED. This behavior and first linearization techniques with analog circuitry were observed and proposed in 1978 already [110], [111]. Works within the last decade have investigated other means to mitigate LED nonlinearities such as the use of multiple Tx [112] for reduced per-Tx transmit power or the use of *digital signal processing* (DSP) at the Tx [113]–[115] or *receiver* (Rx) [14], [116], [117].

Motivated by the promising gains of nonlinear compensation schemes reported in these previous works, we investigate the use of a receive-side and data-aided *nonlinear post-equalizer* (NLPE) designed for wireless industrial communication: Equalization at the Rx is chosen as it does not require additional feedback. This makes the approach, first presented in [118], less susceptible to outdated *channel state information* (CSI), which would trigger re-transmissions of unrecoverable packets and thus increase the delivery latency of such packets. The data-aided nature of the suggested NLPE is based on *nonlinear training sequences* (NLTs) known a priori, removing the need of an adaptation across the payload and is thus particularly suitable for the reception of bursty traffic common in wireless networks. Since the NLTs can be chosen independently of the waveform used for the payload, this NLPE can be combined with any waveform commonly used in *optical wireless communication* (OWC). Here, its applicability to *single-carrier* (SC)-*quadrature amplitude modulation* (QAM) and *direct-current biased optical* (DCO)-*orthogonal frequency-division multiplexing* (OFDM) is demonstrated.

As the NLPE is based on the Volterra series, we briefly review the Volterra series' definition and show how it can be used to model the nonlinear behavior of the OWC system, prior to discussing its application as nonlinear compensator.

### 3.1 NONLINEAR SYSTEM DESCRIPTION AND ESTIMATION

The Volterra series is a widely used tool for the description of a family of nonlinear systems [119]–[124]. With a goal of ultimately designing a digital compensation scheme, we consider its discrete-time variant  $V\{\cdot\}$  with limited

memory and limited order  $Q$ . Operating on an input signal  $x[k]$  around a time instant  $k$ , it yields a noise-free distorted signal  $d[k]$  as [123]

$$\begin{aligned} d[k] &= V\{x[k]\} \\ &= v_0 + \sum_{q=1}^Q \underbrace{V_q\{x[k]\}}_{d_q[k]}. \end{aligned} \quad (3.1)$$

As a part of the Volterra series, the scalar  $v_0$  is the zeroth order kernel. The individual Volterra operators  $V_q\{\cdot\}$  of order  $q$  operate on  $x[k]$  as follows:

$$\begin{aligned} d_q[k] &= V_q\{x[k]\} \\ &= \sum_{k_1, \dots, k_q=1}^{m_q} v_q[k_1, \dots, k_q] \cdot \underbrace{\prod_{i=1}^q x[k - k_i - \kappa_q]}_{\text{nonlinear expansion}} \end{aligned} \quad (3.2)$$

The overall Volterra series of a nonlinear system is thus fully determined by its kernels  $v_q$ , which each have a limited memory  $m_q$ . The order dependent sample delays  $\kappa_q$  are used to align the higher order kernels centric to the first order one. Note that Eq. (3.2) shows how the nonlinearity is rooted in the nonlinear expansion of the input signal. When written like this, each kernel  $v_q$  is determined by a total of  $N_c = m_q^q$  coefficients and the number of coefficients increases drastically for larger memories and higher order. However, since the nonlinear expansion of  $x[k]$  is highly symmetrical, some coefficients are redundant. In order to highlight these symmetries, we evaluate Eq. (3.2) for the simple case of  $q = 2$ ,  $m_2 = 2$  and  $\kappa_2 = 0$ :

$$\begin{aligned} d_2[k] &= v_2[1, 1] \cdot x[k-1] \cdot x[k-1] + v_2[1, 2] \cdot x[k-1] \cdot x[k-2] \\ &\quad + v_2[2, 1] \cdot x[k-2] \cdot x[k-1] + v_2[2, 2] \cdot x[k-2] \cdot x[k-2] \end{aligned} \quad (3.3)$$

While the kernel coefficients  $v_2[1, 1]$  and  $v_2[2, 2]$  are unique, the kernel coefficients  $v_2[1, 2]$  and  $v_2[2, 1]$  are related to the identical nonlinear expansion of input samples  $x[k-1]x[k-2] = x[k-2]x[k-1]$  and without loss of generality may be assumed to be equal. It is thus possible to define slightly different Volterra kernels<sup>1</sup>  $v_q$ , which do not include any redundant terms. Our example then simplifies to

$$\begin{aligned} d_2[k] &= v_2[1, 1] \cdot x[k-1] \cdot x[k-1] + v_2[1, 2] \cdot x[k-1] \cdot x[k-2] \\ &\quad + v_2[2, 2] \cdot x[k-2] \cdot x[k-2]. \end{aligned} \quad (3.4)$$

Note that in this case this means  $v_q[1, 2] = v_q[1, 2] + v_q[2, 1]$  or simply  $v_q[1, 2] = 2 \cdot v_q[1, 2]$  if  $v_q[1, 2] = v_q[2, 1]$ . The modified Volterra kernels  $v_q$  are simply incorporated, if the Volterra operators  $V_q\{\cdot\}$  are written as

$$\begin{aligned} d_q[k] &= V_q\{x[k]\} \\ &= \sum_{k_1=1}^{m_q} \cdots \sum_{k_q=k_{q-1}}^{m_q} v_q[k_1, \dots, k_q] \cdot \underbrace{\prod_{i=1}^q x[k - k_i - \kappa_q]}_{\text{nonlinear expansion}}. \end{aligned} \quad (3.5)$$

<sup>1</sup> Note the sans-serif font for the kernel  $v_q$  including redundant coefficients and the font with serifs for the kernel  $v_q$  without redundant terms. Their similarity is intended due to their nearly identical meaning and should not cause confusion, since  $v_q$  will not be used henceforth.

The number of coefficients is thus reduced to  $N_c = \binom{q+m_q-1}{q}$  [125]. This difference is illustrated next to this paragraph for the case of third order kernels. Ultimately, we are interested in the coefficients of the kernels  $v_q$ , which determine the nonlinearities in an OWC system. Therefore, in the next few paragraphs we elaborate on how such kernels can be estimated from noisy observations and later discuss how a similar approach allows us to design an NLPE to approximately linearize the nonlinear system. We thus consider the noisy observation

$$y[k] = d[k] + n[k], \quad (3.6)$$

where  $n[k]$  is additive noise e.g. due to our measurement equipment or Rx components. To describe the estimation problem, the description of the previous equations in matrix notation is helpful [122], [123]. We consider the column vector  $\mathbf{x}_q[k]$ , whose entries are the unique nonlinear expansions in Eq. (3.5), and the column vector  $\mathbf{v}_q$ , whose entries are the corresponding unique kernel coefficients given by  $v_q$ . For the previous simple example, this results in

$$\mathbf{x}_2[k] = \begin{bmatrix} x[k-1]x[k-1] \\ x[k-1]x[k-2] \\ x[k-2]x[k-2] \end{bmatrix} \quad (3.7)$$

and

$$\mathbf{v}_2 = \begin{bmatrix} v_2[1, 1] \\ v_2[1, 2] \\ v_2[2, 2] \end{bmatrix}. \quad (3.8)$$

With such notation, we can proceed to rewrite Eq. (3.4) as

$$d_2[k] = \mathbf{x}_2[k]^\top \mathbf{v}_2, \quad (3.9)$$

where  $[\cdot]^\top$  denotes the matrix transpose. Equivalently, for the general equation Eq. (3.5) the Volterra operator can be represented by the following matrix product:

$$d_q[k] = \mathbf{x}_q[k]^\top \mathbf{v}_q \quad (3.10)$$

In order to capture all orders, we define the signal vector containing all nonlinear expansions

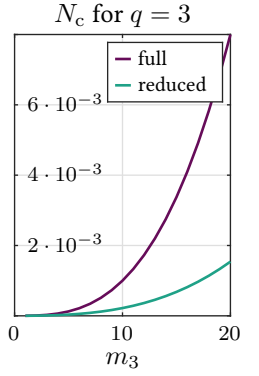
$$\mathbf{x}[k] = \begin{bmatrix} 1 \\ \mathbf{x}_1[k] \\ \vdots \\ \mathbf{x}_Q[k] \end{bmatrix} \quad (3.11)$$

and similarly a vector containing all kernel coefficients

$$\mathbf{v} = \begin{bmatrix} v_0 \\ \mathbf{v}_1 \\ \vdots \\ \mathbf{v}_Q \end{bmatrix}, \quad (3.12)$$

resulting in the matrix representation of Eq. (3.1)

$$d[k] = \mathbf{x}[k]^\top \mathbf{v}. \quad (3.13)$$



Exemplary number of coefficients  $N_c$  in the third order kernels  $v_3$  (full) and  $v_3$  (reduced) for varying memory lengths  $m_3$ .

In order to estimate the coefficients of all kernels  $v_q$  from a total of  $N_o$  consecutive noisy observations via a least squares (LS) fit, we additionally define a vector of received noisy samples  $\mathbf{y} = [y[k], \dots, y[k + N_o - 1]]^\top$ , a vector of noise samples  $\mathbf{n} = [n[k], \dots, n[k + N_o - 1]]^\top$  and the matrix  $\mathbf{X} = [\mathbf{x}[k], \dots, \mathbf{x}[k + N_o - 1]]^\top$ , which contains all nonlinear expansions of the original signal at multiple time instances. All  $N_o$  noisy observations may then be written compactly as

$$\mathbf{y} = \mathbf{X}\mathbf{v} + \mathbf{n}. \quad (3.14)$$

A simple way to estimate all kernel coefficients contained in  $\mathbf{v}$  is to solve the LS optimization problem, which may be written as

$$\hat{\mathbf{v}} = \underset{\mathbf{v}}{\operatorname{argmin}} \|\mathbf{y} - \mathbf{X}\mathbf{v}\|_2^2. \quad (3.15)$$

For invertible  $\mathbf{X}^\top \mathbf{X}$ , the estimate  $\hat{\mathbf{v}}$  is given by [122], [123]

$$\hat{\mathbf{v}} = (\mathbf{X}^\top \mathbf{X})^{-1} \mathbf{X}^\top \mathbf{y}. \quad (3.16)$$

For ill-posed identification problems, invertibility may be improved through the concept of regularization, out of which *penalization* is a common approach [126]. The optimization problem for a penalized least squares (PLS) problem is then [122]

$$\hat{\mathbf{v}} = \underset{\mathbf{v}}{\operatorname{argmin}} \|\mathbf{y} - \mathbf{X}\mathbf{v}\|_2^2 + \lambda J(\mathbf{v}), \quad \text{with } \lambda \geq 0. \quad (3.17)$$

Here,  $\lambda$  is the regularization parameter and  $J(\mathbf{v})$  is the non-negative penalizing function, which should be chosen to penalize unlikely solutions. For simplicity, we assume a penalizing functional of quadratic shape, i.e.  $J(\mathbf{v}) = \mathbf{v}^\top \mathcal{R} \mathbf{v}$ , where  $\mathcal{R}$  is a symmetric, positive semidefinite matrix, whose eigenvectors should span the subspace to be penalized. The unique minimizer is then given by [122]

$$\hat{\mathbf{v}} = (\mathbf{X}^\top \mathbf{X} + \lambda \mathcal{R})^{-1} \mathbf{X}^\top \mathbf{y}. \quad (3.18)$$

Note that for  $\lambda = 0$ , the solution of the PLS and LS estimators are identical. A thorough discussion on the exact shape of  $\mathcal{R}$  suitable for nonlinear identification is given in [122]. While a repetition of this analysis is not necessary for the sole purpose of applying the PLS estimator, an explanation of how its building blocks were constructed for the following measurements, should be provided for reproducibility. As stated in [122],  $\mathcal{R}$  is composed of sub-matrices<sup>2</sup>  $\mathbf{R}_q$  for each order  $q$ . Inspired by [123], [125] we set to  $\mathbf{R}_q = \mathbf{I}_q - \mathbf{D}_q$ , where  $\mathbf{I}_q$  is the  $m_q \times m_q$  identity matrix and  $\mathbf{D}$  a  $m_q \times m_q$  diagonal matrix whose elements contain the first  $m_q$  coefficients of the auto-correlation with unit power of  $x[k]$ . This way, the kernel subspace, which is stimulated mostly by a noise signal, can be penalized. Using an PLS estimator can thus lead to more stable estimates  $\hat{\mathbf{v}}$  at lower signal-to-noise ratios (SNRs).

<sup>2</sup> In [122] simply denoted as  $\mathbf{R}$  since it is explained for a single order  $q$  only.

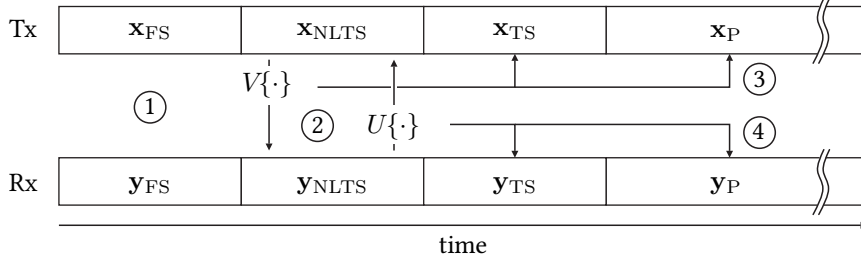


Figure 3.1: Frame structure used in the experiments for the estimation of the nonlinear OWC system  $V\{\cdot\}$  or its NLPE  $U\{\cdot\}$ . The numbers indicate selected steps required in the estimation/compensation process.

Eqs. (3.16) and (3.18) show how the kernels of a nonlinear system can be estimated with known input and output sequences, which in a communication system we may obtain via the insertion of known NLTSs. The following section shows results on an identified nonlinear OWC system and discusses when nonlinear compensation may be of use. Further, an NLPE capable of mitigating the impact of nonlinear effects is presented and validated in SC-QAM and DCO-OFDM transmission experiments.

### 3.2 NONLINEAR POST-EQUALIZER

While the DSP toolchain slightly differs between SC-QAM and DCO-OFDM, the methodology for nonlinear compensation is identical. Fig. 3.1 thus shows the generic frame structure applicable to both waveforms. In a first step, the received frame is aligned to the transmitted frame using a framing sequence (FS) introduced in Section 2.3. As an extension for the NLPE, an NLTS is inserted after the FS and prior to the training sequence (TS) already intended for linear equalization. This NLTS is a filtered, real-valued, random multi-level sequence. In a second step, the NLTS is used to estimate either the nonlinear OWC system determined by its Volterra series  $V\{\cdot\}$  or the Volterra series  $U\{\cdot\}$  associated with the NLPE. Corresponding to an approximate inverse of the nonlinear OWC system, the individual operators  $U_q\{\cdot\}$  operate on the received samples  $y[k]$  and yield an approximation  $\hat{x}[k]$  of the transmitted samples as

$$\begin{aligned}\hat{x}[k] &= U\{y[k]\} \\ &= u_0 + \sum_{q=1}^Q U_q\{y[k]\}.\end{aligned}\quad (3.19)$$

The kernel coefficient estimate  $\hat{\mathbf{v}}$  corresponding to the nonlinear OWC itself is obtained when Eq. (3.18) is applied to the training sequence only. Similarly, but with the received NLTS as an input and the undistorted NLTS as an output, the kernel coefficient estimate  $\hat{\mathbf{u}}$  is obtained for the NLPE. The third and fourth steps in Fig. 3.1 indicate the application of  $V\{\cdot\}$  and  $U\{\cdot\}$  to the remaining signal for emulation of the nonlinear system or nonlinear equalization, respectively.



It is reasonable to expect that a compensation of nonlinearities only results fruitful, when a system is driven in a nonlinear regime and the resulting invertible nonlinear effects are the major limiting factor. For a thorough evaluation of the suggested NLPE, it is thus important to test it for varying a excitation of nonlinear effects and varying noise powers. In the following experimental validations, the amount of nonlinear distortions is adjusted via the Tx-side electrical signal powers  $\tilde{P}_{e,t}$ , which is varied digitally in steps of 3.01 dB over a range of approximately 30 dB (15 dB in optical signal power). In the following,  $\tilde{P}_{e,t}$  is given relative to the weakest power level used in the experiment and thus referred to as *normalized* electrical signal power. The Rx signal power and thus relative noise power is determined by the transmission distance, which is varied from 0.5 m to 3 m in steps of 0.1 m. The photograph on the side shows the laboratory setup of an aligned Tx/Rx pair at a distance of 3 m.

### 3.2.1 Results for SC-QAM

Table 3.1:  
SC-QAM DSP

PS	RRC
$\beta$	0.25
$R_{sy}$	23.4 MBd
$\mathcal{M}$	4, 16, 64, 256
$f_c$	20 MHz
$R_s$	125 MS/s
OH	3.92% w/ NLTS 0.36% w/o NLTS
$G_{phy,g}$	93.75, 140.63, 187.5 Mb/s

In the first evaluation of the nonlinear OWC system, the transmission of an  $\mathcal{M}$ -ary QAM SC is considered. Since the spectral distribution of the Rx noise is not white due to an analog equalization circuit in the Rx front ends (see Fig. 3.2 and Appendix A.1), the 23.4 MBd SC is positioned at a center frequency  $f_c = 20$  MHz, where noise and distortions were found to be minimal. For the nonlinear estimation, the NLTS is a random real-valued five-level sequence, filtered by a passband filter with equal center frequency  $f_c$  and bandwidth as the payload signal. Five levels are used to guarantee the estimation of a fourth-order polynomial is sufficiently determined. The filtering serves in the creation of a training signal, which spans the same subspace in frequency domain as the payload data. This real-valued sequence thus has the same spectral components as the payload. The 131200 samples of the NLTS at a sample rate of  $R_s = 125$  MS/s occupy a total of 3.56% of one frame. Additional relevant DSP parameters are given in Table 3.1.

Using the NLTS for the estimation of the overall nonlinear system  $V\{\cdot\}$ , it is possible to emulate the nonlinear distortions only by computing

$$\begin{aligned}
 d_{nl}[k] &= \sum_{q=2}^Q d_q[k] \\
 &= \sum_{q=2}^Q \mathbf{x}_q[k]^T \hat{\mathbf{v}}_q.
 \end{aligned} \tag{3.20}$$

A comparison of  $d_{nl}$  and the measured Rx noise level allows an illustration of the circumstances under which a nonlinear compensation may improve the overall system performance. In the following,  $d_{nl}$  is emulated using estimated kernel coefficients  $\hat{\mathbf{v}}$  with  $Q = 3$ ,  $m_1 = 51$ ,  $m_2 = 9$ ,  $m_3 = 7$  and  $\lambda = 0.2$  for an aligned Tx/Rx pair at a distance of 1.4 m. The limitation to third order and the given memory lengths results from the fact that an increase did not further reduce the estimation error. Similarly, the regularization parameter was chosen to yield the smallest estimation error.

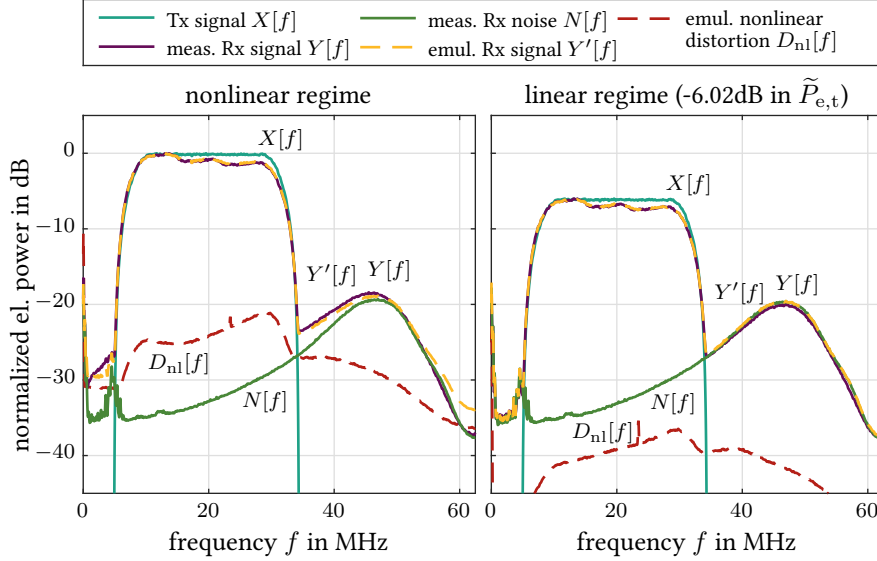


Figure 3.2: Example spectra showing the noise and distortion components.  $X[f]$  is the undistorted 23.4 MBd transmit signal at an intermediate frequency of 20 MHz.  $Y[f]$  and  $N[f]$  are the *measured* signal and noise floor at the receiver, respectively.  $Y'[f]$  and  $D_{nl}[f]$  are the *emulated* signal and nonlinear distortions at the receiver, respectively.

The spectra<sup>3</sup> of the payload of the input signal  $x[k]$ , measured received signal  $y[k]$ , measured noise  $n[k]$ , emulated received signal  $y'[k]$ <sup>4</sup>, and the emulated nonlinear distortions  $d_{nl}[k]$  are shown in Fig. 3.2 and denoted with their capitalized equivalents. The left and right graphs differ in that the normalized electrical transmit signal power  $\tilde{P}_{e,t}$  is 18.06 dB for the left graphs and 12.04 dB for the right graphs. Thus, the right graphs correspond to a mostly linear excitation of the Tx components. We may first observe that in both cases, the emulated Rx spectrum  $Y'[f]$  and the measured Rx spectrum  $Y[f]$  show a good fit. For a nonlinear excitation, the in-band nonlinear distortions shown by  $D_{nl}[f]$  are stronger than the noise floor  $N[f]$  and therefore the limiting factor. When  $\tilde{P}_{e,t}$  is reduced by 6 dB, the nonlinear distortions are reduced by approximately 15 dB and the receive-side noise becomes the limiting factor. In the first case, nonlinear compensations schemes become of interest.

With the same NLTS, it is possible to also estimate the Volterra operator  $U\{\cdot\}$  of the NLPE. As shown in Eq. (3.19), the nonlinear equalizer operates on the received signal  $y$  and yields an approximate  $\hat{x}$  of the originally transmitted TS for linear equalization and payload. The remainder of this section is thus dedicated to showing the improvements obtained from the application of the NLPE on a SC-QAM signal. For the NLPE the same configuration of  $Q = 3$ ,  $m_1 = 51$ ,  $m_2 = 9$ ,  $m_3 = 7$ , and  $\lambda = 0.2$  yielded good performance

<sup>3</sup> All measured quantities are obtained from digitized values and for technical correctness, the frequency-dependence should be indicated by the discrete-frequency index  $l$  as e.g.  $X[l]$ . As the physical frequency  $f$  is commonly of more interest than its index, we will be using  $X[f]$  to indicate the correspondence to a physical frequency of the discrete-frequency quantity.

<sup>4</sup> The emulated Rx signal results from the sum of  $d[k] = \mathbf{x}[k]^T \hat{\mathbf{v}}$  and the measured noise floor.

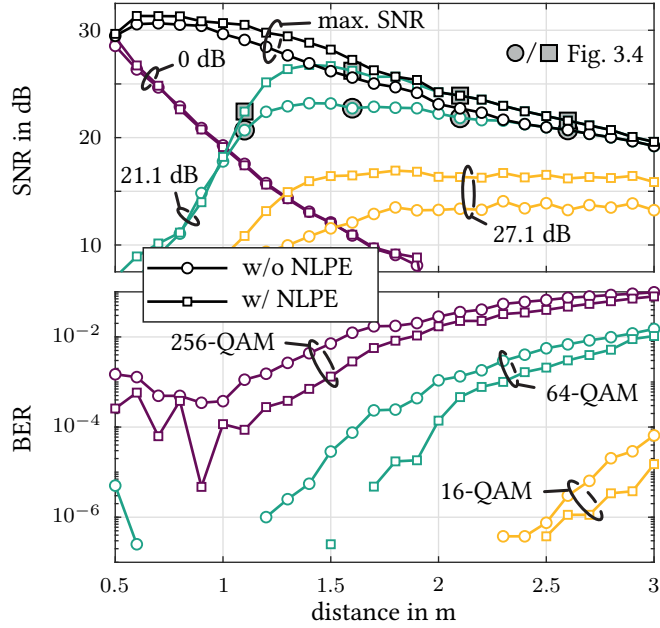


Figure 3.3: Measured SNR (upper graphs) from the 23.4 MBd 64-QAM transmission for multiple drive signal magnitudes, distances and either linear or nonlinear post-equalization. The points highlighted with a gray background correspond to the constellations shown in Fig. 3.4. Obtained BERs (lower graphs) for 16-, 64- and 256-QAM for linear and nonlinear post-equalization.

improvements. The results for a 4-, 16-, 64- and 256-QAM payload are summarized in Fig. 3.3.

The upper graphs show the SNR obtained from the error-vector magnitude (EVM) of the 64-QAM transmission experiment. We first discuss the colored lines, which correspond to selected normalized  $\tilde{P}_{e,t}$  of 0, 21.1 and 27.1 dB. At a low  $\tilde{P}_{e,t}$  of 0 dB, the system behaves linearly and the use of the NLPE yields no gain in SNR. An increased electrical power of 21.2 dB leads to a saturation of the Rx circuitry at distances below approximately 1.4 m, but yields large SNR improvements at larger distances. These are further improved by the NLPE, which reveals additional performance gains of up to 3.5 dB. An additional increase of  $\tilde{P}_{e,t}$  to 27.1 dB, limits the maximal performance due to Tx nonlinearities. While the NLPE continues to prove helpful, a smaller electrical transmit power  $\tilde{P}_{e,t}$  results in better SNR. Thus, for a fair comparison of the nonlinear and purely linear compensation scheme, the black lines in Fig. 3.3 show the SNR for the optimal  $\tilde{P}_{e,t}$  at each transmission distance with and without the use of the NLPE. The actual gain of the NLPE is then limited to approximately 2 dB.

For these optimal  $\tilde{P}_{e,t}$ , the resulting uncoded bit error rate (BER) is shown for a 16-, 64-, and 256-QAM in the lower graphs of Fig. 3.3. While a 4-QAM<sup>5</sup> was also used in this transmission experiment, the resulting uncoded BER was zero for nonlinear and linear equalization at all distances and is thus not displayed. This shows that a nonlinear compensation is mostly interesting for

<sup>5</sup> Also known as quadrature phase-shift keying (QPSK).

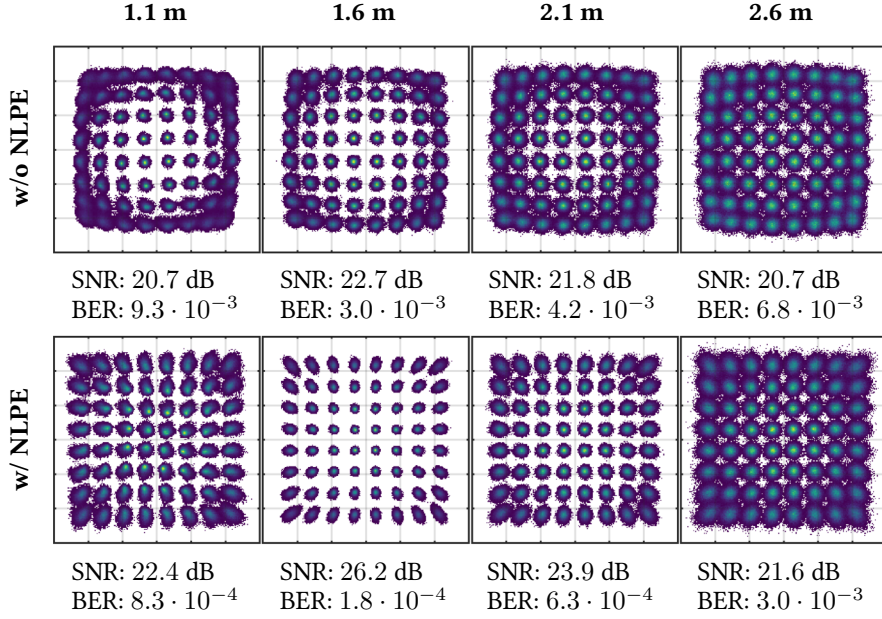


Figure 3.4: Evolution of 64-QAM constellation along the transmission distance with and without activated nonlinear equalization.

modulation formats of higher cardinality. Interestingly, the gain of the NLPE diminishes at larger distances, where the Rx noise becomes the dominant limitation and strong nonlinearities cannot be fully compensated anymore.

Fig. 3.4 shows an evolution of received 64-QAM constellations at selected points along the transmission distance for the intermediate power level of 21.1 dB. Their correspondence to the SNR reported in the upper graph of Fig. 3.3 is indicated with filled circles (w/o NLPE) and filled squares (w/ NLPE). In particular the constellations for which no NLPE is applied reveal the different types of nonlinearities the communication system needs to cope with. The slightly saturating behavior of the LED is induced at the Tx and thus visible at all transmission distances. This distortion is compensated fairly well and yields a gain of 3.5 dB in SNR and a reduction by more than an order of magnitude in BER at a distance of 1.6 m. While the NLPE continues to correct the nonlinearly distorted constellations at higher transmission distances, it becomes visible that its gains are reduced due to an increased additive noise component. At the shorter distance of 1.1 m, we may observe an amplitude-dependent phase rotation due to the saturated Rx circuitry. While the application of the NLPE still improves the overall performance – it increases the SNR by 1.7 dB and reduces the BER by an order of magnitude – the inner constellation points of the 64-QAM are distorted by the equalizer.

It is noteworthy, that the analog-to-digital converter (ADC) was not saturated throughout the experiments discussed in this chapter and we may thus infer, that the nonlinear distortions introduced at the Rx are due to ADC clipping. Furthermore, for a fixed short transmission distance of, e.g. 0.5 m and thus constant average optical power  $\bar{P}_t$ , a reduction of the electrical signal power  $\tilde{P}_{e,t}$ , significantly improves the performance. We may therefore assume, that said distortions are not a result of a saturated photodiode (PD),

but, e.g., the trans-impedance amplifier (TIA) between the PD and the ADC. In such a case, an automatic gain control (AGC) after the PD may avoid the saturation of the remaining Rx circuitry. Such a modification could improve the system's performance for large electrical signal powers  $\tilde{P}_{e,t}$  at short distances and make a slow Tx power adaptation obsolete. At the time of all experiments in this thesis, such an AGC was not available and the electrical transmit signal power was adjusted to suit the desired transmission distance range.

### 3.2.2 Results for DCO-OFDM

Table 3.2:  
OFDM DSP

$N_{\text{DFT}}$	1024
$S$	20-490
$N_{\text{CP}}$	128
$R_s$	125 MS/s
OH	16.45% w/ NLTS 11.22% w/o NLTS
$\mathcal{M}$	2,4,16,32,64, 128,256,512, 1024,2048,4096
BPL	Krongold (tar. BER: $10^{-2}$ )
$G_{\text{phy,g}}$	up to 291 Mb/s

While the previous results showed the usefulness of the NLPE for SC-QAM waveforms with fixed data rates, this section focuses on its application to the DCO-OFDM waveform popular for OWC. Together with a bit and power loading (BPL) algorithm [105], this waveform allows to efficiently make use of the 50 MHz bandwidth and frequency-dependent SNR of the optical front-ends and to investigate the NLPE's impact on the link-level throughput. In the DCO-OFDM experiments discussed in the next paragraphs, the subcarriers range from 2.44 MHz to 59.81 MHz. The same five-level sequence as for the SC-QAM experiments is used as a NLTS, however, filtered to span a frequency range from 1.25 MHz to 61.25 MHz and thus cover the side-lobes of the OFDM waveform. Further DSP parameters are given in Table 3.2.

Similar to Fig. 3.2, the payload spectra of the Tx signal, measured Rx signal, measured noise, emulated Rx signal and emulated nonlinear distortions are shown in the upper graphs of Fig. 3.5 for two different normalized electrical transmit signal powers  $\tilde{P}_{e,t}$  of 18.06 dB and 12.04 dB. These correspond to a nonlinear and a mostly linear excitation, respectively. In both cases, the measured and emulated Rx signals show a good fit (compare purple/solid and yellow/dashed lines). In case of a nonlinear excitation, we observe that the ratio between the emulated nonlinear distortions  $D_{\text{nl}}[f]$  and the Rx noise  $N[f]$  depends on the frequency. For subcarriers below 33 MHz, the interference due to nonlinear distortions appears to be stronger than the Rx noise. While in this range, an improvement due to the NLPE may be expected, this is the contrary for subcarriers at frequencies above 33 MHz. For a mostly linear excitation, the Rx noise is the major limiting factor and a nonlinear compensation scheme should not provide any benefits.

These expectations are verified by the graphs in the lower axes of Fig. 3.5. For both, the nonlinear and linear regime, the SNR per subcarrier is shown with and without an application of the NLPE. When the Rx is driven in the nonlinear regime, the NLPE allows for an SNR improvement of approximately 2.5 dB at lower frequencies. At frequencies above 33 MHz this improvement vanishes quickly. For a linearly driven Tx, we may observe that the NLPE offers no improvement. The average SNRs for the linear regime are thus identical and have the value of 15.3 dB. For the nonlinear regime, the SNRs are increased to 17.7 dB and 19.3 dB without and with the NLPE, respectively. Thus, driving the system in a nonlinear regime yields larger SNR at this distance.

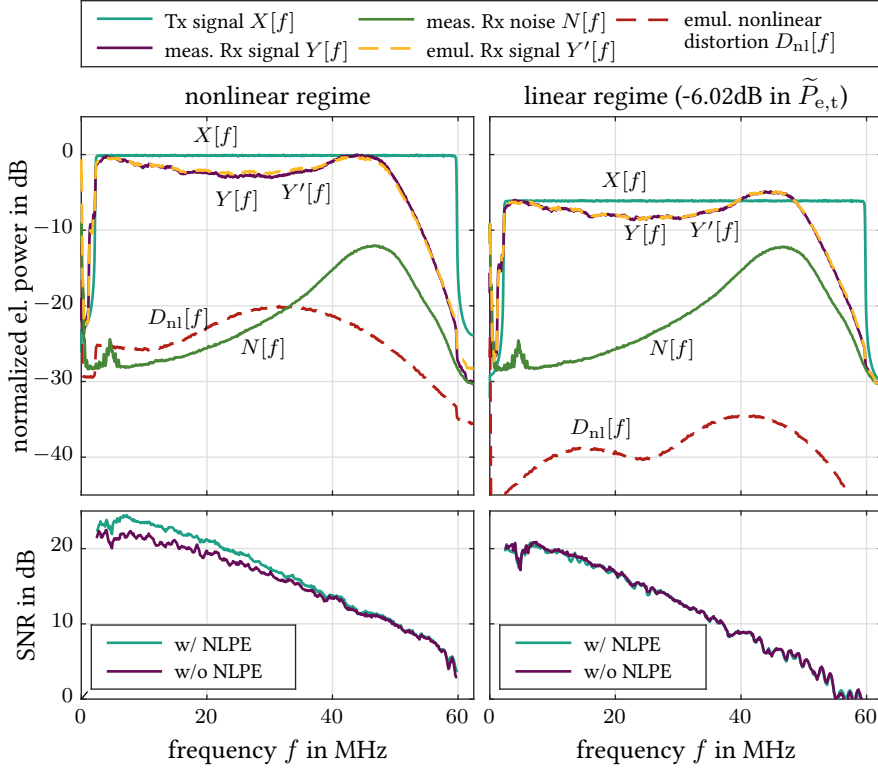


Figure 3.5: Results for an DCO-OFDM transmission over a distance of 1.9 m. The upper graphs show example spectra.  $X[f]$  is the undistorted transmit signal.  $Y[f]$  and  $N[f]$  are the *measured* signal and noise floor at the receiver, respectively.  $Y'[f]$  and  $D_{nl}[f]$  are the *emulated* signal and nonlinear distortions at the receiver, respectively. The lower graphs show resulting SNRs per subcarrier with/without the application of the NLPE.

In order to translate this improved signal quality into a potential gain of data rates, we may use a BPL algorithm such as [105]. For a fixed overall electrical signal power and a target uncoded BER, a suitable power and modulation format of suitable spectral efficiency is assigned to each subcarrier. The result of this loading algorithm is then used to estimate the gross physical layer throughput  $G_{\text{phy,g}}$ . Here, a target uncoded BER of  $10^{-2}$  was chosen<sup>6</sup>. For this configuration, the resulting gross physical layer throughputs  $G_{\text{phy,g}}$  are 180 Mb/s in the linear regime with and without the NLPE. In the nonlinear regime, a purely linear equalization yields a rate of 232 Mb/s and the use of the NLPE yields 249 Mb/s. Thus, the use of a 6.02 dB larger  $\tilde{P}_{e,t}$  improves the rate by 28.8% and which the NLPE increases to a total of 38.3%.

The estimation of an average SNR and gross physical layer throughput  $G_{\text{phy,g}}$  was performed at all distances and electrical transmit signal powers  $\tilde{P}_{e,t}$ . A summary of the results is provided in Fig. 3.6. The upper and lower graphs represent the average SNR and throughput at each distance, respectively. The colored lines correspond to selected normalized electrical transmit powers of 0, 21.1 and 27.1 dB. As in the SC-QAM transmission experiment,

<sup>6</sup> This target BER of  $10^{-2}$  lies well below the limit BER of  $2 \cdot 10^{-2}$  required for a block error rate (BLER) of  $10^{-3}$  when using an LDPC FEC of rate  $R_{\text{FEC}} = 5/6$  [127].

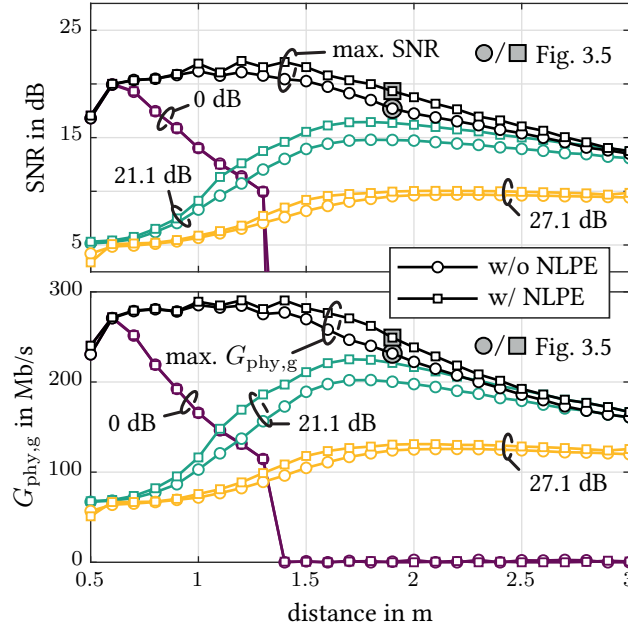


Figure 3.6: Results from the DCO-OFDM transmission for optimal (black lines) and a selection (colored lines) of normalized electrical transmit powers  $\tilde{P}_{e,t}$  with (square markers) and without (circular markers) nonlinear equalization. Upper graphs show the average SNR. Lower graphs represent the estimated gross throughput  $G_{\text{phy,g}}$ . The points highlighted with a gray background correspond to the results shown in Fig. 3.5.

the NLPE yields no gain at the lowest  $\tilde{P}_{e,t}$  of 0 dB. In this case, the signal could not be recovered for distances above 1.3 m. For an increased transmit power of 21.1 dB, the NLPE's maximal gains of 1.9 dB in SNR or 32 Mb/s in  $G_{\text{phy,g}}$  are obtained at a distance of 1.2 m. These reduce to 1 dB and 13 Mb/s at a distance of 1.5 m when  $\tilde{P}_{e,t}$  is increased to 27.1 dB. When all  $\tilde{P}_{e,t}$  in range from 0 dB to 30 dB are considered, best results in SNR and throughput are obtained at varying  $\tilde{P}_{e,t}$ . These maximum values are indicated by the black lines in Fig. 3.6. The overall maximally achieved gross throughputs are 285 Mb/s and 291 Mb/s, without and with the use of the NLPE. Largest gains are obtained at intermediate distances between 1.4 m and 2.2 m, where slightly larger  $\tilde{P}_{e,t}$  introduce distortions, that lie above the noise floor and can be compensated by the NLPE. For these best cases, the NLPE gain in SNR and throughput is 1.6 dB and 24 Mb/s.

The reduced gains in the DCO-OFDM transmission experiment may be attributed to the fact, that the signal spectrum covers the entire bandwidth of 50 MHz, including the portion of the spectrum where the noise floor is significantly larger than the estimated nonlinear distortions. In the previous example illustrated in the left graphs of Fig. 3.5, this is the case for frequencies above 33 MHz. As a result, the small gains in SNR at higher frequencies and the large gains at lower frequencies average out to a reduced gain of 19.3 dB-17.7 dB = 1.6 dB. This example, obtained at 1.9 m, is highlighted in Fig. 3.6 by filled squares (w/ NLPE) and filled circles (w/o NLPE).

Similar as for the SC-QAM waveform, the adjustment of Tx power helps increasing the operational distances. Over the entire range of 0.5 m to 3.0 m this allowed for rates above 150 Mb/s with and without the NLPE and a peak rate of 291 Mb/s with nonlinear equalization.

### 3.3 CONCLUSION

In this chapter, an option of modeling the nonlinear distortions in an OWC system with a Volterra series has been discussed. This model has then been shown to be useful in a laboratory setup not only for the emulation of such nonlinear system, but also for the mitigation of its nonlinear distortions using a receiver-side, data-aided nonlinear post-equalizer. This NLPE has then been shown to be applicable to two waveforms popular in OWC, namely SC-QAM and DCO-OFDM.

We observed that large electrical signal powers are required at the Tx to cover large transmission distances. While the resulting nonlinear distortions at the Tx are well compensated, the saturation of the Rx circuitry between the PD and ADC is more difficult to combat. Here, an AGC would be required, which was not available at the time of the experimental validation. Thus, in the experiments presented in the following two chapters, the power level was adjusted to avoid saturation at distances below 0.8 m.

Although gains of up to 2 dB in SNR were achieved, the NLPE was not implemented in real-time and is not part of the transmission experiments in Chapter 5.



## MEASUREMENT OF THE OPTICAL WIRELESS MIMO CHANNEL

---

The channel impulse responses (CIRs) provided in [95], [96] and discussed in Section 2.2.2 are an important milestone for understanding the optical wireless communication (OWC) channel in industrial production environments. While the geometry of the simulation environment was obtained from a laser scan of a real manufacturing cell, the CIRs were derived from offline raytracing. Nevertheless, these results lack a spatially resolved analysis of the OWC channel and were not experimentally verified. This gap is filled by the content of this chapter, which provides OWC channel measurements in an industrial production environment first published in [128]. The insights obtained from these measurements are poured into the design of a reliable multiple-input multiple-output (MIMO) communication system, whose iterations are presented in Chapter 5. In this chapter, however, we start with an introduction of the measurement setup, which is followed by the presentation and discussion of the channel measurements.

### 4.1 MEASUREMENT SETUP

In order to characterize the MIMO optical wireless channel, we use a channel sounder capable of performing broadband  $8 \times 8$  channel measurements at frequencies of up to 250 MHz. This section is devoted to describing the hardware and the approach taken to perform broadband measurements at high sensitivity.

#### 4.1.1 Hardware

The transmitter hardware consists of eight commercially available, synchronized digital-to-analog converters (DACs) (Spectrum DN 2.662-08) running at a sampling rate of up to 625 MS/s and eight proprietary broadband optical front ends using red light-emitting diodes (LEDs) [66]. Lenses of different fields-of-view (FOVs) may be attached to the optical front ends. However, during the experiments no lenses were attached in order to achieve better coverage. The receiver hardware consists of eight commercially available, synchronized analog-to-digital converters (ADCs) (Spectrum DN 2.445-08) with sampling rates of up to 500 MS/s and highly sensitive, broadband front ends with concentrators glued onto the receiver (Rx) photodiodes (PDs) [68]. As shown in Fig. 2.4, the transmitter (Tx) and Rx used in this experiment exhibit a wide beam and large FOV, respectively. Out of up to eight Tx, only six were used and mounted on the faces of a cube, resulting in an omnidirectional light source. The Tx are operated in a small-signal mode, where the electrical signal power  $\tilde{P}_{e,t}$  was kept small to avoid nonlinear distortions and measurements at high frequencies are possible. A drawback of the

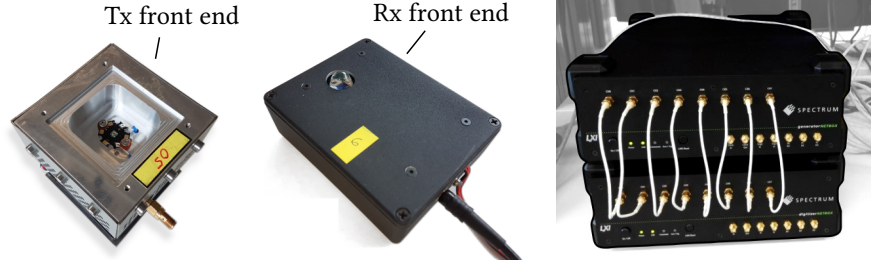
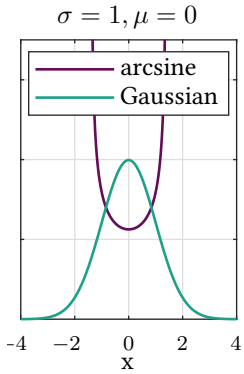


Figure 4.1: Key hardware components of channel sounder. From left to right: optical Tx front end, optical Rx front end and 8-channel DACs/ADCs.

reduced modulation index  $\mu$  is the reduced transmit signal power, which translates to reduced receive powers. In order to perform broadband channel measurements with high coverage, we characterize the channel with single frequencies. The concept is explained in the following subsection.

#### 4.1.2 Frequency-sweep



probability density functions (pdfs) of an arcsine and Gaussian distribution of a the random variable  $x$ , displayed for equal mean  $\mu$  and variance  $\sigma^2$ .

Instead of a simultaneous transmission of all pilot tones, each Tx generates a total of  $N_s$  individual sinusoids, which are transmitted consecutively<sup>1</sup>. In the following, we use the index  $i$  to enumerate the  $N_s$  sinusoids per Tx. The use of individual sinusoids concentrates the signal energy within a given time slot into a single frequency. Furthermore, the sinusoidal amplitude distribution given by the arcsine distribution has a lower peak-to-average power ratio (PAPR) than the one of waveforms consisting of multiple sinusoids, for which it is known to approach a Gaussian distribution. Facing constraints of electrical peak power, rather than average power, the reduced PAPR is used to increase the average modulation index  $\mu$  and hereby the sensitivity and coverage of the channel sounder.

For the generation of the  $i$ -th sinusoid of the  $n$ -th Tx with frequency  $f_{n,i}$ , a block  $X_{n,i}$  of  $N_{\text{DFT}}$  samples is fed to an inverse discrete Fourier transform (iDFT):

$$x_{n,i}[k] = \frac{1}{N_{\text{DFT}}} \sum_{l=1}^{N_{\text{DFT}}} X_{n,i}[l] e^{\frac{2\pi j}{N_{\text{DFT}}}(l-1)(k-1)} \quad (4.1)$$

$X_{n,i}$  is zero, except at the support points corresponding to the desired frequency and its negative counterpart:

$$X_{n,i}[l] = \begin{cases} 1, & l = \lfloor f_{n,i} \cdot N_{\text{DFT}}/R_s \rfloor + 1 \\ 1, & l = \lfloor f_{n,i} \cdot N_{\text{DFT}}/R_s \rfloor + 1 + N_{\text{DFT}} \\ 0, & \text{otherwise} \end{cases} \quad (4.2)$$

This approach generates blocks of periodic sinusoids with a sample rate of  $R_s$ . Prior to transmission a cyclic prefix (CP) of length  $N_{\text{CP}}$  is added to each block. The inset of Fig. 4.2a illustrates how the  $i$ -th frequencies of

<sup>1</sup> The expression *individual sinusoids* is used to emphasize the fact that the resulting time-domain waveform is a sinusoid, as opposed to a nearly random waveform with almost Gaussian distribution resulting from the superposition of multiple sinusoids.

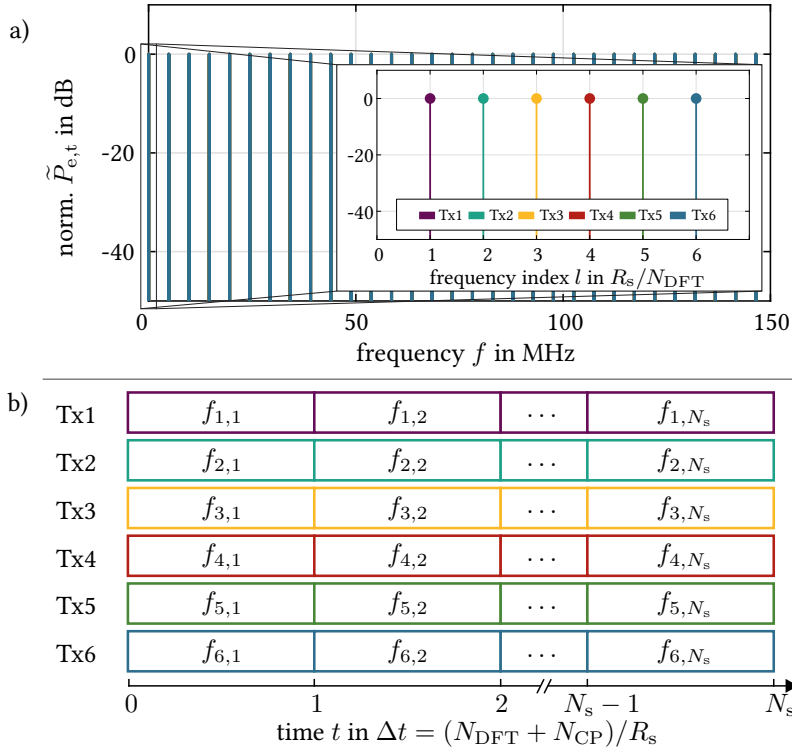


Figure 4.2: Distribution of sinusoidal pilots over all transmitting LEDs and time-slots. a) With  $N_s=31$ , the frequencies per Tx result in a spacing of 4.89 MHz, starting from the lowest non-zero frequencies up to frequencies around 146.7 MHz. The pilots of the six Tx were positioned at neighboring iDFT support points (see inset) to force their orthogonality. b) While the orthogonal pilots of all Tx were transmitted simultaneously, the multiple frequencies at which the channels were measured, were transmitted consecutively allowing for an increased measurement sensitivity.

the six transmitters are positioned on the neighboring iDFT support points following  $f_{1,i} < f_{2,i} < f_{3,i} < f_{4,i} < f_{5,i} < f_{6,i}$ . Hereby, the used pilot tones are orthogonal, which allows simultaneous channel sounding of all Tx. The positions of all frequencies  $f_{n,i}$  in time are depicted more clearly in Fig. 4.2b. Note that except for an added direct-current (DC) component this approach is very similar to channel estimation methods using sparse scattered pilots commonly used for orthogonal frequency-division multiplexing (OFDM). This channel sounding allows us to employ algorithms for channel estimation and interpolation commonly used in OFDM, see [104] and references therein.

Prior to a presentation of measured channel responses, the measurement environment is introduced in the following subsection.

#### 4.1.3 Manufacturing Cell

The manufacturing cell that served as an exemplary industrial environment is part of BMWs robot testing facility, in which new robots are put under stress and endurance is tested prior to the use in the actual production cells. It is administrated by the same department at BMW, whose cell served as

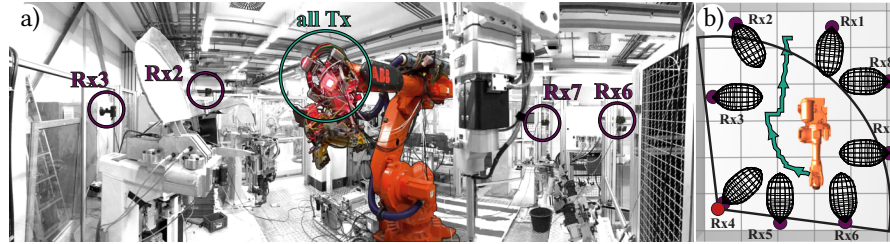


Figure 4.3: a) Picture of the manufacturing cell in which the experiments were conducted. Red LEDs were mounted at the end of the robot arm (green circle) next to a grapppler tool used to pick up car parts. Visible Rx's are highlighted with smaller, purple circles. b) CAD's model of the manufacturing robot including the position from which the photograph was taken (red circle) and the approximate field of view of the camera. The trace along which the Tx was moved is highlighted by the arrowed green line. Purple circles show the Rx's positions.

the industrial manufacturing environment in [95], [96] and Section 2.2.2. At the time of this measurement, however, the former cell was disassembled and unfortunately making the attempt to measure the simulated channels from [95], [96] impossible. This smaller cell extends over a 5 m by 5.7 m rectangular area with a single robot within and is surrounded by a metal cage, partially covered with acrylic glass. In our setup, the omnidirectional Tx was attached to the end of the robot arm, at which the tools for a production step are usually mounted to. This position was chosen, since it was expected that not all tools require data transmission and the communication units would be part of the tools and not the robot itself. A photograph of the cell is shown in Fig. 4.3a, in which the Tx and some Rx's are highlighted with green and purple circles, respectively. As depicted in the computer aided design (CAD) model in Fig. 4.3b, eight Rx's were located at attachable positions around the robot, such that roughly all parts of the cell were visible by some Rx's. No pre-measurements were performed to identify the ideal placement. The green line is the trajectory along which multiple channel measurements were performed and was defined by the BMW staff independently of the Rx placement. It represents a typical movement in a production step, consisting of picking up a part, moving it to the soldering station and dropping off the part on the opposite side of the cell.

The channel measurements discussed in the following paragraphs were performed at a sampling rate  $R_s$  of 500 MS/s, an iDFT size  $N_{\text{DFT}}$  of  $2^{18}$  and an  $N_{\text{CP}}$  of 128. As depicted in Fig. 4.2a, for a given Tx  $n$  the frequencies  $f_{n,1}$  to  $f_{n,N_s}$  were chosen at a spacing of approximately 4.89 MHz allowing to capture memory effects due to reflections of up to  $\frac{1}{4.89 \text{ MHz}} = 204.5 \text{ ns}$ , which lie well within the CP with a temporal length of  $N_{\text{CP}} \cdot R_s = 256 \text{ ns}$ . Such memory effects would correspond to reflections, which travel an additional distance of 61.3 m in air. With this set of parameters, we may thus expect to capture all significant reflections within the given manufacturing cell. The pilot frequencies range from the lowest nonzero frequencies possible up the frequencies located at around 146 MHz. The  $8 \times 6$  MIMO channel was measured at 74 positions along the 5 m long typical trajectory displayed in Fig. 4.3b, resulting in 3552 individual spatial channels. The average distance

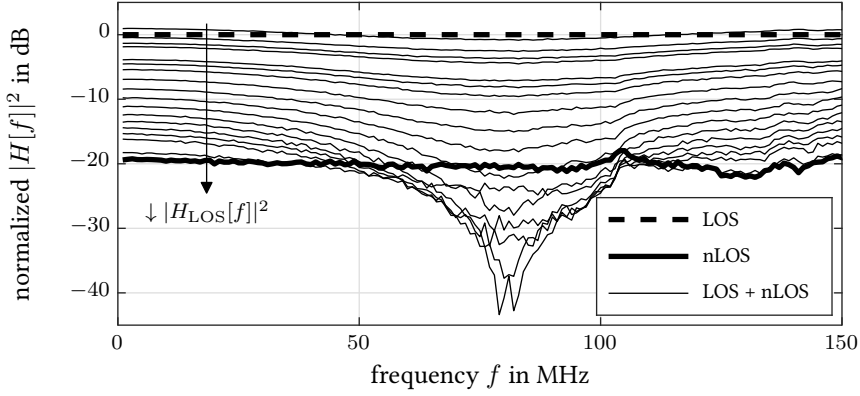


Figure 4.4: Measured impact of a reflected signal in a two-wave channel due to specular reflection. The LOS and nLOS channels are illustrated by a thick dashed and a thick solid line, respectively. The thin solid lines show the channel, when both components superimpose on the Rx PD for different strengths of the LOS component.

between two positions was 6.9 cm with a standard deviation of 2.8 cm. The largest gap between two points was 16 cm between the first and second position. At 3.1 m along the trajectory the tip of the robot was only rotated, resulting in the smallest translational movement of 0 cm.

## 4.2 MEASUREMENT RESULTS

### 4.2.1 Frequency Selectivity

In the preparations of this measurement campaign it was expected to see significant reflective components due to specular reflections off the acrylic glass surrounding the cell. Even single reflections resulting in a two-wave channel would be expected to significantly alter the frequency response of the measured channels [25], [128], [129]. Although it does not belong to the measurement series within the manufacturing cell, such a two-wave channel was generated in a controlled manner within a laboratory environment, to illustrate the expected impact. The two-wave interference, resulting from a specular reflection, was captured experimentally for a fixed path length difference  $\Delta d$  of 1.85 m and a variation of  $\alpha$  of approximately -20 to 0 dB, where  $\alpha$  denotes the relative optical signal power between the line-of-sight (LOS) component and the non-line-of-sight (nLOS) specular reflection. The magnitude of resulting overall frequency response  $H[f]$  with the destructive interference around

$$f_d = \frac{c}{2\Delta d} \approx 81 \text{ MHz} \quad (4.3)$$

is shown in Fig. 4.4. For  $|H_{\text{LOS}}[f]|^2|_{\text{dB}} - |H_{\text{nLOS}}[f]|^2|_{\text{dB}} > 10 \text{ dB}$ , the measurement indicates a overall channel variation below 5 dB. However, for  $|H_{\text{LOS}}[f]|^2 \rightarrow |H_{\text{nLOS}}[f]|^2$  and thus  $\alpha \rightarrow 0 \text{ dB}$ , we may observe that the otherwise large bandwidth of the optical wireless channel is severely reduced. As described in [128] and briefly summarized in Eq. (4.3), the bandwidth would be further reduced for larger path length differences  $\Delta d$ , which are

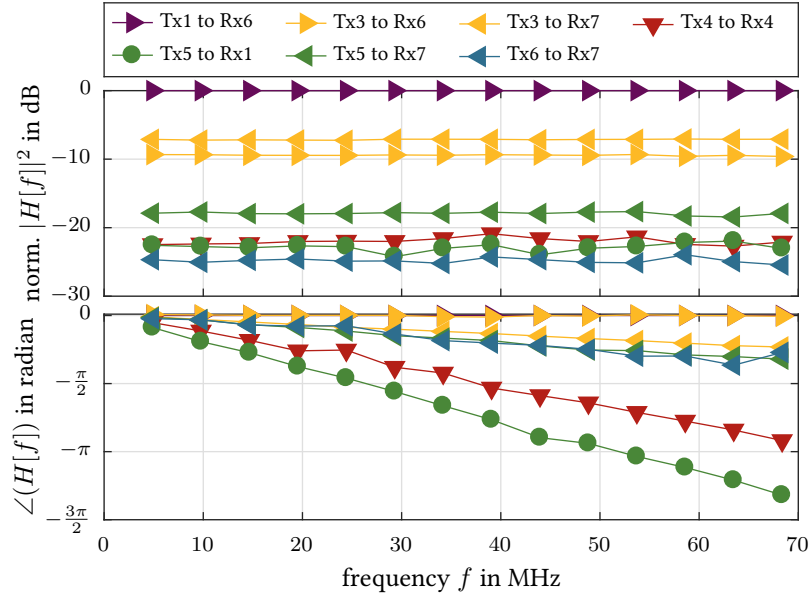
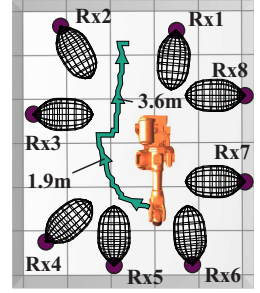
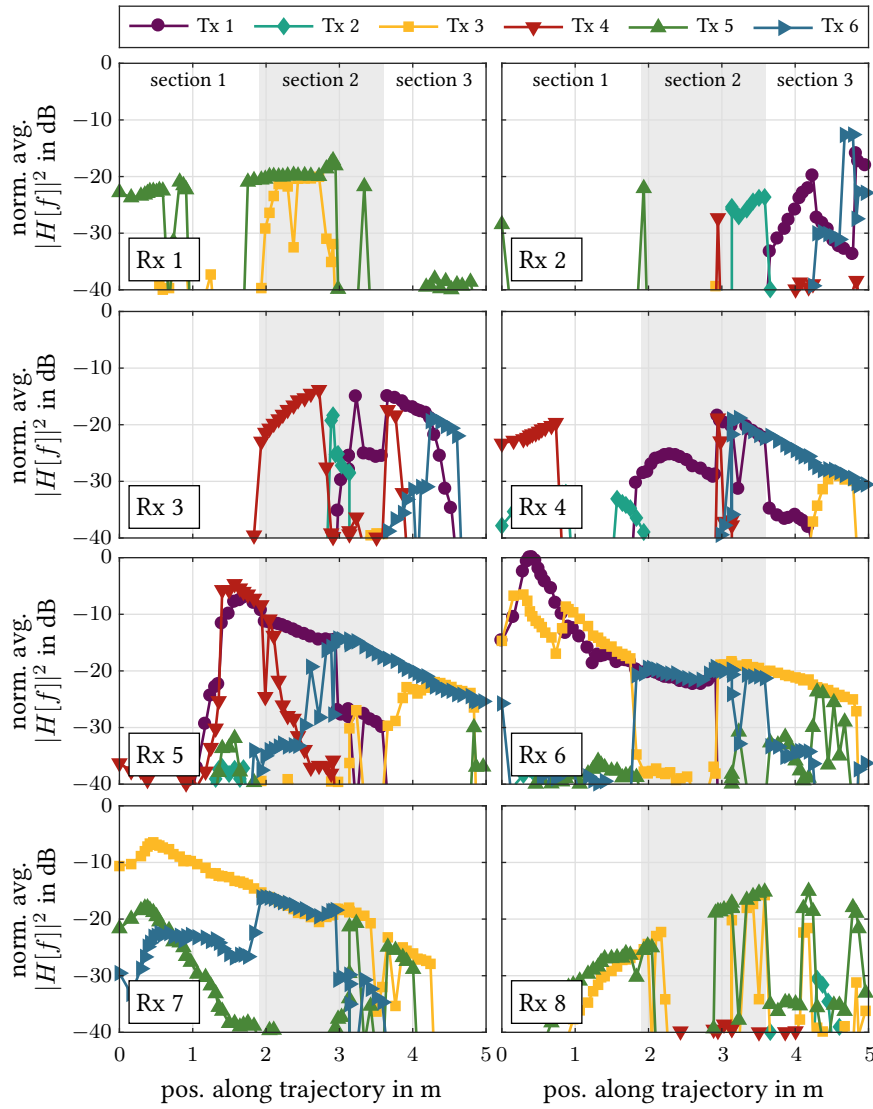


Figure 4.5: Exemplary optical wireless channels measured in the first section of the trajectory (position 0.4 m). Channels down to 30 dB below the strongest channel are shown and exhibit a flat frequency response.

likely obtained in larger room geometries. However, the case of two waves exhibiting similar powers after significantly different propagation distances, i.e.  $\alpha \approx 0$  dB and  $\Delta d \gg 0$ , is less likely. Furthermore, if this case manifests at larger propagation distances, the received optical signal power levels may easily fall below the Rx sensitivity [83].

In the channel measurement series within the manufacturing cell, it was observed that after deconvolution of the Tx and Rx circuitry channels with signal powers above the noise level were constant over frequency. Figure 4.5 shows an exemplary MIMO channel measured at 0.4 m along the trajectory. At frequencies above 70 MHz, we observed strong interference from radio broadcasting onto weak channels, which we expect to have coupled into the Rx signal path over the 5 m long coaxial cables between the distributed analog front ends and the ADCs<sup>2</sup>. Very low frequencies in the 0-100 kHz domain were strongly attenuated due to the alternating current (AC)-coupled Tx and Rx. The upper graph in Fig. 4.5 shows a total of 7 channels in the range of 5-70 MHz measurable above the noise level, which lies approximately 40 dB below the strongest channel. Unlike the two-wave-channels depicted in Fig. 4.4, all channels are flat over the entire range. This indicates that either path length differences between multiple waves were too short or that one component significantly dominated over all others. For this measurement series the results indicate a LOS dominated, distributed MIMO channel. The bottom graph of Fig. 4.5 shows the phases relative to the strongest channel. The linear frequency-dependence of the phase results from the delay differ-

<sup>2</sup> This can be mitigated with the use of differential signaling and twinaxial/twisted pair cabling. This insight was adopted and included in newer version of the front ends, which were used for data transmissions presented in Sections 3.2 and 5.4.



Trajectory and boundaries of sections 1/2 and sections 2/3 at 1.9 m and 3.6 m.

Figure 4.6: Measured average frequency responses along the trajectory represented by the colored lines. Shading of the background indicates three sections with different properties: in the first 1.9 m only a few strong channels exist, while in the next 1.7 m multiple weak channels are present. In the last 1.4 m of the trajectory even fewer and weaker channels are available.

ences between individual Tx/Rx pairs. Since the six Txs are in close spatial proximity (<30 cm) phases seen by the same Rx show similar slopes.

#### 4.2.2 Spatial Selectivity

Now we investigate the results with respect to the dependence of the MIMO channel on the position and movements of the robot and thus Tx placement. The average power transfer function in the range from 5-70 MHz serves as a figure of merit to determine the channel's spatial dependence. It is reported in Fig. 4.6 for all positions along the trajectory and all Tx/Rx pairs. At first glance, the measurement reveals that no single spatial channel maintains

large channel coefficients throughout the movement of the robot. When considering the multiplicity of 48 spatial channel at each position, we may roughly split the trajectory into three sections. While there are a few dominant channels seen within the first 1.9 meters by Rx6, Rx7 and the end of the section by Rx5, numerous similarly weak channels exist along the following 1.7 meters. In the last 1.4 meters, most channel gains are very low and fluctuate strongly.

Since the Tx's with large half-power semi-angle (HPSA) are closely spaced, we may observe an increasing path loss seen by Rx5, Rx6 and Rx7. As the omnidirectional Tx moves along the trajectory, it moves mostly away from these three Rx's (except for the first few centimeters). This overall slowly reducing channel gain is clearly visible along the trajectory. The use of Tx's with large HPSA further results in channels seen by a single Rx, yet originating from different Tx's, to have similar channel gains. Exceptions, e.g., as seen by Rx7 in section 1, are due to deeply counterbored LEDs in the highly reflective metal casings of the Tx front ends (see Fig. 4.1). This results in very small, yet non-zero side lobes in the angular dependence of the Tx's, similar to those in Fig. 2.4. As a result, weak channel coefficients manifest when a LOS exists between a Rx the LED's surroundings, but not to the LED itself.

While measurable channels do not exhibit any frequency selectivity, they face strong spatial selectivity. Even small rotations or movements of the robot's head result in sudden changes of the channel, leading to changes of the received signal by 10-20 dB in the electrical domain (e.g., channels Tx6  $\rightarrow$  Rx7 and Tx1/Tx3  $\rightarrow$  Rx6 at position 2.98 m). These measurement results indicate that even in a MIMO link, no assumptions on the existence of a minimum number of individual good LOS channels should be made, as regions exist in which illumination is poor and only multiple weak LOS signals are available for communication<sup>3</sup>. Even though a single trajectory does not represent the entire spectrum of possible channel realizations, it shows the variety of MIMO channels that must be coped with in this scenario.

### 4.3 CONCLUSION

In this chapter, the first MIMO channel measurements in an industrial production environment have been presented. The measurements, conducted in a 5 m by 5.7 m manufacturing cell at BMW, show the OWC channels exhibit a strong spatial selectivity as opposed to frequency selectivity, where small movements or rotations lead to sudden channel changes of 10-20 dB. Furthermore, multiple MIMO channel conditions are observed. While in some parts of the manufacturing cell the MIMO channel is dominated by a few strong spatial channels, it is spanned by multiple weaker channels in other parts. In poorly illuminated sections, the MIMO channel is composed a few spatial channels with very small gains.

The following chapter discusses how even such weak channels can be jointly used via antenna diversity to improve reliability even under bad illu-

<sup>3</sup> A simple counter-measure would be a prior illumination planning, which should alleviate the chances of poor illumination.

minations conditions and focuses on the transmission over MIMO channels employing antenna diversity in OWC.



Within the optical wireless communication (OWC) community, most experimental works so far have focused on exploiting the multiplicity of spatial channel for multiplexing gains. Such works report remarkable rates between one and seven Gb/s [21], [130], [131] in an up  $9 \times 9$  multiple-input multiple-output (MIMO) setup, however at limited distances below 2 m and employing highly directed transmission with small coverage. With an interest in a system with large coverage supporting mobile communication, the focus in this work lies on spatial diversity concepts known to potentially increase reliability [62], [132].

At the beginning of this chapter we introduce the basic idea of antenna diversity and illustrate its gains in a simple line-of-sight (LOS) MIMO simulation. Using the same high bandwidth equipment as in the previous chapter, we show how antenna diversity can be exploited in broad- and narrowband transmission systems. The resulting insights lead to the development of an analog combining circuitry and a new optical front end design suitable for spatially distributed transceivers (TRxs) with a limited bandwidth of 50 MHz. Together, these prototypes allow to make use of antenna diversity while using a commercial single-input single-output (SISO) digital signal processing (DSP) baseband unit. The reliable real-time transmission based on such a setup is presented and discussed afterwards. The same manufacturing cell as presented in Section 4.1.3 served as a demonstration environment for a first reliable and mobile real-time OWC transmission system.

## 5.1 ANTENNA DIVERSITY

This section introduces the use of antenna diversity as a concept for increasing the coverage and reliability of OWC. Equivalently to distributed antennas in radio frequency (RF) communication, we distribute multiple optical transmitter and receiver front ends in space, thus spanning a MIMO channel. Considering a link, in which a single information source transmits data to a single information sink, the transmit signal  $x$  is distributed to  $N$  transmitters (TxS) with the  $N \times 1$  transmit vector  $\mathbf{p}$  and is received by  $M$  receivers (RxS), resulting in an  $M \times N$  MIMO channel  $\mathbf{H}$ . The received signals and noise  $\mathbf{n}$  are combined using the  $M \times 1$  receive vector  $\mathbf{q}$  into a single signal

$$y = \underbrace{\mathbf{q}^T \mathbf{H} \mathbf{p}}_{H_{\text{eff}}} x + \mathbf{q}^T \mathbf{n}, \quad (5.1)$$

where  $(\cdot)^T$  denotes the matrix transpose. The application of the transmit and receive vectors to the channel matrix results in a scalar effective channel  $H_{\text{eff}}$ . Without loss of generality, we let  $\|\mathbf{p}\|_2^2 = \|\mathbf{q}\|_2^2 = 1$ , where  $\|\cdot\|_2$  denotes the Euclidean norm.

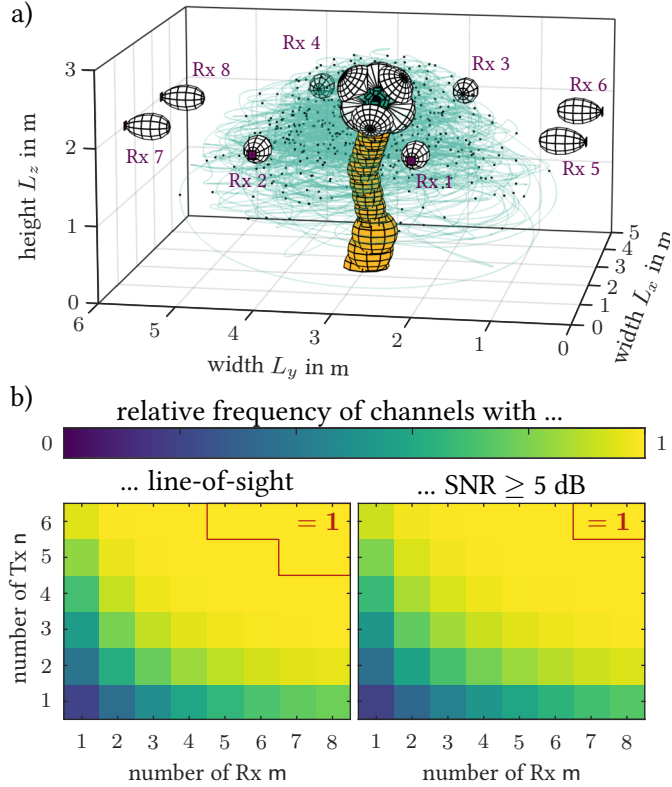


Figure 5.1: a) Rendering of the simulation setup in an uplink (UL) configuration, i.e. the TxS mounted on the robot model and the RxS on the walls. The green line interpolates the 500 randomly placed dots and indicates the trajectory taken by the TxS throughout the simulation resulting in  $10^6$  test positions. b) Availability of channels with LOS (left column) and sufficient SNR for a 23.4 MBd QPSK transmission (right column) for an UL transmission.

To show how antenna diversity significantly improves reliability, we use the LOS-MIMO simulator presented in Section 2.2.3 and analyze the existence of at least one available LOS for varying number of used Tx and Rx. The simulated room geometry is configured to emulate the behavior encountered in a real manufacturing cell. A rendering of the resulting geometrical setup is shown in Fig. 5.1a. It shows a downlink (DL) configuration, in which  $N = 6$  Tx and  $M = 8$  Rx are mounted at a robot's head and the surrounding walls, respectively. Purple dots indicate 500 randomly chosen points reachable by the robot model. Their interpolation yields  $10^6$  positions on a smooth trajectory represented by the green line. At each of these positions  $\mathbf{H}$  is computed. The LOS blocking term in Eq. (2.26) is determined by a set of spheres representing a fully opaque robot (orange spheres in Fig. 5.1a). When considering only a reduced number of Tx  $n \in \mathbb{N} : 1 \leq n \leq N$  and Rx  $m \in \mathbb{N} : 1 \leq m \leq M$ , we need to consider all combinations  $C_{NM}(n, m) = \binom{N}{n} \cdot \binom{M}{m}$  for each pair. For example, in the case of using all Tx/Rx, there is only one combination  $C_{68}(6, 8) = 1$ , but  $C_{68}(1, 1) = 48$  when one Tx/Rx is used at most. For simplicity, we set the entries of  $\mathbf{p}$  and  $\mathbf{q}$  to  $p_n = \frac{1}{\sqrt{n}}$  and  $q_m = \frac{1}{\sqrt{m}}$  in this first illustration and discuss improved choices in the

following sections. Analyzing if  $H_{\text{eff}} > 0$  at every position of the trajectory and for all combinations, results in the left heatmap of Fig. 5.1b, hereby revealing the relative frequency of existing LOSs for each combination of  $m$  and  $n$ . Increasing  $n$  and/or  $m$  rapidly increases the relative frequency of an existing LOS, saturating quickly to a value close to 1. However, due to the LOS blocking spheres, full coverage is only achieved when using at least a total of 11 optical front ends as indicated by the area surrounded by a red line. The right heatmap in Fig. 5.1b shows the relative frequency of channels with a signal-to-noise ratio (SNR)  $\geq 5$  dB<sup>1</sup>. These simulations are calibrated to match the measurement results presented in Section 3.2.1<sup>2</sup>. The shrunk area marked by the red line indicates that requiring a minimum SNR leads to an increased number of required TxS and RxS if full coverage is required.

An important observation for these exemplary simulations is how even a small number of Tx *and* Rx rapidly improves coverage and that antenna diversity appears to be a promising concept for improving the reliability of an OWC system. However, for an inherently reliable physical layer with full coverage, these simulations also indicate that there is no clear upper limit on the number of required front ends. This number depends on the LOS obstructing elements, the exact movements of a mobile unit (MU) and the targeted SNR, which cannot be determined by approximately accurate simulations. Therefore, the next sections cover experimental investigations of data transmission over an OWC system, which employs antenna diversity schemes. We start with the case of a broadband transmission (100 MHz).

## 5.2 BROADBAND TRANSMISSION

Even if the contributions from reflections have so far shown to be negligible, the joint use of multiple TxS and RxS effectively creates a multipath channel and the simple addition of all spatial channels, as done in the previous example, can result in self-induced multipath fading. Similar fading effects may also be observed in Digital Video Broadcasting - Terrestrial (DVB-T) [133], [134], when multiple-site transmission is used in a single frequency network (SFN). In OWC however, multi-path fading is only particularly severe for broadband transmissions. With a focus on broadband direct-current biased optical (DCO) orthogonal frequency-division multiplexing (OFDM) transmissions, the following section introduces means to mitigate this effect and shows their effectiveness in a short-reach  $8 \times 6$  MIMO transmission experiment performed within a reduced size manufacturing cell replica.

### 5.2.1 Phase-Matched Equal-Gain-Transmission

Notice that in a multi-carrier system such as DCO-OFDM, Eq. (5.1) describes the link per subcarrier with frequency-dependent  $\mathbf{H}$ ,  $\mathbf{p}$  and  $\mathbf{q}$ . With the

<sup>1</sup> This was the required SNR in [128] for an error-free QPSK transmission protected by an LDPC FEC code.

<sup>2</sup> An SNR of 20 dB is assumed between an aligned pair of Tx/Rx at 3 m distance. Equations (2.13) and (2.14) describe the angle dependence of the LEDs and PDs used.

entries of  $\mathbf{H}$ ,  $\mathbf{p}$  and  $\mathbf{q}$  being denoted by  $H_{mn}$ ,  $p_n$  and  $q_m$ , respectively, they are ideally chosen to maximize the scalar effective channel

$$|H_{\text{eff}}|^2 = \left| \sum_{m=1}^M \sum_{n=1}^N q_m H_{mn} p_n \right|^2 = \left| \sum_{n=1}^N \sum_{m=1}^M p_n H_{mn} q_m \right|^2, \quad (5.2)$$

where  $|\cdot|$  denotes the absolute value of a complex number. The maximization of the channel gain and SNR, which is achieved by maximum ratio transmission (MRT) and maximum ratio combining (MRC) at the Tx and Rx, respectively [135]. If the entries of  $\mathbf{p}$  and  $\mathbf{q}$  are constrained to have equal gains, i.e., to be of shape  $p_n = \frac{e^{i\rho_n}}{\sqrt{N}}$  and  $q_m = \frac{e^{i\psi_m}}{\sqrt{M}}$  with phase angles  $\rho_n, \psi_m \in [0, 2\pi)$ , we realize equal gain transmission (EGT) and equal gain combining (EGC), respectively. In case of EGT, the intensities of all LEDs are modulated with equal electrical signal power, which is particularly interesting for OWC since, due to peak-power constraints in the light-emitting diode (LED) driver and the LED itself, power transfer among different Tx's would lead to strong clipping. In case of EGT with either EGC or MRC, the joint optimization of  $\mathbf{p}$  and  $\mathbf{q}$  is not straightforward as we face a nonlinear cost function with multiple local and global optima. A brute-force search may be applied for small MIMO systems [135], but in the case of  $N = 6$  and  $M = 8$  this involves a search over a 14 (EGC) or 22 (MRC) dimensional space, which becomes unfeasible due to the *curse of dimensionality*. However, independent optimization of  $\mathbf{p}$  and  $\mathbf{q}$  is possible. For a given channel  $\mathbf{H}$  and receive vector  $\mathbf{q}$ , the optimal transmit phase vector  $\boldsymbol{\rho}^*$ , where optimality is denoted by  $(\cdot)^*$ , is determined by the optimization problem

$$\boldsymbol{\rho}^* \in \underset{\boldsymbol{\rho} \in [0, 2\pi)}{\text{argmax}} \left| \sum_{n=1}^N e^{i\rho_n} \sum_{m=1}^M H_{mn} q_m \right|^2. \quad (5.3)$$

The term independent of the optimization variable can be interpreted as the effective channel  $H_{\text{eff},n} = \sum_{m=1}^M H_{mn} q_m$  as seen by the  $n$ -th Tx. Being a complex number, it may be written in polar coordinates as  $H_{\text{eff},n} = |H_{\text{eff},n}| e^{j\angle(H_{\text{eff},n})}$ , where the operator  $\angle(\cdot)$  returns the phase of its argument. Thus, the outer sum in Eq. (5.3) is maximized when the phases of its complex summands are aligned. The simplest solution then results in

$$\rho_n^* = -\angle \left( \sum_{m=1}^M H_{mn} q_m \right). \quad (5.4)$$

Analogously, for a given channel  $\mathbf{H}$  and transmit vector  $\mathbf{p}$ , the optimization problem to find the optimal receive phase vector  $\boldsymbol{\psi}^*$  is given by

$$\boldsymbol{\psi}^* \in \underset{\boldsymbol{\psi} \in [0, 2\pi)}{\text{argmax}} \left| \sum_{m=1}^M e^{i\psi_m} \sum_{n=1}^N H_{mn} p_n \right|^2 \quad (5.5)$$

and the phases of an optimal EGC receive vector are calculated as

$$\psi_m^* = -\angle \left( \sum_{n=1}^N H_{mn} p_n \right). \quad (5.6)$$

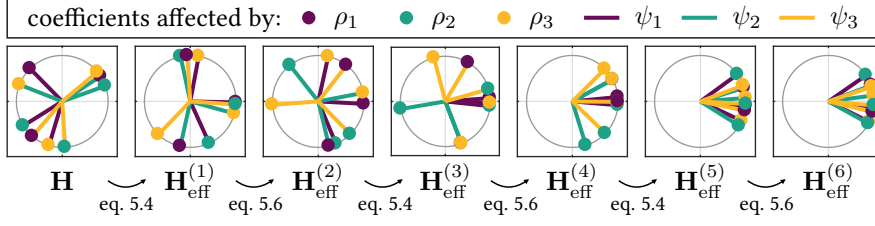


Figure 5.2: Evolution of the effective channel matrix throughout the first seven iterations of the suggested iterative optimization algorithm.

It is therefore possible to iteratively search for the nearest local optimum around an initial guess when alternately applying Eqs. (5.4) and (5.6) for EGT+EGC. As a result,  $|H_{\text{eff}}|^2$  increases with each iteration.

For illustrative purposes, we step through the phases of the algorithm using the following random  $3 \times 3$  MIMO channel matrix<sup>3</sup>:

$$\mathbf{H} = \frac{1}{\sqrt{3 \cdot 3}} \begin{bmatrix} e^{j2\pi 0.37} & e^{j2\pi 0.59} & e^{j2\pi 0.70} \\ e^{j2\pi 0.09} & e^{j2\pi 0.05} & e^{j2\pi 0.44} \\ e^{j2\pi 0.64} & e^{j2\pi 0.76} & e^{j2\pi 0.11} \end{bmatrix} \quad (5.7)$$

By writing the entries of  $\mathbf{p}$  and  $\mathbf{q}$  onto the diagonal elements of  $3 \times 3$  matrices, we obtain a matrix that can be interpreted as an effective channel matrix:

$$\begin{aligned} \mathbf{H}_{\text{eff}} &= \frac{1}{\sqrt{3 \cdot 3}} \begin{bmatrix} e^{j\psi_1} & 0 & 0 \\ 0 & e^{j\psi_2} & 0 \\ 0 & 0 & e^{j\psi_3} \end{bmatrix} \mathbf{H} \begin{bmatrix} e^{j\rho_1} & 0 & 0 \\ 0 & e^{j\rho_2} & 0 \\ 0 & 0 & e^{j\rho_3} \end{bmatrix} \\ &= \frac{1}{9} \begin{bmatrix} e^{j(2\pi 0.37 + \rho_1 + \psi_1)} & e^{j(2\pi 0.59 + \rho_2 + \psi_1)} & e^{j(2\pi 0.70 + \rho_3 + \psi_1)} \\ e^{j(2\pi 0.09 + \rho_1 + \psi_2)} & e^{j(2\pi 0.05 + \rho_2 + \psi_2)} & e^{j(2\pi 0.44 + \rho_3 + \psi_2)} \\ e^{j(2\pi 0.64 + \rho_1 + \psi_3)} & e^{j(2\pi 0.76 + \rho_2 + \psi_3)} & e^{j(2\pi 0.11 + \rho_3 + \psi_3)} \end{bmatrix} \quad (5.8) \end{aligned}$$

Summing over all elements of  $\mathbf{H}_{\text{eff}}$  yields the scalar effective channel  $H_{\text{eff}}$  as denoted in Eq. (5.1). The leftmost plot in Fig. 5.2 shows Eq. (5.8) with  $\rho_n, \psi_m = 0 \forall n, m$  or equivalently the exemplary channel coefficients from Eq. (5.7) on the complex plane. The following plots on the right show the resulting effective matrices  $\mathbf{H}_{\text{eff}}^{(i)}$  after the  $i$ -th iteration of applying Eqs. (5.4) and (5.6) alternately. The phasors sharing a *marker* color are affected by the same entry of the *transmit* phase vector  $\rho$ , while the phasors sharing a *line* color are affected by the same entry of the *receive* phase vector  $\psi$ . In this example, Eq. (5.4) is applied first and the *transmit* vector  $\mathbf{p}$  and thus its phase entries  $\rho_n$  are updated first. As a result, when going from  $\mathbf{H}$  to  $\mathbf{H}_{\text{eff}}^{(1)}$  the phasors with the same *marker* color are rotated by the same amount. In the second iteration, Eq. (5.4) is evaluated with the previously computed  $\mathbf{p}$ . Thus, when moving from  $\mathbf{H}_{\text{eff}}^{(1)}$  to  $\mathbf{H}_{\text{eff}}^{(2)}$  the phasors with the same *line* color are rotated by the same amount. After continuing these steps for four

<sup>3</sup> Admittedly, even though multiple random matrices were generated, this particular realization of a random matrix was chosen, because it shows a nice path across the cost function surface and does not converge too fast, hereby allowing to visualize the steps of the algorithm. Furthermore, the coefficients have equal amplitude. While this does not represent a realistic OWC channel, it helps in keeping the example simple.

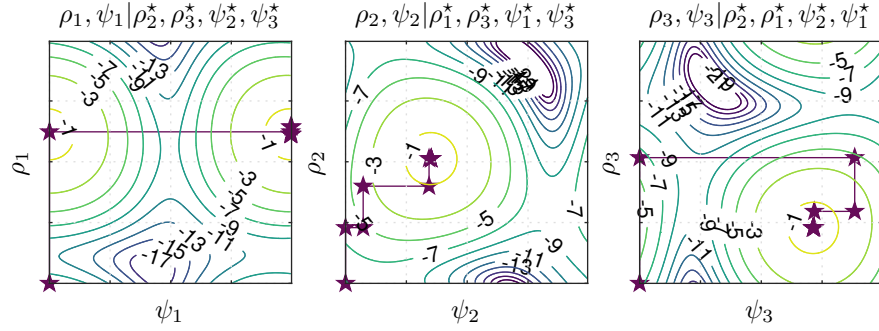


Figure 5.3: Cut through the 6-dimensional cost function. The numbers on the contour lines indicate  $|H_{\text{eff}}|^2$  in dB. For the given normalization, 0 dB is the global maximum.

further iterations, the phasors are mostly aligned along the real axis. With this improved alignment, the sum of these phasors and hereby the scalar effective channel  $H_{\text{eff}}$  results in a larger magnitude.

The cost function of this nonlinear optimization problem  $|H_{\text{eff}}|^2$ , is shown in Fig. 5.3. Since it is difficult to visualize it over the entire six-dimensional problem, we see three two-dimensional planes cutting through this six-dimensional space by keeping the respective four other dimensions fixed. Here, they are fixed at the resulting values after convergence of the algorithm. This way, the first graph shows the cost function's dependence on  $\rho_1$  and  $\psi_1$  for given  $\rho_2 = \rho_2^*$ ,  $\rho_3 = \rho_3^*$ ,  $\psi_2 = \psi_2^*$  and  $\psi_3 = \psi_3^*$ . The second and third graph respectively pair the second and third entries of the transmit phase vector  $\rho$  and receive phase vector  $\psi$ . The stars represent the resulting entries of  $\rho$  and  $\psi$  after each iteration. Starting at  $\rho = \psi = \mathbf{0}$ , only  $\rho_1$ ,  $\rho_2$  and  $\rho_3$  are updated after the first iteration, while after the second iteration only  $\psi_1$ ,  $\psi_2$  and  $\psi_3$  are updated. Quickly the adaptation finds its way to the resulting local maximum as indicated by the contour plot. The numbers on the contour lines indicate  $|H_{\text{eff}}|^2$  in dB. Note that with the given normalization, the maximum value  $|H_{\text{eff}}|^2$  can take is 0 dB.

Now that we have had a glance at the inner life of the phase adjustment algorithm for EGT+EGC with a simplified  $3 \times 3$  MIMO channel, we take a look at a measured  $8 \times 6$  MIMO channel to understand how the transmit and receive vectors can be further adjusted to the particularities of an OWC MIMO channel. For this purpose, we use an exemplary measured channel presented in following Section 5.2.2 obtained in a laboratory setup shown in Fig. 5.5a. Similar to before, the channel coefficients are shown in Fig. 5.4, however, for increasing frequencies. Due to the difference in distance from individual TxS to individual RxS, the angles of the phasors increase linearly by different amounts. Since a larger delay may be interpreted as a linear phase increment proportional to the delay, larger distances result in faster rotating phasors, more significantly so at higher frequencies. Thus, while at small frequencies the phasors are mostly aligned, they have significantly different angles at higher frequencies. The sum of all phasors without adjustment results in frequency-selective fading due to multipath propagation from multiple sources.

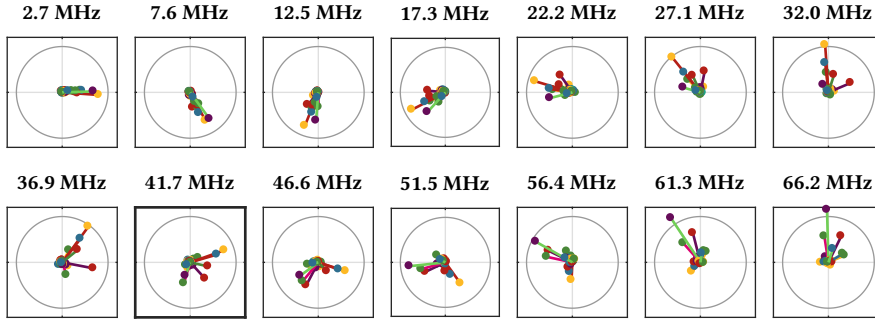


Figure 5.4: Channel coefficients of a measured  $8 \times 6$  MIMO channel at increasing frequencies. For better visual comparison, they are normalized such that the sum of the phasor magnitudes is constant at all frequencies.

Conveniently, the correlation between channel coefficients at adjacent frequencies is a property that can be exploited for improved convergence behavior of the algorithm presented thus far. Since in the case of OWC, the entries of  $\mathbf{H}$  are real-valued and non-negative at the frequency  $f = 0$ , we know a global optimum is obtained for  $\rho_n^* = \psi_m^* = 0$ . Considering, e.g., the case of DCO-OFDM we may use the resulting solution as an initial guess for the smallest subcarrier and its solution in turn for the next higher subcarrier. This is repeated until  $\mathbf{p}$  and  $\mathbf{q}$  are known for all subcarriers. The resulting improvement of convergence and the comparison to other general purpose solvers for unconstrained nonlinear optimization is presented in detail in Appendix A.3.

So far we have focused on the unconstrained nonlinear optimization problem resulting from the combination of EGT and EGC. However, if we want to employ EGT with MRC, the constraint  $\|\mathbf{q}\|_2 = 1$  turns the problem into a constrained nonlinear optimization problem and general purpose nonlinear optimization schemes need significant adaptation [136], [137]. The suggested iterative optimization however is easily adapted: Instead of applying Eq. (5.6) to update the receive phase vector  $\boldsymbol{\psi}$  and thus indirectly the receive vector  $\mathbf{q}$ , we may compute the MRC receive vector directly as [135]

$$\mathbf{q} = \frac{(\mathbf{H}\mathbf{p})^*}{\|\mathbf{H}\mathbf{p}\|_2}, \quad (5.9)$$

where  $(\cdot)^*$  the complex conjugate. By alternately applying Eqs. (5.4) and (5.6), we can thus apply the suggested iterative optimization to either EGT with EGC or EGT with MRC, when Eqs. (5.4) and (5.9) are used. The following section experimentally investigates the gains of the iterative optimization over the case of simply summing over the entries of the channel matrix  $\mathbf{H}$  without phase adaption in the transmit and receive vectors.

### 5.2.2 Experimental Setup and Results

The reduced size,  $1.45 \text{ m} \times 1.45 \text{ m} \times 1.45 \text{ m}$  manufacturing cell replica used for the following transmission experiments is shown in Fig. 5.5a. As in the channel measurements in Chapter 4, six Tx were placed on the faces of a cube

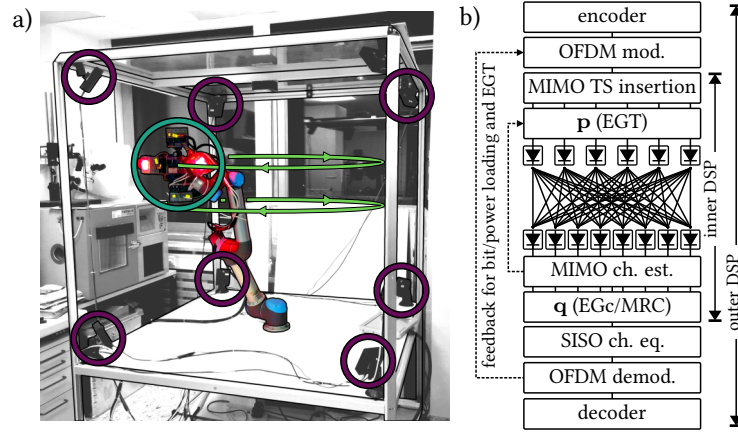


Figure 5.5: a) Photograph of robotic manufacturing cell replica used for  $8 \times 6$  MIMO experiments. Purple and green circles highlight the Rx and Tx, respectively. The light green circles sketch the trajectories along which the Tx were positioned by the robot. b) Block diagram of the DSP used for the transmission experiment.

and attached to the end of a manufacturing robot's arm, where tools with OWC modules would also be located. The eight Rx front ends were placed on the corners of the cell. Allowing for a straight-forward implementation of the per-subcarrier phase adjustment discussed in the previous section, DCO-OFDM transmissions were performed from 36 positions over a bandwidth of up to 100 MHz. Figure 5.5b gives an overview on the DSP, which may be split into two parts.

Table 5.1:  
OFDM DSP

$N_{\text{DFT}}$	2048
$\mathcal{S}$	11-410
$N_{\text{CP}}$	128
$R_s$	500 MS/s
OH	6.1%
$\mathcal{M}$	2,4,16,32,64, 128,256,512, 1024,2048,4096
BPL	Krongold
FEC	LDPC
$R_{\text{FEC}}$	5/6
$G_{\text{phy},n}$	56-196 Mb/s

The inner DSP effectively converts the MIMO channel into a SISO channel via the transmit/receive  $\mathbf{p}/\mathbf{q}$  vectors presented in the previous section. For the calculation of  $\mathbf{p}$  and  $\mathbf{q}$  the channel  $\mathbf{H}$  must be known. Therefore the inner DSP includes the framing synchronization and MIMO training sequences (TSs) orthogonal in frequency domain. Essentially, the same MIMO channel estimation approach as in Section 4.1.2 is employed, except that all pilot frequencies are transmitted simultaneously<sup>4</sup> and with the same discrete Fourier transform (DFT) size  $N_{\text{DFT}}$  as the payload. More explicitly, out of the set of unmasked subcarriers  $\mathcal{S}$  used by the payload, the TS used by the  $n$ -th Tx uses the subset  $\mathcal{S}_n = \{l \in \mathcal{S} : l \bmod 6 = (n+10) \bmod 6\}$ . The estimated channel at these scattered pilot frequencies is then interpolated as described in [104]. In the following experimental validation, we investigate three types of antenna diversity, which differ solely in the  $\mathbf{p}$  and  $\mathbf{q}$ : either *unmatched transmission*, in which  $p_n = \frac{1}{\sqrt{6}}$  and  $q_m = \frac{1}{\sqrt{8}}$ , or the pairs EGT+EGC and EGT+MRC. For the last two we use the iterative optimization described in the previous section with five iterations per subcarrier. A transmission employing MRT+MRC was not possible as the digital readjustment of the transmit powers lead to immense clipping.

The outer DSP consists of the residual SISO DCO-OFDM processing chain described in Section 2.3.1. This includes the equalization of the SISO channel, demodulation and error vector magnitude (EVM) estimation. Based on the resulting EVM, bit and power loading (BPL) is performed as described in

<sup>4</sup> This significantly reduces the OH at the cost of an increased PAPR.

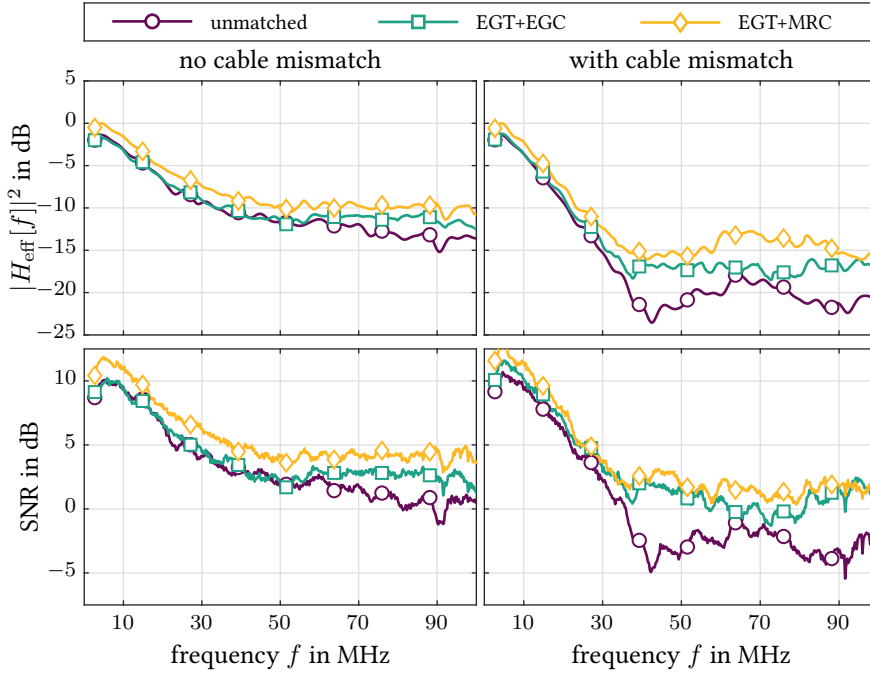


Figure 5.6: Exemplary frequency dependent effective channel  $H_{\text{eff}}$  (top) and resulting SNRs (bottom) for multiple diversity schemes when equally long cables are used to connect all Rx (left) and when minimally short cables are used (right).

[105]. After BPL, decoding and bit error rate (BER) counting is performed to verify error-free transmission of a fully loaded transmission. The target BER fed to the BPL algorithm was  $10^{-2}$ , which lied below the expected forward error correction (FEC) threshold of approximately  $2 \cdot 10^{-2}$  [127].

The upper graphs of Fig. 5.6 illustrate the measured effective channels  $H_{\text{eff}}$  when matched cable lengths are used to avoid different path delays (left) and when minimally short cables are used (right). The latter may be the case in actual deployment scenarios in larger geometries, where unnecessarily long cables should be avoided and/or equal length cannot be guaranteed. While EGT+MRC increases the channel gain over all frequencies, EGT+EGC shows improvements only at frequencies at which there is a phase mismatch. This effect is significantly stronger when cables of different lengths are used. Thus, for signals with bandwidths below approximately 50 MHz (30 MHz when mismatched cables are used), we may expect the adjustment of phases in the transmit/receive vectors to yield little gain. The bottom graphs of Fig. 5.6 show the corresponding SNRs of the 400 subcarriers, which closely follow the frequency-dependent channel coefficients. Together with BPL algorithm, the gains in SNR may be used to increase the system's throughput.

Figure 5.7 shows the empirical cumulative distribution functions (CDFs) of achieved net throughputs resulting from BPL with [105]. Achieving the highest rates, the improvements of EGT+MRC over an unmatched transmission in lowest, average and peak data rates are shown in percent. The pure phase adjustment of  $\mathbf{p}$  and  $\mathbf{q}$  (EGT+EGC) becomes mostly relevant

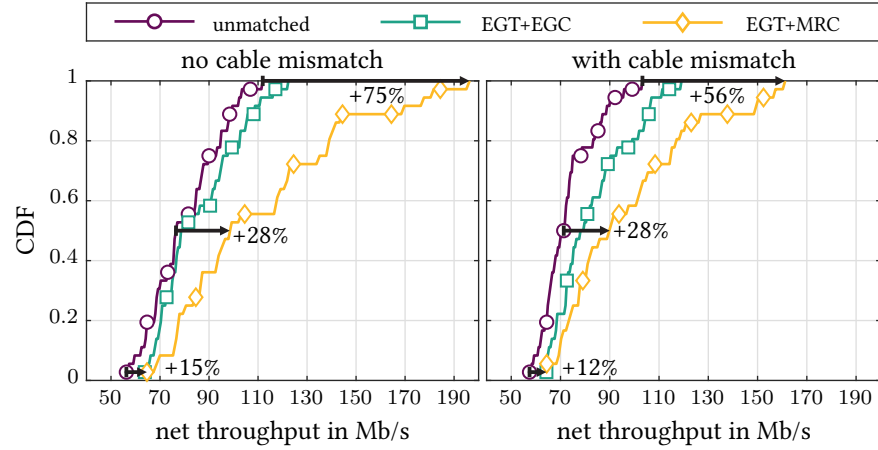


Figure 5.7: Distribution of net throughputs for multiple diversity schemes. The arrows and percentages indicate the gain of EGT+MRC over an unmatched transmission.

when mismatched cable lengths are used. However, the lowest data rate, an indicator for robustness, is the same for EGT+EGC and EGT+MRC.

For broadband transmission of up to 100 MHz, we see that adjusting the phases of the transmit and receive vectors  $\mathbf{p}$  and  $\mathbf{q}$  can significantly improve the received signal quality at higher frequencies. The use of a transmit-side phase adjustment and MRC at the Rx improved the lowest, median and peak rates by up to 15 %, 28 % and 75 %, respectively. Note that while in this experimental evaluation maximally achieved data rates served as an indirect indicator of improved channel gains, these gains may be used alternatively to increase the SNR margin of our communication system. This makes the pair of EGT+MRC, enabled by the suggested algorithm for iterative optimization of the transmit and receive vectors, an interesting component for a broadband industrial OWC system.

However, since an optimization of the phases of the transmit and receive vectors yields small gains at low frequencies, simplifications are possible when the waveform in use occupies only a limited bandwidth. The next section thus presents experimental results obtained in the full size manufacturing cell at BMW for a narrowband transmission.

### 5.3 NARROWBAND TRANSMISSION

To avoid confusion, it should be clarified that, chronologically, the narrowband transmission experiment was conducted prior to the broadband transmission. In fact, it was conducted in immediate succession to the channel measurements discussed in Chapter 4 with the same setup and along the exact same trajectory. Facing larger propagation distances and hardware build for high bandwidth and linear channel sounding, broadband transmission was simply not possible due to too little optical signal power. This section therefore focuses on the transmission of a narrowband signal, employing antenna diversity schemes over the measured channels depicted in Fig. 4.6. The DSP and transmission results are presented in the following paragraphs.

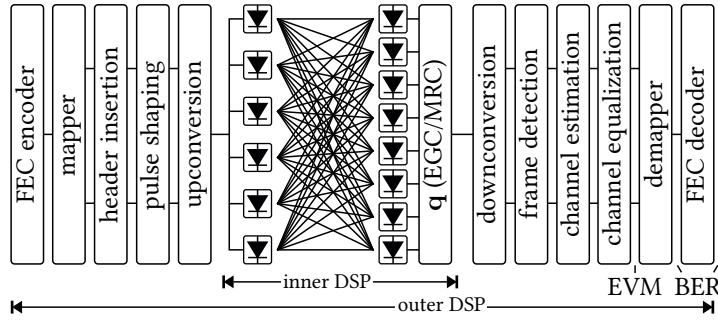


Figure 5.8: Block diagram of the DSP used in the 1 Mb/s transmission experiment. The inner DSP consists of equal gain transmission at the Tx and maximal ratio combining or equal gain combining at the Rx. The outer DSP consists of the SC DSP designed for a coded IM/DD QPSK transmission.

### 5.3.1 Digital Signal Processing and Results

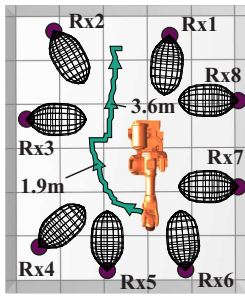
The waveform chosen for this transmission experiment was a single-carrier (SC) quadrature phase-shift keying (QPSK) with a root-raised-cosine (RRC) pulse shape (PS) of rolloff  $\beta = 1.0$ . It was selected for its low peak-to-average power ratio (PAPR) of 6.5 dB<sup>5</sup> measured after the upconversion of the SC. For the given front ends, optical signal power  $\tilde{P}$  could only be adapted by variation of the electrical signal power  $\tilde{P}_e$ , which was in turn peak-limited by the dynamic range of our digital-to-analog converters (DACs). Therefore, for this given peak-power limitation, the reduced PAPR allowed for an increased average power, yielding a higher SNR. Similar to the broadband transmission, the DSP of this experiment may be split into two parts (see Fig. 5.8). The outer part of the DSP performs all steps needed for a classical single-carrier modulation scheme introduced in Section 2.3.2. The inner part of the signal processing handles the MIMO channel and converts it into an effective SISO link for the outer part via simple EGT at the Tx and MRC or EGC at the Rx [135], [140].

Since for MRC the SNRs at each Rx need to be known a priori, they are estimated by computing the signal power in the transmission passband around the intermediate frequency of 3.5 MHz and a noise power around 5.5 MHz prior to down conversion. The hereby estimated SNR at each Rx and each position along the trajectory are shown in the left plot of Fig. 5.9. As the transmission was performed along the same trajectory as the channel measurements presented in Chapter 4, a division into three sections, i.e., a first section with only a few strong channels, a second section with multiple weak channels and a third section with only a few weak channels, is also possible in the transmission experiment. Due to their proximity, we may observe that Rxs 5, 6 and 7 receive the signal with high SNR within the first section. For section 2 and 3 the SNR of individual Rxs is below the

Table 5.2:  
SC-QPSK DSP

PS	RRC
$\beta$	1.0
$\mathcal{M}$	4
$R_{\text{sy}}$	625 kBd
$f_c$	3.5 MHz
$R_s$	500 MS/s
PAPR	6.5 dB
OH	2.5%
FEC	LDPC
$R_{\text{FEC}}$	5/6
$G_{\text{phy,n}}$	1 Mb/s

<sup>5</sup> As a comparison, the PAPR of simple DCO-OFDM are easily >10 dB if no additional means for PAPR reduction are performed [138], [139].



As a reminder:  
Trajectory with  
boundaries of sections  
1/2 and sections 2/3 at  
1.9 m and 3.6 m.

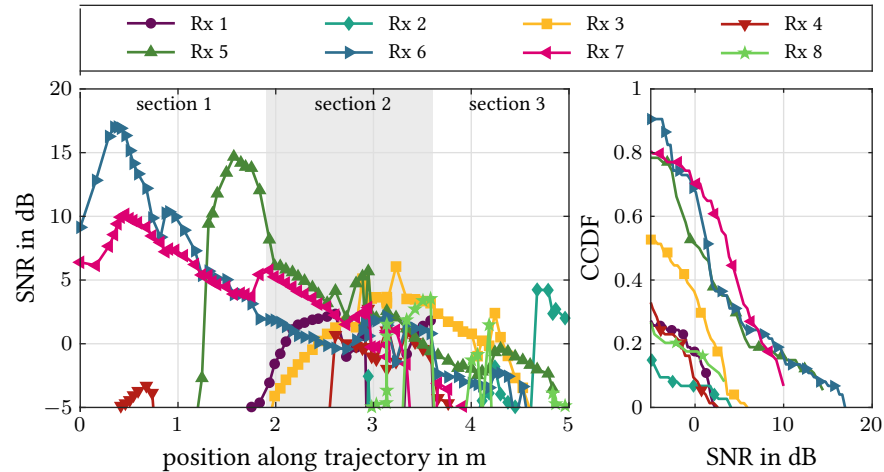


Figure 5.9: Received SNR per Rx along the trajectory (left) and the resulting empirical CCDF (right). The Rx with best visibility (Rx 7) achieves an SNR above 5 dB from 35 % of the positions.

minimally required 5 dB<sup>6</sup> most of the time. The right graph shows the empirical complementary cumulative distribution functions (CCDFs)<sup>7</sup> of these values. This representation shows that for all Rxs the received SNR is below 5 dB at most of the positions along the trajectory. The CCDF reveals that for Rx 7, which has the best visibility throughout the trajectory, the threshold of 5 dB in SNR is only achieved from 35% of the positions. This illustrates the requirement for spanning a MIMO channel, which allows to exploit spatial diversity, e.g., to obtain a single, more reliable channel with higher gain.

Although it is possible to estimate the SNR from the signals' spectra, employing the received electrical signal power  $\tilde{P}_{e,r}$  as a measure for the calculation of the entries of the receive vector  $\mathbf{p}$  is of interest, since its estimation does not require knowledge on the noise power levels. Furthermore, in case of equal noise per Rx, it is proportional to the SNR. While this condition may not always be met, the choice of power over SNR was found to make no difference in this particular measurement series, but strongly simplifies the DSP when noise power measurements are not possible. In case of EGC, the received signals are thus sorted by their power and only the strongest are combined, where the number of used Rx is varied from one to eight. The use of only the single strongest signal is equivalent to selection combining (SLC), whereas the use of all eight signals may be considered as the classical EGC scheme.

Figure 5.10 shows the resulting SNRs, when Rx-side antenna diversity schemes are employed. Over all sections, MRC provides the highest SNR when compared to all EGC cases as it is expected from an SNR maximizing scheme. More interestingly, the EGC schemes perform differently in the

<sup>6</sup> From additive white Gaussian noise theory the minimum required SNR for a capacity of 2 bit is 4.77 dB. However, for the given experiment, DSP and FEC, error-free transmission was only possible for SNRs above 5 dB.

<sup>7</sup> The graph may be read as follows: "For a given SNR value, the empirical CCDF indicates the relative frequency of channels with equal or higher SNR."

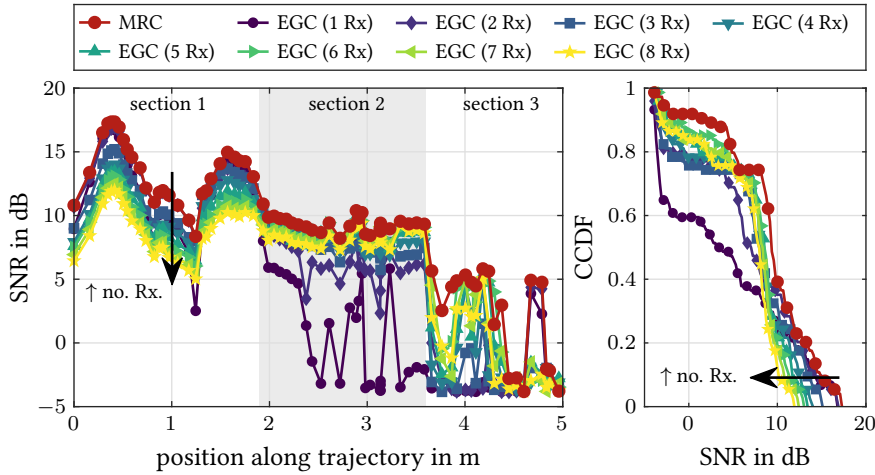


Figure 5.10: Estimated SNR and corresponding empirical CCDF when MRC or EGC is applied. EGC is performed only over the Rx's with most power, where the number of Rx's in use is varied and denoted in parenthesis (see legend). The sections observed in the previous channel measurements are highlighted in the left axis.

first two sections depending on the number of Rx in use. The use of fewer Rx's is beneficial when a small number of strong channels dominate over all other channels, as the channels with low signal power will mostly contribute with noise. This is the case in section 1, where for EGC the use of only the two strongest Rx's yield best results. The use of more Rx improves the resulting signal quality significantly in the next two sections, where multiple similarly strong, yet rather weak signals are received. This is also visible in right plot of Fig. 5.10, where the empirical CCDFs of the SNR are shown for each diversity scheme. While the EGC schemes using more Rx achieve the minimally required SNR of 5 dB at more positions along the trajectory, the maximally achieved SNRs are visibly reduced. However, for an application in a production environment, we are concerned with designing a simple, yet reliable communication system and therefore aim to minimize the number of positions at which communication is not possible.

In the presented transmission experiment, the selection of the best six Rx for EGC shows a good performance in the low SNR regime. For this case and the MRC scheme the measured BERs before and after FEC decoding are shown in Fig. 5.11. At each position,  $> 1.6 \cdot 10^6$  bits are evaluated to count the post-FEC BER. The positions at which error-free communication was not possible lie in the third section and are highlighted in the bottom right graph of Fig. 5.11. Error-free transmission for MRC and EGC with six Rx was possible at 80% and 76% of the robot positions, respectively. This is a good improvement compared to the use of single Rx's without SLC, where in the best case, transmission would only be possible from less than 35% of the positions. While full coverage was not possible with either approach, it is important to point out that the measured channels depicted in Fig. 4.6 indicate that the problem was not full blockage of all LOS paths, but limited overall signal power. Tx front ends with higher optical transmit power can

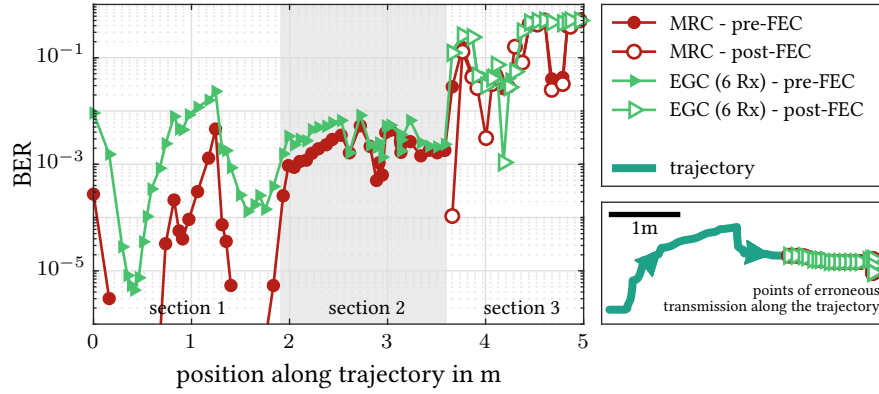


Figure 5.11: Estimated BER before and after the LDPC decoder, when MRC/EGC is applied. For EGC, we show the case for six Rx. Error-free transmission is possible in the first two sections. In the third section, the FEC could not correct all errors. Points along the trajectory, at which error-free communication was not possible, are shown in the bottom right graph and highlighted by the green and red markers

thus be expected to further improve coverage. A major limitation in the last two transmission experiments was therefore the limited achievable SNR, which is attributed to the use of front ends designed for broadband channel sounding and the use of no lenses at the Tx.

#### 5.4 ANALOG COMBINING AND REAL-TIME IMPLEMENTATION

The insights of Chapter 4 and this chapter so far lead to a redesign of the optical Tx and Rx front ends with a smaller targeted bandwidth of up to 50 MHz (instead of 200 MHz), which mitigates the problem of weak optical signal powers. In fact, the investigation of nonlinearities in Chapter 3 was performed with such reduced bandwidth, high power front ends [43]. Furthermore, Tx and Rx were integrated into single TRxs - a fundamental requirement for bidirectional communication. Together with an analog combining circuitry presented in the next section, which is capable of performing SLC, EGC and MRC, these front ends are important building blocks of the real-time OWC system presented at the end of this thesis.

##### 5.4.1 Analog Combiner

The basic idea behind the analog combiner is that the MRC weights of the receive vector  $\mathbf{q}$  may be computed from the received powers as was verified in the previous section. Note that the knowledge of the effective single-input multiple-output (SIMO) channel coefficients is required in Eq. (5.9). However, assuming the input signal  $x$  has a constant average power and the received SNR is sufficiently large, an estimate  $\hat{\mathbf{q}}$  of the ideal receive vector may be obtained by setting its entries proportional to the standard deviation of the entries in the received signal  $\mathbf{y} = \mathbf{H}\mathbf{p}x + \mathbf{n}$  before combining. This realization was used to build an analog combining circuitry.

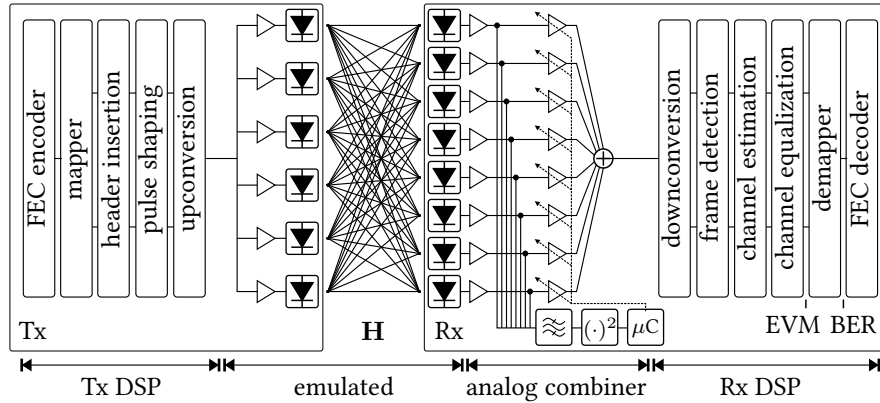


Figure 5.12: Block diagram of the DSP and setup used to validate the analog combining circuit. Sections *Tx DSP*, *emulated* and *Rx DSP* are performed in the digital domain, which is interfaced with *analog combiner* via DACs and an ADC.

A sketch and a photograph of the analog combining circuit are shown in Figs. 5.12 and 5.13, respectively. Since Fig. 5.12 also depicts the test setup used to evaluate the performance of the circuitry, we do now focus only of the section indicated as *analog combiner*. For each of the up to eight received signals, a bandpass filter serves as a projection to the subspace by which the original signal  $x$  resides, similar to a matched filter, and essentially filters out noise, which would distort the signal power measurement. Each filter is followed by a power meter, which outputs a voltage approximately proportional to the power of each received signal. These voltages are sampled by a 8-bit micro controller ( $\mu C$ ) [141] and processed as follows: The inaccurate and nonlinear power-transfer function of the power meter is corrected via a look-up-table (LUT), which contains the inverse power-transfer function. Afterwards, the corrected power values are used to set eight digitally controlled attenuators in the signal path in a range of 0-31.75 dB, whose outputs are added in the analog domain. For the given simple  $\mu C$  and its built-in analog-to-digital converter (ADC), the update rate of the attenuators is limited to approximately 2 kHz. The state of the attenuators can be read out via a serial port, which is also used for configuring the Rx-side combining scheme. In case of MRC, the strongest signal is always set to an attenuation of 0 dB, while the other attenuators are set according to their difference to the dominant signal. In case of EGC all attenuators are set to 0 dB attenuation. Additionally, SLC



Figure 5.13: Photograph of the analog combiner circuitry.

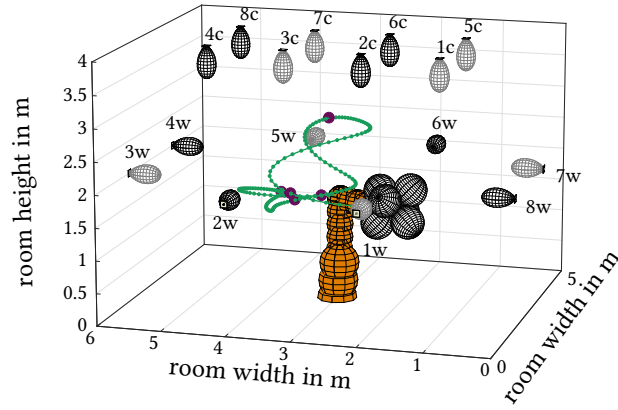


Figure 5.14: Model of a manufacturing cell. The orange spheres represent the robot arm, which blocks light paths. In this UL configuration six Tx are mounted at the robot's head and eight Rx are either placed on the walls (postfix w) or on the ceiling (postfix c) of the cell. Due to the limited number of DACs, only four Rx were used to test the combiner. Those not used are grayed out.

can be performed, when the signal from single Rx is considered, by setting its attenuation to 0 dB, whilst the other channels are set to the maximal attenuation of 31.27 dB.

The next section presents how the analog combiner performs with SLC, EGC and MRC when fed with synthesized outputs of a OWC MIMO channel.

#### 5.4.2 Evaluation

In order to test the analog combining circuit with realistic MIMO LOS channels, a simplified model of a 5 m x 6 m x 4 m manufacturing cell with non-reflective walls and a robot positioned in its center is used (see Fig. 5.14). The robot arm consists of four segments with 0.6 m, 1 m, 1 m and 0.3 m in length. Each segment is modeled with multiple non-transparent/non-reflective spheres of radius 0.3 m, 0.2 m, 0.2 m and 0.02 m, respectively. The spheres are spaced with their radius along the corresponding segment, resulting in an approximation of a robot arm, which may block a LOS. In Fig. 5.14, this robot model is represented by the orange spheres. Five positions of the robot arm are chosen randomly (purple markers) and interpolated to result in a total of 200 points. This yields a smooth trajectory with cyclic boundary conditions, i.e., the same start and end point. This trajectory is depicted in Fig. 5.14 as a green line. At each point, the entries  $H_{mn}$  of the  $M \times N$  LOS MIMO channel matrix  $\mathbf{H}$  is calculated according to Eq. (2.26) for both, UL and DL in two configurations. In the first configuration, the immobile TRx are placed on the walls, whereas in the second configuration they are placed on the ceiling. It is noteworthy, that the UL case with mobile Txs on the robot and immobile Rxs placed on the walls, corresponds to the circumstances given in the channel measurements from Chapter 4 and transmission experiments in Sections 5.2 and 5.3.

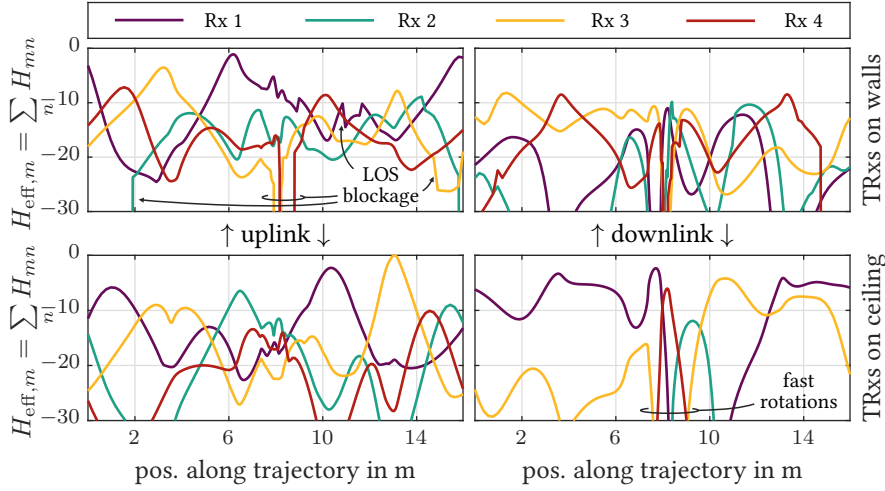


Figure 5.15: Effective SIMO channels along the trajectory as seen by the four receivers in use. The channels are normalized to the strongest effective channel. Abrupt LOS blockage occurs only when the immobile TRx are placed on the walls and the robot may obstruct the LOS.

The target of this channel synthesis, is to use it for an emulation of a MIMO channel with realistically varying channel coefficients. Therefore, as Fig. 5.12 suggests, a SC signal is generated, its transmission over an OWC MIMO channel is emulated and the resulting noisy waveforms are uploaded to synchronized DACs, which feed the inputs of the analog combiner. Note that due to the availability of only four differential DACs, only four inputs of the analog combiner could be tested simultaneously. Thus, in the UL cases we have  $N = 6$  Tx and  $M = 4$  Rx, in the DL  $N = 8$  Tx and  $M = 4$  Rx. For the UL case, the four Rx in use are denoted in Fig. 5.14 as 2w, 4w, 6w and 8w when placed at the walls and 2c, 4c, 6c and 8c when placed on the ceiling.

The resulting effective SIMO channels, when all Tx transmit the same signal with equal gain (i.e., EGT) as seen by each Rx, are shown in Fig. 5.15. The top and bottom graphs show the channels when TRxs are mounted on the walls and ceiling, respectively. While the graphs in the left axes correspond to the channels obtained in the UL, the right axes correspond to the DL. It may be observed that the channels show similar fluctuations to those measured and presented in Chapter 4, i.e., channel coefficients vary strongly depending on the position/orientation of the robot. While some parts of the trajectory are dominated by single links (e.g., first 6 m in bottom right axis), in other parts multiple similarly strong channels exist (e.g., around 11-14 m in top left axis). However, compared to the channel measurements<sup>8</sup>, we observe fewer abrupt changes in the channel coefficients due to LOS blocking (see, e.g., top left axes). This is due to the fact, that in this simulation the spheres representing the robot are the only LOS-blocking obstacles. As a result, when the TRxs are located at the ceiling, a LOS between all Txs and any individual Rx is never blocked abruptly by the robot. In this case, fast channel changes

<sup>8</sup> Note that as a UL configuration with Rxs on the walls, only the top left axis corresponds to the setup in the channel measurements of Chapter 4.

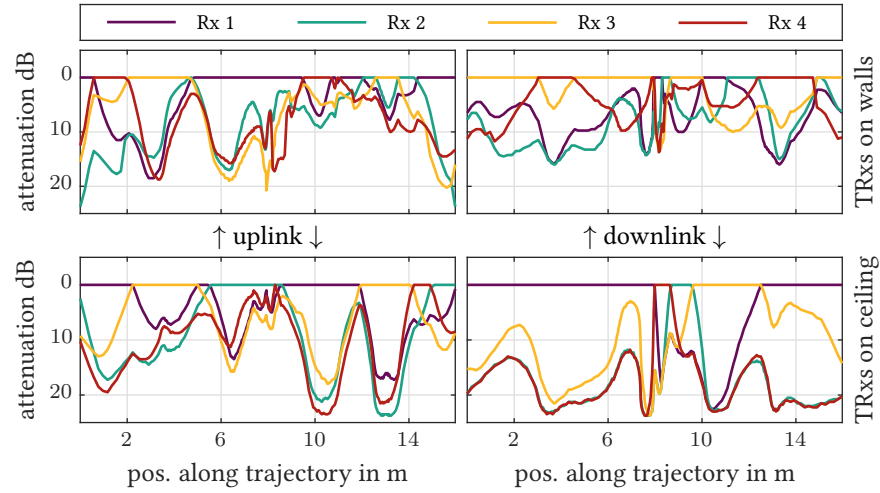


Figure 5.16: Attenuation values set by the  $\mu\text{C}$ , when the analog combiner is configured to perform MRC. The attenuation of Rxs facing the best channel condition is always set to 0 dB.

as highlighted in the bottom right axis of Fig. 5.15 are smooth and rather a result of fast rotations.

Table 5.3:

SC-QPSK DSP	
PS	RRC
$\beta$	0.5
$\mathcal{M}$	4
$R_{\text{sy}}$	15.625 MBd
$f_c$	15.625 MHz
$R_s$	62.5 MS/s
OH	2.5%
FEC	LDPC
$R_{\text{FEC}}$	5/6

In order to test the analog combining circuitry on such MIMO channels, a SC waveform is used. The Tx and Rx DSP employed for the experiment was already depicted in Fig. 5.12 and is now explained in detail. FEC encoded bits are mapped to a QPSK symbol alphabet, after which a header for frame detection and channel estimation is inserted. The resulting symbols with a rate of 15.625 MBd are shaped with a RRC pulse shape with a roll-off  $\beta = 0.5$  and upconverted to an intermediate frequency of 15.625 MHz. The resulting signal is distorted by the emulated MIMO channels and white Gaussian noise is added, which emulates receiver-side noise of optical front ends. The noise power is set such that the best channel would result in an SNR of 30 dB. This value is chosen to be approximately in accordance with the measured SNRs for a transmit distance of 1-2 m presented in Chapter 3. The noisy samples of four emulated Rxs are then uploaded to four synchronized 14 bit resolution DACs working as a sample rate of 62.5 MS/s with a bandwidth above 200 MHz, whose outputs are connected to the analog combining circuitry. The circuit is configured to perform either SLC, EGC or MRC. Its output is sampled by a single ADC working at a sample rate of 62.5 MS/s with a bandwidth above 200 MHz. The sampled signal is digitally down-converted to complex baseband, where the training sequences are detected and used for channel estimation and equalization. After equalization, the SNR is derived from the EVM. The pre-FEC BER is estimated after de-mapping. For the results shown here, the soft-decision de-mapping and FEC correction is not employed.

Since the attenuation values set by the  $\mu\text{C}$  may be read via a serial port, they are displayed in Fig. 5.16 for the case that the  $\mu\text{C}$  is configured to perform MRC. As previously stated, in this configuration, the attenuation of the strongest channels is set to 0 dB and the weaker Rxs are attenuated accordingly to the received power. The attenuation values of the non-dominant

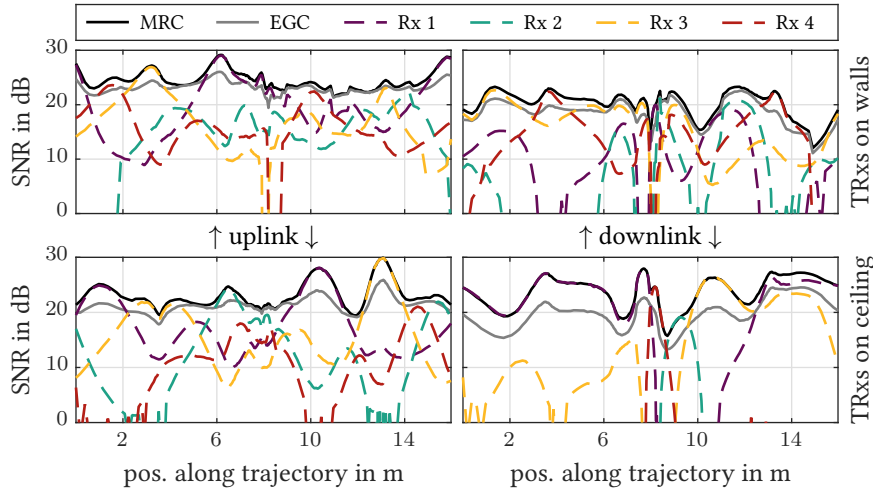


Figure 5.17: Measured SNR when using only single Rxs and for EGC and MRC, which are implemented on the combining circuitry. For SLC, the best of the single Rx cases is considered. As an SNR maximizing scheme, the approximated MRC yields the highest SNR at each position.

channels thus closely follow the gain difference to the dominant channel coefficient (see Fig. 5.15 for comparison).

The resulting SNRs are shown in Fig. 5.17 for the three previously described combining configurations. The SLC results serve as a reference and are shown for the four channels individually. Note how the resulting SNRs for individual Rx closely follow the SIMO channel coefficients shown in Fig. 5.15. If applied correctly, a SLC scheme makes use of the best channel at each position. Along the trajectory, EGC reduces the SNR variations and suffers from noisy channels, when only a few strong channels are available (e.g., first 6 m in bottom right axis). The targeted MRC scheme outperforms all the presented reference combining schemes as the analog circuit successfully adapts to the given channel conditions.

Figure 5.18 shows the empirical CDFs for each combining scheme and the use of single Rxs in all scenarios. Since for the targeted communication system, reliability is the most important property, the lower left part of the CDF is of particular interest. For the case that single Rxs are used, the minimally required SNR of 5 dB for a QPSK is not reached at all positions of the emulated trajectory. Thus, the value of the CDF at 5 dB indicates the empirical outage probability, i.e., the experimentally observed probability with which communication is not possible. With the use of single Rxs, this ranges from 4% to 56%. For the combining schemes, i.e., MRC, EGC and SLC, no outage is observed and the lower left part of the CDFs indicates the lowest achieved SNR. For high reliability, it is desired that this smallest resulting SNR is as high as possible, since it indicates a larger SNR margin. In all UL/DL configurations this is achieved by the MRC scheme performed in real-time by the analog combining circuitry. Using either of the implemented combining schemes a link with sufficiently large SNR is established at each point of the trajectory under consideration. It is worth mentioning that the pre-FEC BER was always below  $8 \cdot 10^{-5}$ ,  $4 \cdot 10^{-4}$  and  $5 \cdot 10^{-3}$  for MRC, EGC and SLC,

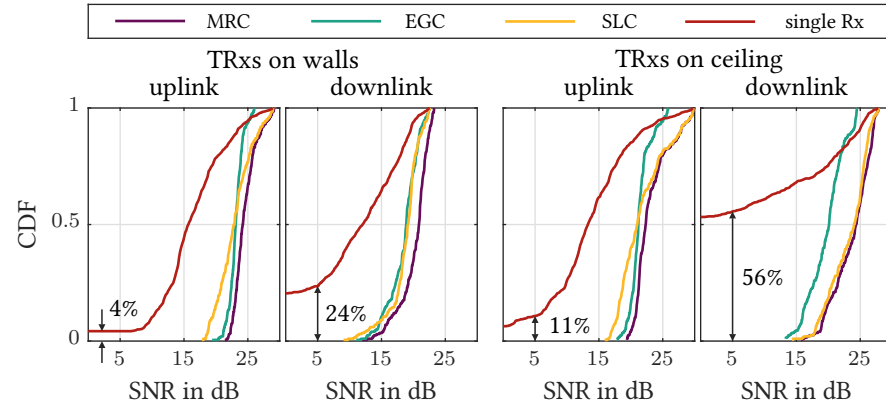


Figure 5.18: Cumulative distributions of the SNR values obtained in each scenario for maximal ratio, equal gain and selection combining. The empirical outage probability for the case of single Rxs is shown in percent.

respectively. These lie well below the expected threshold of  $2 \cdot 10^{-2}$  of the low-density parity-check (LDPC) FEC with rate 5/6 used in other evaluations in this thesis.

These tests in the electrical domain have validated the functionality of the analog combining circuitry and shown its working principle. Based on this circuitry, we are able to practically convert a distributed MIMO<sup>9</sup> channel, which may consist of multiple unreliable spatial links, into a reliable SISO channel. For such a channel, efficient baseband DSP chipsets exist, which can be employed jointly with the presented analog combining scheme and hereby create a reliable real-time OWC system. The operation of such a system is presented in the next section.

#### 5.4.3 Field-Trial with Reliable Real-Time OWC System

The manufacturing cell that served as a test environment for the real-time OWC system has already been presented in Section 4.1.3 and is depicted in Fig. 5.19a. However, the communication system has evolved to support bidirectional transmission and higher distances in real-time. Therefore, the all modules shown in the photographs of Fig. 5.19 of said cell are not either *Txs* or *Rxs*, but optical *TRxs* front ends with larger modulation indices [43]. In the following, we differentiate between the MU, which can be moved freely around the cell and can thus also be attached to the robot itself, and the access point (AP). The six TRx front ends of the MU are mounted on the faces of a cube and shown in Fig. 5.19a/b. The AP consists of eight optical TRx front ends, which are shown in Fig. 5.19a/c and placed on the edges of the cell. The separation of front ends ensures that the spatial diversity is high and multiple links are less likely to be blocked simultaneously. Due to the analog implementation of the diversity schemes, no handover on higher layers is required, resulting in a reliable communication system with rather

<sup>9</sup> Technically, this circuitry performs only the conversion from a SIMO channel into a SISO channel. The circuitry dispensing the same signal to multiple Tx front ends is not further discussed due to its simplicity.

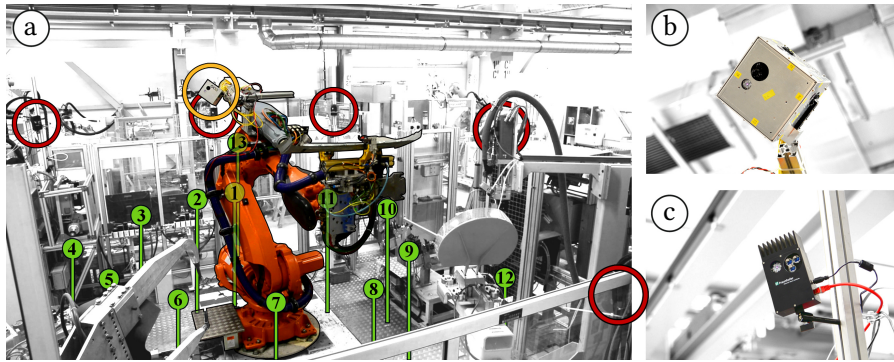


Figure 5.19: a) Manufacturing cell. The MU and front ends of the AP are highlighted by yellow and red circles, respectively. For experiments in which the MU was not mounted to the robot, green markers indicate 13 measurement points. b) Front ends of the MU. c) Single front end of the AP.

low latencies. In the following paragraphs, the evaluation of this system with respect to throughput and latency of Ethernet packet transmissions is presented.

Figure 5.20 shows a block diagram of the measurement setup: An Optixia XM2 with 1G Ethernet cards was used to generate arbitrary Ethernet traffic and evaluate the performance of the bidirectional OWC system. This traffic was processed by a commercially available, ITU-T G.hn compliant [98], [142], baseband DSP unit. This OFDM-based unit was configured to use 481 subcarriers on a range from 2.15 MHz to 95.90 MHz, resulting in a subcarrier spacing of 195.3 kHz. Its generated OFDM waveform was distributed to six (UL) or eight (DL) infrared LEDs with a center wavelength of 850 nm and half-power semi-angles (HPSAs) of  $45^\circ$  [67], received by eight (UL) or six (DL) photodiodes (PDs) with HPSAs of  $35^\circ$  [68], processed by the analog combiner and then passed to the receiving baseband DSP unit. Note that these DSP units have their own full protocol stack including FEC and automatic repeat request (ARQ) mechanisms [98], [142]. From point of view of the Ixia network test equipment, the DSP units acted as Ethernet bridges. The output Ethernet packets were further processed by the Optixia XM2. Resulting packet error rates (PERs) and per packet latencies were measured

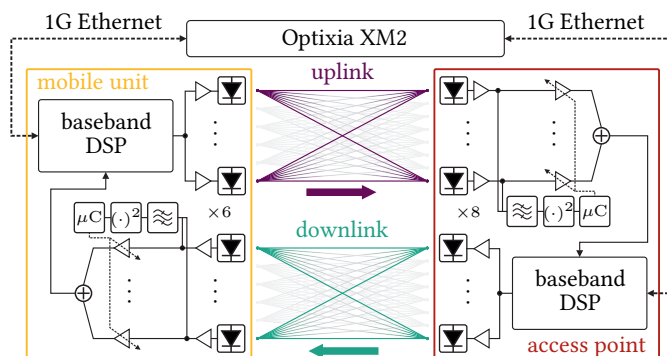


Figure 5.20: Block diagram, which indicates the key components of the reliable real-time OWC system.

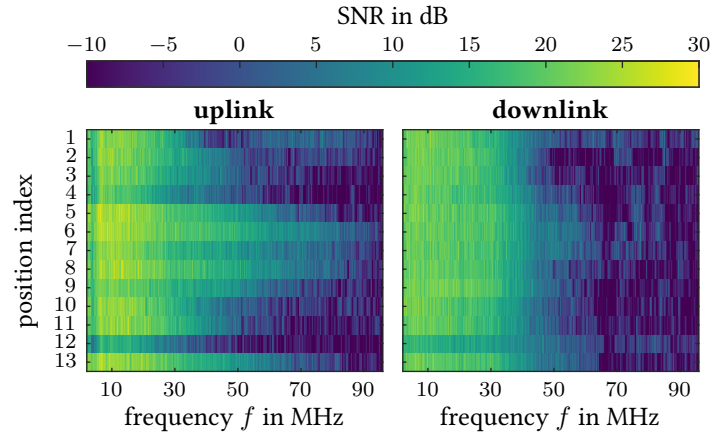


Figure 5.21: SNR per subcarrier as reported by the physical layer of the baseband DSP unit at the 13 measurement points in the UL and DL

for multiple Ethernet line rates and packet sizes. The employed optical front ends were the same as those used in Chapter 3 and had the electrical transmit signal power  $\tilde{P}_{e,t}$  adjusted to avoid Rx circuitry saturation at transmission distances above 0.8 m. The bandwidth of the Tx and Rx front ends was designed to be approximately 50 MHz.

In a first measurement series, the MU highlighted in Fig. 5.19a with a yellow circle, was not yet mounted to the robot, but placed on a tripod at 13 positions around the robot. These are highlighted in Fig. 5.19a with green markers. The resulting ULs and DLs between the MU and the distributed front ends of the AP (highlighted by red circles) were analyzed with respect to SNR and throughput. The SNR per subcarrier, as reported by the physical layer of the DSP baseband unit, is shown in Fig. 5.21 for all 13 positions. Especially in the DL, the targeted bandwidth limitation to 50 MHz is clearly reflected in the SNR values. Furthermore, the gross throughput  $G_{\text{phy,g}}$  of the OWC physical layer and the Ethernet goodput  $G_{\text{gp}}$  are summarized in Table 5.4. The quantity  $G_{\text{phy,g}}$  returned by the commercial chipset is determined by the bits per subcarrier and the fixed OFDM symbol rate. It excludes any overhead of the ITU-T G.hn physical layer and serves as an upper limit for the throughput. It varies with the available SNR per subcarrier and reflects the impact of the optical wireless channel employing antenna diversity. The goodput is defined as

$$G_{\text{gp}} = (1 - \text{PER}) \cdot G_{\text{eth,n}}, \quad (5.10)$$

where  $G_{\text{eth,n}}$  denotes the net Ethernet line rate<sup>10</sup>. While  $G_{\text{eth,n}}$  is generated by the Optixia XM2 independently of the rate supported by the optical wireless channel,  $G_{\text{gp}}$  decreases when packets are not delivered, e.g., due to a saturated OWC link and resulting packet drops at overflowing queues. We may use  $G_{\text{gp}}$  as a figure of merit for the average rate of successfully transmitted Ethernet payload bits. Differences between  $G_{\text{phy,g}}$  and  $G_{\text{gp}}$  are caused, e.g., by training sequences, FEC overhead, packet losses, or

<sup>10</sup> We may differentiate the *net* and *gross* rates with the subscript n and g, respectively. For Ethernet, the *net* line rate excludes the 22 byte (B) header.

Table 5.4: Gross optical wireless physical layer rates and net Ethernet goodput in Mb/s at different positions

pos.	uplink		downlink	
	physical layer	Ethernet	physical layer	Ethernet
1	89	41.5	96	45.8
2	89	41.5	96	45.8
3	100	47.4	95	44.3
4	69	33.5	95	44.5
5	150	50.5	95	50.5
6	150	50.5	95	50.5
7	150	50.5	108	50.5
8	135	50.5	108	50.5
9	95	44.8	108	50.4
10	104	48.4	90	42.7
11	103	48.2	86	43.9
12	44	24	94	45
13	138	50.5	104	50.5

management packets used, e.g., for rate adaptation. Note that the highest tested  $G_{\text{eth},n}$  was 50.5 Mb/s and higher rates are potentially possible.

The results shown Fig. 5.21 and Table 5.4 clearly reflect the non-reciprocity of the OWC system. While in the DL all figures of merit remain mostly steady, the UL shows variations depending on the positions of the MU. The non-reciprocity results not only from unequal HPSAs of TxS and RxS, but also from different numbers of TxS/RxS in the UL and DL. At positions 4 and 12, i.e., those close to the cell boundaries, worst performances were obtained. Positions 5, 6, 7 and 8 happened to be in a well illuminated region of the cell, showing increased SNR and throughputs. Here, the highest gross physical layer and net Ethernet line rates of 150 Mb/s and 50.5 Mb/s were achieved, respectively.

In a second experiment, the support of mobility and large coverage within the manufacturing cell was tested. Therefor the TRxS of the MU was moved by hand while bi-directionally transmitting short Ethernet packets of 64 B at a packet rate of 2 kHz, resulting in a 1.02 Mb/s gross Ethernet rate (0.67 Mb/s net). The resulting 90s long trajectory taken by the MU is highlighted in green in Fig. 5.22a and its start/end point is marked by a yellow *0s*. A sensor logging the acceleration and rotational speed was attached to the MU. These figures are shown in Fig. 5.22b and Fig. 5.22c. The latencies of all successfully received 180000 packets are shown in Fig. 5.22d. The minimum, average and maximum cut-through latencies for the DL are 0.1 ms, 0.4 ms and 162 ms, respectively. For the UL they result in 0.1 ms, 0.33 ms and 95 ms. In both directions, 99% of the latencies were below 1 ms. Peak latencies can be observed for packets transmitted during fast channel changes, i.e., at large accelerations or rotations. The locations of two such exemplary events are highlighted in Fig. 5.22a with yellow *22s* and *72s* and happened at the according times along the path. At the first event, multiple rapid rotations around the Z-axis appear to be the cause of the increased packet latency. At the latter, a rotation around the Y-axis with large translational displacement, followed by two quick rotations around the Z-axis appear to be responsible. Interestingly,

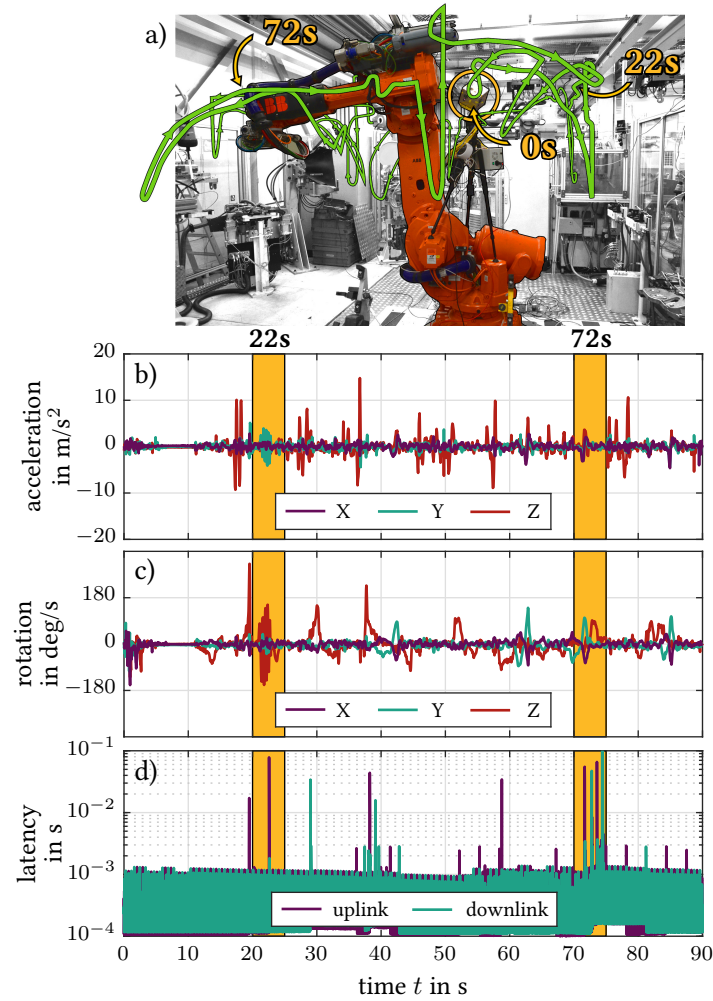


Figure 5.22: a) Photograph of the cell with the trajectory (green line) of the MU (yellow circle) while undergoing slower movements. The yellow 22s/72s indicate two exemplary locations at which transmissions with increased latencies were observed. b) Sensor data of accelerometer. c) Sensor data of gyroscope. d) Latencies per 64B packet along the 90s long trajectory.

larger translational displacements did not appear to have a strong impact, while rapid rotations changed the individual optical wireless channels more significantly.

The fact that PERs of 0 were achieved, i.e., no packets were lost, but merely faced increased latencies, is accredited to the built-in re-transmission mechanism of the rate-adaptive DSP baseband unit. We expect that configuring the baseband unit to operate its physical layer at a more conservative rate or with an increased SNR margin, may slightly increase the average latency, but significantly decrease the peak latencies due to a reduced number of required re-transmissions. This test showed that the designed OWC is capable of maintaining a reliable link in both, UL and DL, while supporting mobility even in the corners of the cell.

The third test series consisted of a real-time video/data transmission from the robot to the infrastructure, while moving at full production speed. For

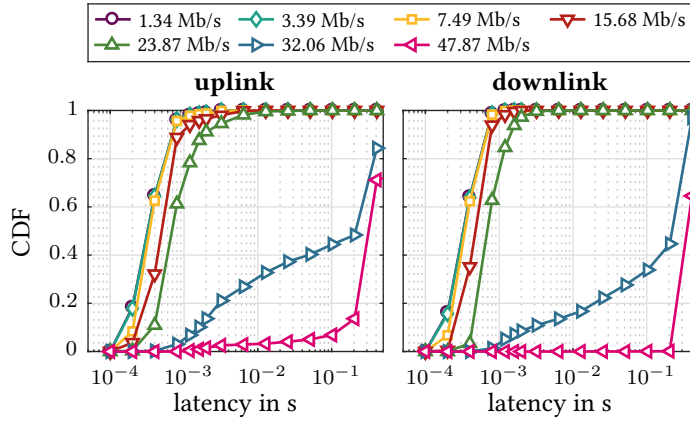


Figure 5.23: Empirical CDFs of latencies for different Ethernet packet sizes and thus different net Ethernet rates measured while the robot was moving at full speed.

this test, the MU was mounted to the robot’s shoulder as highlighted by the yellow circle in Fig. 5.19a. The movements of the robot in this test cell consisted of picking up a grappler, grabbing a car part and moving it to a welding station at the other side of the cell. After the welding process, the part and the grappler were placed back. Subsequently, a mobile welding tool was taken by the robot and different positions of the car part were welded. A total cycle of this manufacturing process took 77s.

For a fixed packet rate of 4000 packets/s, Ethernet packets of 64B, 128B, 256B, 512B, 768B, 1024B and 1518B were transmitted. This resulted in net Ethernet rates  $G_{\text{eth},n}$  of 1.34, 3.39, 7.49, 15.68, 23.87, 32.06 and 47.87 Mb/s, respectively. For each packet size 1,000,000 packets were transmitted over 250s, i.e., approximately 3.5 cycles of the robot. The minimum size for Ethernet packets is 64B, which may be used for packets with high priority as they face smaller network latencies. Large packets are used to obtain higher net rates, as the Ethernet overhead is constantly 22B.

The empirical CDFs of the measured latencies are shown in Fig. 5.23 for both, UL and DL. The reduced latencies for small packets are clearly visible. Latencies start to increase for packets of sizes 512B (15.86 Mb/s) and above. The two largest packet sizes of 1024B (32.06 Mb/s) and 1518B (47.87 Mb/s) faced PERs of 15.6% and 25.6%, respectively, in the UL and 3% and 35.4%, respectively, in the DL. This non-zero PERs resulted from overflowing packet queues in the baseband unit and reveal a saturation of the rate-adaptive physical layer, which did not support such large continuous traffic throughput the entire trajectory. However, for all packet sizes below 768B (23.87 Mb/s) the PER was zero. In case of the two smallest packet sizes, 99% of the packets were delivered within 2 ms in the UL and 1 ms in the DL. In case of the largest error-free packets for 768B, 99% of the packets faced latencies below 10 ms in the UL and 3 ms in the DL.

As a final result, this system allowed for a real-time transmission of a high definition video with MJPEG compression. A camera mounted next to the MU on the robot’s shoulder generated user datagram protocol (UDP) traffic with varying packet sizes and an average Ethernet line rate of 19 Mb/s. The

video was successfully transmitted with low latency while the robot was moving at full speed.

## 5.5 CONCLUSION

In this chapter, a series of transmission experiments over the MIMO OWC channel have been presented. The focus of these experimental investigations lied on how spatial diversity can be exploited and optimized for OWC in order to improve reliability at the physical layer of the communications system.

In a first experiment, it was shown that for broader bandwidths of approximately 100 MHz and resulting data rates between 50 Mb/s and 200 Mb/s, the phase-adjustment of the transmit and receive vectors is an effective way for mitigating self-induced multi-path fading effects. An efficient algorithm for the computation of the transmit and receive vectors, which is also applicable to higher order MIMO channels, was proposed and its functionality verified within this first experiment. However, it was observed that the phase-adjustment can be neglected for narrower bandwidths below 30-50 MHz.

In a second experiment, a narrowband 1 Mb/s transmission was performed in an industrial production environment of a manufacturing cell. For such narrowband transmissions, the use of only the received signal power to calculate the receive vectors was shown to be feasible. Furthermore, the suggested antenna diversity scheme with up to eight Rx's was able to improve coverage from 35% to 80%, when compared to a single Rx setup.

In a third experiment it was demonstrated that the gap to 100% coverage can be closed, even for a real-time transmission of Ethernet packets with a net rate of 23.87 Mb/s. In order to improve coverage, the optical front ends were redesigned to allow for increased optical signal powers at a limited bandwidth of 50 MHz. Furthermore, real-time transmission was enabled by the use of commercially available OFDM baseband DSP units for SISO channels, which required the antenna diversity schemes to be implemented in the electrical analog domain. Note that ideally, combining would be performed in the digital domain, which was not possible due to the use said commercial chipset. However, as a proof-of-concept, these experiments have shown that the exploitation of spatial diversity in OWC is a key building block for a physical layer with high reliability. As a final result, reliable mobile communication over an optical wireless MIMO link faced in a real manufacturing environment could be demonstrated in real-time.

## CONCLUSIONS AND OUTLOOK

---

With a focus on the application of OWC within an industrial production environment, this thesis has discussed the design of a OWC system with high reliability and low latencies. First, causes compromising the reliability of an OWC system were identified: quickly changing channel gains due to fast rotations, high directivity and LOS blockage.

As means of mitigation, the use of non-directed transmission, which smoothes channel gain variations, and the use of multiple Tx/Rxs was suggested and experimentally investigated. The reduced received optical signal powers and thus poor SNRs associated with this approach was successfully overcome by using higher modulation indices. The impact of resulting nonlinear distortions was investigated and a receive-side, Volterra series based nonlinear equalization scheme suggested, whose gains of up to 2 dB were demonstrated experimentally. For joint mitigation of LOS blocking and reduced received signal powers, the exploitation of spatial diversity was investigated. As an initial step, the first optical wireless MIMO channel measurements in a real manufacturing environment were performed and presented in this thesis. The expected strong spatial dependence with sudden variations of 10-20 dB in received signal power due to LOS blocking and fast rotations was verified. This led to a thorough analysis of how antenna diversity schemes for broad- and narrowband signaling can be optimized for OWC. These results in turn motivated the design of a first reliable real-time OWC system that employs antenna diversity schemes implemented in the analog electrical domain. This system was deployed in a real manufacturing environment and its suitability for industrial wireless communication demonstrated. With all its in-between steps, this thesis has shown how to design and operate a real-time OWC system usable in an industrial production environment. The derived concepts are, however, not limited to the field of industrial wireless communication and may also be applied to less demanding environments such as wireless indoor home or office networks, where the experience of mobility is crucial.

As for possible improvements, it is noteworthy that combining in the analog domain is sub-optimal. Thus, first extensions of this system would include moving the application of antenna diversity schemes to the digital domain. This would allow to make use of the improved calculation and application of transmit/receive vectors suggested in this thesis, when moving to higher bandwidth transmissions. Additionally, an extension of the Rx front ends by an automatic gain control (AGC) between the PD and residual Rx circuitry would improve the range of feasible transmission distances. With this capability added, the implementation of the suggested nonlinear post-equalizer (NLPE) in real-time is a suitable step for further improvement of the signal quality.

Apart from the improving modifications already investigated in parts within this thesis, further extensions are possible. Overall, it is reasonable to focus the next steps on scaling the communication system to larger areas and

the support of multiple users. While the presented real-time communication system supports multiple users via time division multiple access (TDMA) coordinated in the ITU-T G.hn chipsets [142], an efficient multi-user coordination would be an interesting addition. This could, e.g., allow for efficient spatial reuse via a combination of TDMA and spatial division multiple access (SDMA), which is crucial for the support of multiple users without significantly decreasing the per-user data rates. This would require a multi-user MIMO channel estimation, which ideally probes the optical wireless channel at sub-millisecond intervals in order to track the fast channel changes. Furthermore, miniaturization and a light-weight design of the MU front ends with lower power consumption would open new applications for highly mobile units, such as handheld devices or drones, which are envisioned in the factories of the future.

## APPENDIX

## A.1 NOISE FLOORS

To test the type of limitation in our transceivers (TRxs), the noise floor was measured under multiple conditions:

<i>normal</i>	artificial (fluorescent) and natural light through the window of the well illuminated laboratory
<i>dark</i>	fully darkened laboratory
<i>own Tx blocked</i>	as a potential source of shot noise, the LED of the TRx fully blocked
<i>outside</i>	TRx is pointed outside the window towards the sky on a cloudy day to gather diffuse sunlight
<i>alien Tx</i>	same as <i>normal</i> , but a second TRx positioned at a distance of 1.5 m additionally illuminates the Rx

The resulting spectra are shown in Fig. A.1. Since darkening the laboratory had no impact on the noise spectrum, we may conclude that the noise was not dominated by shot noise of ambient light sources. The peculiar looking spectral lines at lower frequencies disappeared when blocking the LED of the own transmitter (Tx) circuitry and increased when a second TRx was added. Without knowing the exact reason at the time of writing this manuscript, a

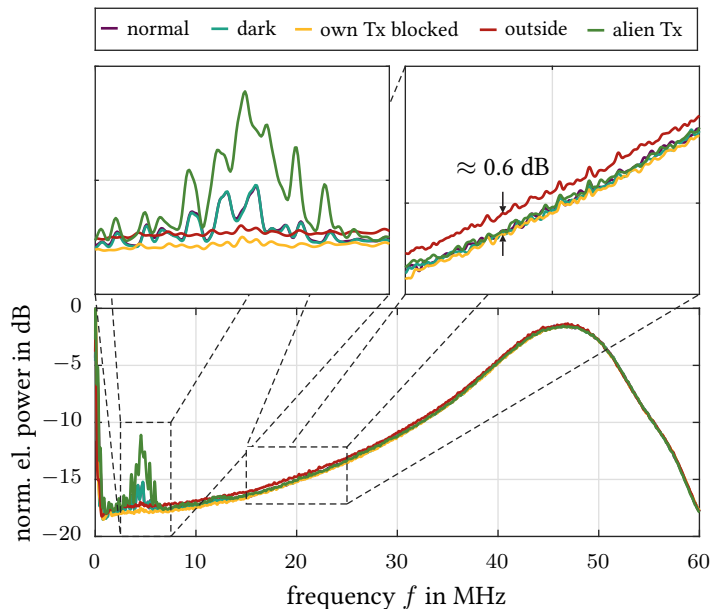


Figure A.1: Measured noise floors of our Rxs with dominant thermal noise. The noise was measured with a resolution bandwidth of 100 kHz under varying conditions.

probable cause may be the coupling of imperfection from the power supply into the Tx circuitry, which are modulated onto the optical power and picked up by the photodiode (PD). Holding the TRx with the blocked LED towards the bright sky increased the noise floor by approximately 0.6 dB at lower to intermediate frequencies. Such an increase indicates that the shot noise power inflicted by the natural light source was still only  $\frac{1}{10^{0.6}} = 6.75$  times weaker than the other noise source. A possible noise source independent of the incident optical power and one which shows a frequency dependent increasing power would be thermal noise from the Rx components [2], [143].

## A.2 RADIO- AND PHOTOMETRIC QUANTITIES

The fields of radiometry and photometry both involve the quantitative measurement of electromagnetic radiation power, with the difference that in photometry powers are considered as perceived by the human eye. Therefore, every quantity in radiometry has a corresponding one in photometry, which is obtained by weighting it with a luminosity function that models the human eye's spectrally depending sensitivity. Table A.1 summarizes some of such quantities. Those considered elsewhere in the thesis, have a symbol in the first column.

Table A.1: Radiometric quantities and their photometric equivalents.

	radiometry	units	photometry	units
$E$	radiant energy	J, eV, W · s	luminous energy	lm · s
$P$	radiant flux or power	W, J/s	luminous flux or power	lm, cd · sr
$R$	radiant intensity	W/sr	luminous intensity	cd, lm/sr
$I$	irradiance/ radiosity/ radiant exitance	W/m <sup>2</sup>	illuminance/ luminosity/ luminous exitance	lx, lm/m <sup>2</sup>
-	radiance	W/m <sup>2</sup> /sr	luminance	cd/m <sup>2</sup>

The unabbreviated units are joule (J), watt (W), second (s), steradian (sr), meter (m), lumen (lm), candela (cd), and lux (lx). Sometimes the units of luminance is called nit. Note the slight differences between irradiance, radiant exitance and radiosity: while radiosity describes the radiant power per unit area *leaving* a surface via emission, transmission or reflection, radiant exitance is the radiant power per unit area *emitted* by a surface. To add further to the confusion, the term irradiance describes the radiant power per unit area *incident upon* a surface.

Interestingly, the eye's spectral sensitivity varies with the surrounding lighting conditions. For this reason, the Commission International de l'Éclairage (CIE) has adopted luminous functions for *photopic* (daylight) and *scotopic* vision (darkness), which are made publicly available by the Colour and Vision Research Laboratory at University College London [144] and listed in [71].

## A.3 PHASE OPTIMIZATION FOR EQUAL GAIN TRANSMISSION

The cost function of the equal gain transmission (EGT)+equal gain combining (EGC) phase optimization problem may be written as:

$$\begin{aligned} J(\boldsymbol{\rho}, \boldsymbol{\psi}) &= |H_{\text{eff}}|^2 \\ &= \left| \sum_{m=1}^M \sum_{n=1}^N e^{j\rho_n} e^{j\psi_m} H_{mn} \right|^2 \\ &= \left( \sum_{m=1}^M \sum_{n=1}^N e^{j\rho_n} e^{j\psi_m} H_{mn} \right) \left( \sum_{m=1}^M \sum_{n=1}^N e^{-j\rho_n} e^{-j\psi_m} H_{mn}^* \right) \end{aligned} \quad (\text{A.1})$$

Many of the conventional, general purpose nonlinear optimization algorithms rely on a search along the cost function  $J(\boldsymbol{\rho}, \boldsymbol{\psi})$ , for which its gradient and Hessian matrix are often required. We derive both of them, so that they can be fed to such nonlinear optimization algorithms. To put the entries of the nabla operator into a fixed order, we define the gradient as follows:

$$\nabla J(\boldsymbol{\rho}, \boldsymbol{\psi}) = \left[ \frac{\partial}{\partial \rho_1}, \dots, \frac{\partial}{\partial \rho_N}, \dots, \frac{\partial}{\partial \psi_1}, \dots, \frac{\partial}{\partial \psi_M} \right]^\top J(\boldsymbol{\rho}, \boldsymbol{\psi}) \quad (\text{A.2})$$

The entries of the gradient of  $\nabla J(\boldsymbol{\rho}, \boldsymbol{\psi})$  when taken with respect to the  $n'$ -th entry of the transmit phase vector  $\boldsymbol{\rho}$  are then

$$\begin{aligned} &\frac{\partial}{\partial \rho_{n'}} J(\boldsymbol{\rho}, \boldsymbol{\psi}) \\ &= -2 \operatorname{Im} \left\{ \left( \sum_{m=1}^M e^{j\psi_m} e^{j\rho_{n'}} H_{mn'} \right) \left( \sum_{m=1}^M \sum_{n=1}^N e^{-j\psi_m} e^{-j\rho_n} H_{mn}^* \right) \right\}. \end{aligned} \quad (\text{A.3})$$

Equivalently, for the  $m'$ -th entry of the receive phase vector  $\boldsymbol{\psi}$  we get

$$\begin{aligned} &\frac{\partial}{\partial \psi_{m'}} J(\boldsymbol{\rho}, \boldsymbol{\psi}) \\ &= -2 \operatorname{Im} \left\{ \left( \sum_{n=1}^N e^{j\psi_{m'}} e^{j\rho_n} H_{m'n} \right) \left( \sum_{m=1}^M \sum_{n=1}^N e^{-j\psi_m} e^{-j\rho_n} H_{mn}^* \right) \right\}. \end{aligned} \quad (\text{A.4})$$

The Hessian matrix, while simple to derive, is a little more tedious to write down, since we have a few cases to differentiate. Since we see both, the entries of the transmit and receive phase vectors  $\boldsymbol{\rho}$  and  $\boldsymbol{\psi}$  as the optimization variables, the Hessian matrix  $\mathbf{H}_H$  can be split into four parts:

$$\mathbf{H}_H = \begin{bmatrix} \frac{\partial^2}{\partial \rho_1 \partial \rho_1} & \cdots & \frac{\partial^2}{\partial \rho_1 \partial \rho_N} & \frac{\partial^2}{\partial \rho_1 \partial \psi_1} & \cdots & \frac{\partial^2}{\partial \rho_1 \partial \psi_M} \\ \vdots & \ddots & \vdots & \vdots & \ddots & \vdots \\ \frac{\partial^2}{\partial \rho_N \partial \rho_1} & \cdots & \frac{\partial^2}{\partial \rho_N \partial \rho_N} & \frac{\partial^2}{\partial \rho_N \partial \psi_1} & \cdots & \frac{\partial^2}{\partial \rho_N \partial \psi_M} \\ \frac{\partial^2}{\partial \psi_1 \partial \rho_1} & \cdots & \frac{\partial^2}{\partial \psi_1 \partial \rho_N} & \frac{\partial^2}{\partial \psi_1 \partial \psi_1} & \cdots & \frac{\partial^2}{\partial \psi_1 \partial \psi_M} \\ \vdots & \ddots & \vdots & \vdots & \ddots & \vdots \\ \frac{\partial^2}{\partial \psi_M \partial \rho_1} & \cdots & \frac{\partial^2}{\partial \psi_M \partial \rho_N} & \frac{\partial^2}{\partial \psi_M \partial \psi_1} & \cdots & \frac{\partial^2}{\partial \psi_M \partial \psi_M} \end{bmatrix} \quad (\text{A.5})$$

We are thus taking two partial derivatives, first with respect to either the  $n'$ -th or  $m'$ -th entry of  $\boldsymbol{\rho}$  or  $\boldsymbol{\psi}$ , respectively, then with respect to the  $n''$ -th or  $m''$ -th entry. The entries of  $\mathbf{H}_H$  can be computed by splitting them into the following cases.

Case 1,  $n' = n''$ :

$$\begin{aligned} & \frac{\partial^2}{\partial \rho_{n'} \partial \rho_{n''}} J(\boldsymbol{\rho}, \boldsymbol{\psi}) \\ &= -2 \operatorname{Re} \left\{ \left( \sum_{m=1}^M e^{j\psi_m} e^{j\rho_{n'}} H_{mn'} \right) \left( \sum_{\substack{n=1, \\ n \neq n'}}^N \sum_{m=1}^M e^{-j\psi_m} e^{-j\rho_n} H_{mn}^* \right) \right\} \quad (\text{A.6}) \end{aligned}$$

Case 2,  $n' \neq n''$ :

$$\begin{aligned} & \frac{\partial^2}{\partial \rho_{n'} \partial \rho_{n''}} J(\boldsymbol{\rho}, \boldsymbol{\psi}) \\ &= 2 \operatorname{Re} \left\{ \left( \sum_{m=1}^M e^{j\psi_m} e^{j\rho_{n'}} H_{mn'} \right) \left( \sum_{m=1}^M e^{-j\psi_m} e^{-j\rho_{n''}} H_{mn''}^* \right) \right\} \quad (\text{A.7}) \end{aligned}$$

Case 3,  $m' = m''$ :

$$\begin{aligned} & \frac{\partial^2}{\partial \rho_{m'} \partial \rho_{m''}} J(\boldsymbol{\rho}, \boldsymbol{\psi}) \\ &= -2 \operatorname{Re} \left\{ \left( \sum_{m=1}^M e^{j\psi_{m'}} e^{j\rho_n} H_{m'n} \right) \left( \sum_{\substack{m=1, \\ m \neq m'}}^M \sum_{n=1}^N e^{-j\psi_m} e^{-j\rho_n} H_{mn}^* \right) \right\} \quad (\text{A.8}) \end{aligned}$$

Case 4,  $m' \neq m''$ :

$$\begin{aligned} & \frac{\partial^2}{\partial \rho_{m'} \partial \rho_{m''}} J(\boldsymbol{\rho}, \boldsymbol{\psi}) \\ &= 2 \operatorname{Re} \left\{ \left( \sum_{n=1}^N e^{j\psi_{m'}} e^{j\rho_n} H_{m'n} \right) \left( \sum_{n=1}^N e^{-j\psi_{m''}} e^{-j\rho_n} H_{m''n}^* \right) \right\} \quad (\text{A.9}) \end{aligned}$$

Case 5, otherwise:

$$\begin{aligned} & \frac{\partial^2}{\partial \rho_{n'} \partial \rho_{m'}} J(\boldsymbol{\rho}, \boldsymbol{\psi}) \\ &= -2 \operatorname{Re} \left\{ e^{j\psi_{m'}} e^{j\rho_{n'}} h_{m'n'} \left( \sum_{n=1}^N \sum_{m=1}^M e^{-j\psi_m} e^{-j\rho_n} H_{mn}^* \right) \right. \\ & \quad \left. - \left( \sum_{n=1}^N \sum_{m=1}^M e^{j\rho_{m'}} e^{-j\psi_{n'}} e^{j\psi_n} e^{-j\psi_m} H_{m'n} H_{mn}^* \right) \right\} \quad (\text{A.10}) \end{aligned}$$

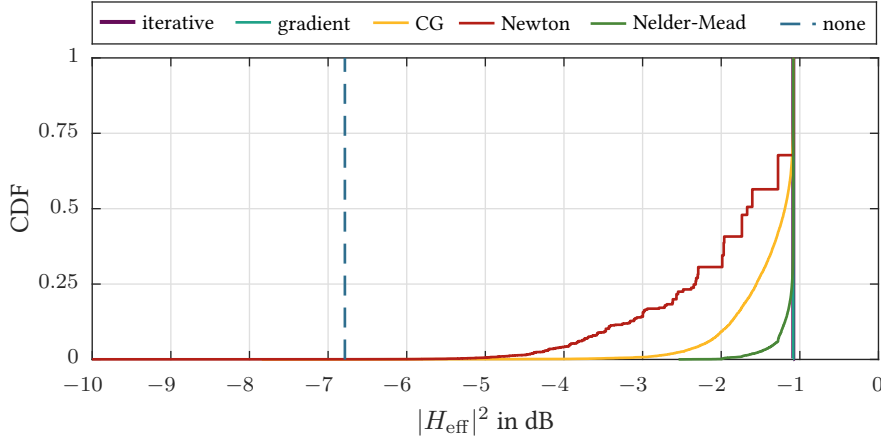


Figure A.2: Empirical CDFs of resulting effective channel gains after the convergence of different nonlinear optimization algorithms. The outcomes vary due to varying initialization points. The suggested iterative optimization (purple) and the simple gradient search (turquoise) always converge to the largest gain of 1.08 dB obtained among all optimization schemes.

In the last case we first take the derivative with respect to the  $n'$ -th entry of  $\boldsymbol{\rho}$  and then with respect to the  $m'$ -th entry of  $\boldsymbol{\psi}$ . In all cases, the order of differentiation does not matter since the all partial derivatives are continuous (Schwarz's theorem).

Equations (A.1) to (A.10) are the basis for multiple unconstrained nonlinear optimization solving algorithms. As benchmarks, we will be applying a simple gradient search and a conjugate gradient (CG) search by Fletcher and Reeves [136], [137]. Both these methods rely on Eqs. (A.1) to (A.4) only. Further, we apply Newton's method [136], which approximates the cost function with a quadratic function via a truncated Taylor series. Thus, the Hessian matrix and all Eqs. (A.1) to (A.10) are employed by this method. The last method is a simplex method<sup>1</sup> by Nelder and Mead, which does not require the computation of derivatives and relies fully on Eq. (A.1) only [145], [146]. It is also the workhorse behind MATLAB's `fminsearch` function. Its approach is fundamentally different, which is why it serves as an additional benchmark to the check against in case derivative-based methods fail.

In order to see how well the suggested iterative optimization presented in Section 5.2.1 performs compared to general purpose algorithms, we solve an optimization problem for a fixed channel starting from 10000 different, randomly selected initial guesses  $\boldsymbol{\rho}_0$  and  $\boldsymbol{\psi}_0$ . The initial guesses may have a strong impact on the outcome of the optimization problem, since Eq. (A.1) is neither convex nor concave and we do thus have to assume that multiple local maxima exist to which the solution may converge. The channel used for testing is highlighted in Fig. 5.4 (41.7 MHz). It was chosen because coefficients are not aligned, but scattered in the angular space. This suggest a more difficult problem to solve, since the target of are fully aligned pha-

<sup>1</sup> It is not to be confused with simplex methods from linear programming. Here, the name results from the higher dimensional simplex, which is the convex hull at whose edge nodes the cost function is evaluated. Details are out of scope of this thesis, but are well described in [137], [145], [146].

sors differs strongly from the initial state. Figure A.2 shows the empirical cumulative distribution functions (CDFs) of the resulting scalar effective channels  $|H_{\text{eff}}|^2$  after each algorithm is converged. Since the channel is normalized such that  $\sum_{n=1}^N \sum_{m=1}^M |H_{nm}| = 1$ , an upper limit of  $|H_{\text{eff}}|^2$  is 0 dB. The dashed blue line shows the effective channel gain, when  $\boldsymbol{\rho} = \boldsymbol{\psi} = \mathbf{0}$  and thus no phase adjustment is performed. Its magnitude is thus given by  $\left| \sum_{n=1}^N \sum_{m=1}^M H_{nm} \right|^2 \approx 0.21$ , which corresponds to -6.79 dB. The suggested iterative optimization and simple gradient method perform best and always converge to the best result of -1.08 dB, thus improving the channel gain by 5.76 dB. In 68%, 51%, and 13% of the initializations, the CG, Newton and Nelder-Mead methods converge to solutions 0.1 dB worse than the optimum. In rare cases, the CG and Newton method converge to solutions worse than for  $\boldsymbol{\rho} = \boldsymbol{\psi} = \mathbf{0}$ . The reason for the poor performance of these two methods is likely due to the non-quadratic nature of Eq. (A.1). Both methods are optimized to have improved convergence when applied to quadratic problems. In unconstrained nonlinear optimization it is often assumed that the cost function can be approximated as a quadratic function around a local/global maximum. Thus, when already close to the optimum, the CG and Newton's method are expected to have faster convergence, but fail in cases where this assumption is wrong.

We now investigate the convergence behavior of two initial guesses  $\boldsymbol{\rho}_0$  and  $\boldsymbol{\psi}_0$  that are of particular interest. Since the overall goal of this optimization is to improve the performance compared to the simple unmatched case, a reasonable initialization is  $\boldsymbol{\rho}_0 = \boldsymbol{\psi}_0 = \mathbf{0}$ , which corresponds to performing no phase matching. The convergence for the exemplary channel under discussion is shown in the left graph of Fig. A.3. All optimization algorithms start off at the unmatched case, quickly improving the channel gain after only a few iterations<sup>2</sup>. We may observe that for this particular initialization, Newton's method and the Nelder-Mead method do not converge to the optimum and the CG method does so only slowly. However, looking at the second particularly interesting initialization, the convergence behaves differently. We recall, that the channel under investigation is a measured multiple-input multiple-output (MIMO) channel estimated at  $i$ -th frequency channel of  $f_i = 41.7$  MHz and thus all quantities in this section are in fact frequency-dependent quantities. For the given digital signal processing (DSP), the channel at the next lower frequency was estimated at  $f_{i-1} = 41.5$  MHz. Expecting the solutions of neighboring frequency channels to be similar, we set the initialization to  $\boldsymbol{\rho}_0(f_i) = \boldsymbol{\rho}^*(f_{i-1})$  and  $\boldsymbol{\psi}_0(f_i) = \boldsymbol{\psi}^*(f_{i-1})$ . For such initialization, the right graphs of Fig. A.3 show the convergence. The small change in  $|H_{\text{eff}}|^2$  and the little number of iterations required to achieve convergence indicate that indeed the optimum is shifted only slightly. The inset shows an enlarged version of the convergence within the first 10 iterations. Being close to the local optimum, the Newton's method and the CG method now show improved convergence over the simple gradient method. However, the suggested iterative optimization continues to quickly

<sup>2</sup> While the steps within each iterations of the gradient, CG and Newton's method are quite similar, they are not comparable to the other ones. Since the Nelder-Mead method takes  $>100$  iterations to converge, only the final result is shown.

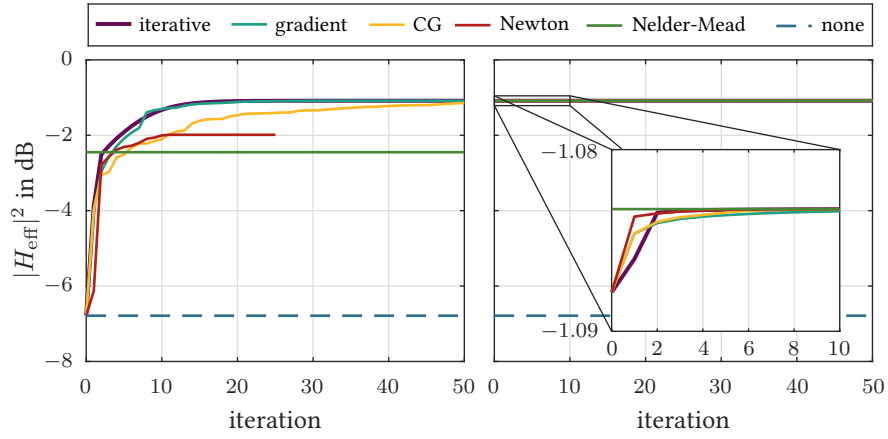


Figure A.3: Convergence behavior of multiple nonlinear optimization algorithms. The left plot shows the convergence, when  $\rho_0(f_i) = \psi_0(f_i) = \mathbf{0}$  is chosen for initialization. The right graph shows the convergence, when the nonlinear optimization algorithms are initialized with the result of the neighboring frequency, i.e.,  $\rho_0(f_i) = \rho^*(f_{i-1})$  and  $\psi_0(f_i) = \psi^*(f_{i-1})$ .

find the new optimum within two iterations. Since  $\rho$  and  $\psi$  need to be updated, two iterations are always required.



## LIST OF ACRONYMS

---

$\mu$ C	<u>micro</u> <u>controller</u>
$\mu$ LED	<u>micro</u> <u>light-emitting diode</u>
AC	<u>alternating</u> <u>current</u>
ACO	<u>asymmetrically</u> <u>clipped</u> <u>optical</u>
ADC	<u>analog-to-digital</u> <u>converter</u>
AGC	<u>automatic</u> <u>gain</u> <u>control</u>
AP	<u>access</u> <u>point</u>
APD	<u>avalanche</u> <u>photodiode</u>
ARQ	<u>automatic</u> <u>repeat</u> <u>request</u>
B	<u>byte</u>
BER	<u>bit</u> <u>error</u> <u>rate</u>
BLER	<u>block</u> <u>error</u> <u>rate</u>
BPL	<u>bit</u> and <u>power</u> <u>loading</u>
BPSK	<u>binary</u> <u>phase-shift</u> <u>keying</u>
BW	<u>bandwidth</u>
CAD	<u>computer</u> <u>aided</u> <u>design</u>
CAP	<u>carrier-less</u> <u>amplitude/phase</u> <u>modulation</u>
CAZAC	<u>constant-amplitude</u> <u>zero-auto</u> <u>correlation</u>
CCDF	<u>complementary</u> <u>cumulative</u> <u>distribution</u> <u>function</u>
CDF	<u>cumulative</u> <u>distribution</u> <u>function</u>
CG	<u>conjugate</u> <u>gradient</u>
CIE	<u>Com</u> <u>mission</u> <u>I</u> <u>nternational</u> <u>d</u> <u>e</u> <u>l'</u> <u>E</u> <u>clairage</u>
CIR	<u>channel</u> <u>impulse</u> <u>response</u>
CP	<u>cyclic</u> <u>prefix</u>
CSI	<u>channel</u> <u>state</u> <u>information</u>
DAC	<u>digital-to-analog</u> <u>converter</u>
DC	<u>direct-current</u>
DCO	<u>direct-current</u> <u>biased</u> <u>optical</u>
DD	<u>direct</u> <u>detection</u>
DFT	<u>discrete</u> <u>Fourier</u> <u>transform</u>
DL	<u>downlink</u>
DSP	<u>digital</u> <u>signal</u> <u>processing</u>
DVB-T	<u>D</u> <u>igital</u> <u>V</u> <u>ideo</u> <u>B</u> <u>roadcasting</u> - <u>T</u> <u>errestrial</u>
E/O	<u>electro-optical</u>
EGC	<u>equal</u> <u>gain</u> <u>combining</u>
EGT	<u>equal</u> <u>gain</u> <u>transmission</u>
eU	<u>enhanced</u> <u>unipolar</u>

EVM	<u>e</u> rror- <u>v</u> ector <u>m</u> agnitude
FEC	<u>f</u> orward <u>e</u> rror <u>c</u> orrection
FFT	<u>f</u> ast <u>F</u> ourier <u>t</u> ransform
FOV	<u>f</u> ield- <u>o</u> f- <u>v</u> iew
FS	<u>f</u> raming <u>s</u> equence
HHI	Fraunhofer <u>H</u> einrich <u>H</u> ertz <u>I</u> nstitute
HPSA	<u>h</u> alf- <u>p</u> ower <u>s</u> emi- <u>a</u> ngle
iDFT	<u>i</u> nverse <u>d</u> iscrete <u>F</u> ourier <u>t</u> ransform
IEC	<u>I</u> nternational <u>E</u> lectrotechnical <u>C</u> ommission
IEEE	<u>I</u> nstitute of <u>E</u> lectrical and <u>E</u> lectronics <u>E</u> ngineers
IM	<u>i</u> ntensity <u>m</u> odulation
IoT	<u>I</u> nternet of <u>T</u> hings
IR	<u>i</u> nfrared
ISI	<u>i</u> nter-symbol <u>i</u> nterference
ISM	<u>i</u> ndustrial, <u>s</u> cientific and <u>m</u> edical
ITU-T	<u>I</u> nternational <u>T</u> elecommunications <u>U</u> nion - Standardization Sector
IWC	<u>i</u> nfrared <u>w</u> ireless <u>c</u> ommunication
LD	<u>l</u> aser <u>d</u> iode
LDPC	<u>l</u> ow- <u>d</u> ensity <u>p</u> arity- <u>c</u> heck
LED	<u>l</u> ight- <u>e</u> mitting <u>d</u> iode
LLR	<u>l</u> og- <u>l</u> ikelihood <u>r</u> atio
LOS	<u>l</u> ine- <u>o</u> f- <u>s</u> ight
LS	<u>l</u> east <u>s</u> quares
LTE	<u>l</u> ong <u>t</u> erm <u>e</u> volution
LUT	<u>l</u> ook- <u>u</u> p- <u>t</u> able
MAC	<u>m</u> edium <u>a</u> ccess <u>c</u> ontrol
MIMO	<u>m</u> ultiple- <u>i</u> nput <u>m</u> ultiple- <u>o</u> utput
MMSE	<u>m</u> inimum <u>m</u> ean <u>s</u> quare <u>e</u> rror
MRC	<u>m</u> aximum <u>r</u> atio <u>c</u> ombining
MRT	<u>m</u> aximum <u>r</u> atio <u>t</u> ransmission
MU	<u>m</u> obile <u>u</u> nit
nLOS	<u>n</u> on- <u>l</u> ine- <u>o</u> f- <u>s</u> ight
NLPE	<u>n</u> onlinear <u>p</u> ost- <u>e</u> qualizer
NLTS	<u>n</u> onlinear <u>t</u> raining <u>s</u> equence
O/E	<u>o</u> pto- <u>e</u> lectrical
OFDM	<u>o</u> rthogonal <u>f</u> requency- <u>d</u> ivision <u>m</u> ultiplexing
OH	<u>o</u> verhead
OOK	<u>o</u> n/ <u>o</u> ff <u>k</u> eysing
OWC	<u>o</u> ptical <u>w</u> ireless <u>c</u> ommunication
P2P	<u>p</u> oint- <u>t</u> o- <u>p</u> oint

PAPR	<u>peak-to-average power ratio</u>
PD	<u>photodiode</u>
pdf	<u>probability density function</u>
PDV	<u>packet delay variation</u>
PER	<u>packet error rate</u>
PIN	<u>positive intrinsic negative</u>
PLC	<u>powerline communication</u>
PLS	<u>penalized least squares</u>
PRBS	<u>pseudo-random bit sequence</u>
PS	<u>pulse shape</u>
QAM	<u>quadrature amplitude modulation</u>
QPSK	<u>quadrature phase-shift keying</u>
RF	<u>radio frequency</u>
RGB	<u>red-green-blue</u>
RGBY	<u>red-green-blue-yellow</u>
RRC	<u>root-raised-cosine</u>
Rx	<u>receiver</u>
SC	<u>single-carrier</u>
SDMA	<u>spatial division multiple access</u>
SFN	<u>single frequency network</u>
Si	<u>silicon</u>
SIMO	<u>single-input multiple-output</u>
SISO	<u>single-input single-output</u>
SLC	<u>selection combining</u>
SNR	<u>signal-to-noise ratio</u>
SP	<u>serial-to-parallel</u>
TDMA	<u>time division multiple access</u>
TIA	<u>trans-impedance amplifier</u>
TRx	<u>transceiver</u>
TS	<u>training sequence</u>
Tx	<u>transmitter</u>
U	<u>unipolar</u>
UDP	<u>user datagram protocol</u>
UL	<u>uplink</u>
VLC	<u>visible light communication</u>
WDM	<u>wavelength-division multiplexing</u>
WLAN	<u>wireless local area network</u>
ZF	<u>zero-forcing</u>



## LIST OF SYMBOLS

---

The notation in this thesis follows a few rules of thumb. While it was not always possible to strictly enforce them, they are as follows: Italic, non-bold symbols in latin or greek letters indicate variable quantities. Non-italic, non-bold symbols indicate non-variable quantities such as constants and annotations. Lowercase, bold symbols in latin or greek letters indicate vectors. Uppercase, bold symbols indicate matrices. Parentheses are used for continuous-time/-frequency signals. Brackets are used for discrete-time/-frequency signals.

Symbol	Description	Unit
$A$	area of a surface	$\text{m}^2$
$A_{\text{eff}}$	effective area of a surface	$\text{m}^2$
$\alpha$	relative magnitude between a line-of-sight and non-line-of-sight component	-
$ \cdot $	denotes the magnitude operator, which returns the absolute value of a complex number	-
$\angle(\cdot)$	denotes the angle operator, which returns the phase of a complex	rad
$B$	bandwidth of a bandwidth-limited signal or system	Hz
$\beta$	roll-off of a (root-)raised cosine pulse shape	-
$c$	speed of light in vacuum: 299, 792, 458 m/s	m/s
$d$	distance	m
$\Delta d$	difference in distances	m
$d[k]$	distorted signal in discrete time-domain	-
$d_{\text{nl}}[k]$	purely nonlinear part of the distorted signal in discrete time-domain	-
$D[l]$	distorted signal in discrete frequency-domain	-
$D_{\text{nl}}[l]$	purely nonlinear part of the distorted signal in discrete frequency-domain	-
$\delta(t)$	Dirac delta function	-
$e$	base of natural logarithm, sometimes called Euler's number. Approximately 2.718281828	-
$E$	radiant or optical energy	J
$\ \cdot\ _2$	Euclidean norm of a vector	-
$f$	continuous frequency index	Hz
$f_c$	electrically or digitally generated intermediate carrier frequency	Hz

Symbol	Description	Unit
$f_{n,i}$	frequency of $i$ -th sinusoid transmitted by the $n$ -th transmitter	Hz
$\phi$	azimuth angle	rad
$G(\theta)$	optical gain of a lens	-
$G_{\text{eth,g}}$	gross Ethernet throughput	b/s
$G_{\text{eth,n}}$	net Ethernet throughput	b/s
$G_{\text{gp}}$	gootput of the end-to-end Ethernet link	b/s
$G_{\text{phy,g}}$	gross physical layer throughput	b/s
$G_{\text{phy,n}}$	net physical layer throughput	b/s
$h(t)$	continuous-time channel impulse response	-
$h[k]$	discrete-time channel impulse response	-
$h$	Planck's constant: $6.626070150 \cdot 10^{-34}$ Js	Js
$H[l]$	channel frequency response in discrete frequency-domain. To indicate the correspondence to a physical frequency $f$ the notation $H[f]$ will sometimes be used.	-
$\mathbf{H}$	frequency dependent multiple-input multiple-output channel matrix	-
$H_{\text{eff}}$	scalar, frequency dependent effective single-input single-output channel coefficient	-
$I$	irradiance	W/m <sup>2</sup>
$j$	imaginary number	-
$J$	penalizing function of the peanlized least-squares estimation	-
$k$	discrete time index	-
$K$	order of Lambertian function	-
$\kappa$	shift of discrete time index	-
$l$	discrete frequency index	-
$L^{(K)}(\theta)$	Lambertian function of order $K$	-
$\lambda_{\text{ph}}$	wavelength ascribed to a photon	m
$\lambda$	regularition parameter for the penalized least-squares estimation	-
$m$	number of receiver when only a subset of $M$ receiver is used	-
$m$	denotes the $m$ -th receiver	-
$m_q$	memory in samples of $q$ -th Volterra kernel	-
$M$	number of receivers	-
$\mathcal{M}$	cardinality of a constellation	-
$\mu$	modulation index of a light-emitting diode	-

Symbol	Description	Unit
$n$	number of transmitters when only a subset of $N$ transmitters is used	-
$\mathbf{n}$	vector whose elements are the samples of a noise signal in discrete time-domain	-
$n$	denotes the $n$ -th transmitter	-
$n_a$	refractive index of surrounding environment, e.g. air	-
$n_l$	refractive index of a lens' material	-
$n(t)$	noise signal in continuous time-domain	-
$n[k]$	noise signal in discrete time-domain	-
$\mathbf{N}$	vector whose elements are the samples of a noise signal in discrete frequency-domain	-
$N$	number of transmitters	-
$N_c$	number of distinct coefficients in a Volterra kernel	-
$N_{CP}$	size of the cyclic prefix	-
$N_{DFT}$	size of the discrete Fourier transform	-
$N_{FFT}$	size of the fast Fourier transform	-
$N_{IR}$	memory of an impulse response in samples	-
$N(f)$	noise signal in continuous frequency-domain	-
$N[l]$	noise signal in discrete frequency-domain	-
$N_s$	number of distinct sinusoids used to estimate the frequency response of a channel	-
$\Omega$	solid angle	sr
$\mathbf{p}$	weighting vector at the transmitter	-
ph	denotes correspondence to a photon	-
$p_n$	$n$ -th entry of the transmit vector $\mathbf{p}$	-
$P_e$	electrical power	W
$\tilde{P}_e(t)$	time-varying electrical power	W
$\overline{P}_e$	average electrical power	W
$P$	radiant or optical power	W
$\tilde{P}(t)$	time-varying optical power	W
$\overline{P}$	average optical power	W
$\pi$	mathematical constant, sometimes called Archimedes' constant. Approximately 3.14519265	-
$\psi_m$	phase angle of the $m$ -th entry of the receive vector $\mathbf{q}$	rad
$\boldsymbol{\psi}$	receive phase vector, whose entries are $\psi_m$	rad
$\mathbf{q}$	weighting vector at the receiver	-
$q_m$	$m$ -th entry of the receive vector $\mathbf{q}$	-
$q$	order of an individual Volterra operator	-
$Q$	highest order of a Volterra series	-
r	denotes correspondence to a receiver	-

Symbol	Description	Unit
$\mathcal{R}$	matrix whose eigenvectors span the subspace to the penalized in the penalized least-squares estimation	-
$R(\theta)$	radiant intensity	W/sr
$R_{\text{FEC}}$	rate of the forward error-correction	-
$R_s$	sampling rate	Hz
$R_{\text{sy}}$	symbol rate	Bd
$\rho_n$	phase angle of the $n$ -th entry of the transmit vector $\mathbf{p}$	rad
$\boldsymbol{\rho}$	transmit phase vector, whose entries are $\rho_n$	rad
$\square_W$	rectangular function of width $W$	-
$\mathcal{S}$	subset of subcarriers used in a simulation or experiment	-
$(\cdot)^*$	indicates the conjugate transpose	-
$(\cdot)^\star$	indicates optimality of (intermediate) solution	-
$t$	continuous time index	s
$\text{t}$	denotes correspondence to a transmitter	-
$T$	period of time, e.g. observation time	s
$T_s$	sample period	s
$\tau$	delay or integration variable	s
$\theta$	polar angle	rad
$(\cdot)^\text{T}$	indicates the matrix transpose	-
$\mathbf{v}$	vector whose elements are the kernel coefficients of all volterra operators up to $q$ -th order without repetition of symmetric elements	-
$u_q$	kernel of $q$ -th order volterra operator of the nonlinear post-equalizer with repetition of symmetric elements	-
$\mathbf{u}_q$	vector whose elements are the kernel coefficients of the $q$ -th order volterra operator of the nonlinear post-equalizer without repetition of symmetric elements	-
$v_q$	kernel of $q$ -th order volterra operator of the nonlinear post-equalizer without repetition of symmetric elements	-
$U_q\{\cdot\}$	$q$ -th order volterra operator of the nonlinear post-equalizer	-
$\mathbf{v}$	vector whose elements are the kernel coefficients of all volterra operators up to $q$ -th order without repetition of symmetric elements	-
$v_q$	kernel of $q$ -th order volterra operator without repetition of symmetric elements	-
$v_q$	kernel of $q$ -th order volterra operator with repetition of symmetric elements	-

Symbol	Description	Unit
$\mathbf{v}_q$	vector whose elements are the kernel coefficients of the $q$ -th order volterra operator without repetition of symmetric elements	-
$v_q\{\cdot\}$	$q$ -th order volterra operator	-
$\nu_{\text{ph}}$	optical frequency ascribed to a photon	Hz
$x(t)$	transmit signal in continuous time-domain	-
$x[k]$	transmit signal in discrete time-domain	-
$\mathbf{x}$	vector whose elements are the samples of a transmit signal in discrete time-domain	-
$x_{n,i}[k]$	$i$ -th sinusoid generated by the $n$ -th transmitter in discrete time-domain	-
$X(f)$	transmit signal in continuous frequency-domain	-
$X[l]$	transmit signal in discrete frequency-domain	-
$\mathbf{X}$	vector whose elements are the samples of a transmit signal in discrete frequency-domain	-
$X_{n,i}[l]$	$i$ -th sinusoid generated by the $n$ -th transmitter in discrete frequency-domain	-
$y(t)$	receive signal out contoutuous time-domain	-
$y[k]$	receive signal in discrete time-domain	-
$\mathbf{y}$	vector whose elements are the samples of a receive signal in discrete time-domain	-
$Y(f)$	receive signal out contoutuous frequency-domain	-
$Y[l]$	receive signal in discrete frequency-domain	-
$\mathbf{Y}$	vector whose elements are the samples of a receive signal in discrete frequency-domain	-



## BIBLIOGRAPHY

---

- [1] F. R. Gfeller and U. Bapst, "Wireless In-House Data Communication via Diffuse Infrared Radiation," *Proc. IEEE*, vol. 67, no. 11, pp. 1474–1486, Nov. 1979.
- [2] J. M. Kahn and J. R. Barry, "Wireless Infrared Communications," *Proc. IEEE*, vol. 85, no. 2, pp. 265–298, Feb. 1997.
- [3] D. Wisely and I. Neild, "A 100 Mbit/s tracked optical wireless telepoint," in *IEEE International Symposium on Personal, Indoor and Mobile Radio Communications (PIMRC)*, IEEE, Helsinki, Finland, Sep. 1997, pp. 964–968.
- [4] G. Yun and M. Kavehrad, "Spot-diffusing and fly-eye receivers for indoor infrared wireless communications," in *IEEE International Conference on Selected Topics in Wireless Communications*, Vancouver, 1992.
- [5] S. T. Jivkova and M. Kavehrad, "Multispot diffusing configuration for wireless infrared access: Joint optimization of multibeam transmitter and angle diversity receiver," in *Proc. SPIE 3850, Optical Wireless Communications II*, International Society for Optics and Photonics, Dec. 1999, pp. 72–78.
- [6] —, "Multispot diffusing configuration for wireless infrared access," *IEEE Trans. Commun.*, vol. 48, no. 6, pp. 970–978, Jun. 2000.
- [7] V. Jungnickel, A. Forck, T. Haustein, U. Krüger, V. Pohl, and C. von Helmolt, "Electronic Tracking for Wireless Infrared Communications," *IEEE Trans. Wireless Commun.*, vol. 2, no. 5, pp. 989–999, Sep. 2003.
- [8] S. Nakamura, T. Mukai, and M. Senoh, "Candela-class high-brightness InGaN/AlGaIn double-heterostructure blue-light-emitting diodes," *Appl. Phys. Lett.*, vol. 64, no. 13, pp. 1687–1689, Mar. 1994.
- [9] J. S. Kim, P. E. Jeon, Y. H. Park, J. C. Choi, H. L. Park, G. C. Kim, and T. W. Kim, "White-light generation through ultraviolet-emitting diode and white-emitting phosphor," *Applied Physics Letters*, vol. 85, no. 17, pp. 3696–3698, Oct. 2004.
- [10] T. Komine and M. Nakagawa, "Fundamental Analysis for Visible Light Communication System using LED Lights," *IEEE Trans. Consum. Electron.*, vol. 50, no. 1, pp. 100–107, 2004.
- [11] J. Vucic, C. Kottke, K. Habel, and K.-D. Langer, "803 Mbit/s Visible Light WDM Link based on DMT Modulation of a Single RGB LED Luminary," in *Optical Fiber Communication Conference/National Fiber Optic Engineers Conference (OFC/NFOEC)*, Los Angeles, 2011.

- [12] G. Cossu, A. M. Khalid, P. Choudhury, R. Corsini, and E. Ciaramella, "2.1 Gbit/s visible optical wireless transmission," in *European Conference and Exhibition on Optical Communication (ECOC)*, Amsterdam, Netherlands, 2012.
- [13] G. Cossu, A. Wajahat, R. Corsini, and E. Ciaramella, "5.6 Gbit/s downlink and 1.5 Gbit/s uplink optical wireless transmission at indoor distances ( $>1.5$  m)," in *European Conference on Optical Communication (ECOC)*, IEEE, Cannes, France, Sep. 2014.
- [14] Y. Wang, L. Tao, X. Huang, J. Shi, and N. Chi, "Enhanced Performance of a High-Speed WDM CAP64 VLC System Employing Volterra Series-Based Nonlinear Equalizer," *IEEE Photonics J.*, vol. 7, no. 3, pp. 1–7, 2015.
- [15] H. Le Minh, D. O'Brien, G. Faulkner, O. Bouchet, M. Wolf, L. Grobe, and J. Li, "A 1.25-Gb/s indoor cellular optical wireless communications demonstrator," *IEEE Photon. Technol. Lett.*, vol. 22, no. 21, pp. 1598–1600, Nov. 2010.
- [16] T. Borogovac and T. D. C. Little, "Laser visible light communications," in *IEEE Photonics Society Summer Topical Meeting Series*, Seattle, WA, USA, Jul. 2012, pp. 117–118.
- [17] D. Tsonev, S. Videv, and H. Haas, "Towards a 100 Gb/s visible light wireless access network," *Opt. Express*, vol. 23, no. 2, pp. 1627–1637, Jan. 2015.
- [18] J. J. D. McKendry, R. P. Green, A. E. Kelly, Z. Gong, B. Guilhabert, D. Massoubre, E. Gu, and M. D. Dawson, "High-speed visible light communications using individual pixels in a micro light-emitting diode array," *IEEE Photon. Technol. Lett.*, vol. 22, no. 18, pp. 1346–1348, Sep. 2010.
- [19] H. Chun, P. Manousiadis, S. Rajbhandari, D. A. Vithanage, G. Faulkner, D. Tsonev, J. J. D. McKendry, S. Videv, E. Xie, E. Gu, M. D. Dawson, H. Haas, G. A. Turnbull, I. D. W. Samuel, and D. C. O'Brien, "Visible Light Communication Using a Blue GaN  $\mu$ LED and Fluorescent Polymer Color Converter," *IEEE Photon. Technol. Lett.*, vol. 26, no. 20, pp. 2035–2038, 2014.
- [20] D. Tsonev, H. Chun, S. Rajbhandari, J. J. D. McKendry, S. Videv, E. Gu, M. Haji, S. Watson, A. E. Kelly, G. Faulkner, M. D. Dawson, H. Haas, and D. O'Brien, "A 3-Gb/s single-LED OFDM-based wireless VLC link using a gallium nitride  $\mu$ LED," *IEEE Photon. Technol. Lett.*, vol. 26, no. 7, pp. 637–640, Apr. 2014.
- [21] S. Rajbhandari, A. V. N. Jalajakumari, H. Chun, G. Faulkner, K. Cameron, R. Henderson, D. Tsonev, H. Haas, E. Xie, J. J. D. McKendry, J. Herrnsdorf, R. Ferreira, E. Gu, M. D. Dawson, and D. O'Brien, "A multigigabit per second integrated multiple-input multiple-output VLC demonstrator," *J. Lightw. Technol.*, vol. 35, no. 20, pp. 4358–4365, Oct. 2017.

- [22] Y. Tanaka, T. Komine, S. Haruyama, and M. Nakagawa, "Indoor visible communication utilizing plural white LEDs as lighting," in *IEEE International Symposium on Personal, Indoor and Mobile Radio Communications (PIMRC)*, vol. 2, San Diego, CA, USA, Sep. 2001, F81–85.
- [23] J. Grubor, V. Jungnickel, K.-D. Langer, and C. Von Helmolt, "Dynamic data-rate adaptive signal processing method in a wireless infra-red data transfer system," 8,831,427, Sep. 2014.
- [24] J. Grubor, V. Jungnickel, and K.-D. Langer, "Rate-adaptive multiple-subcarrier-based transmission for broadband infrared wireless communication," in *Optical Fiber Communication Conference/National Fiber Optic Engineers Conference (OFC/NFOEC)*, Optical Society of America, Anaheim, CA, USA, Mar. 2006.
- [25] O. González, R. Pérez-Jiménez, S. Rodríguez, J. Rabadán, and A. Ayala, "OFDM over indoor wireless optical channel," *IEE P.-Optoelectron.*, vol. 152, no. 4, pp. 199–204, Aug. 2005.
- [26] —, "Adaptive OFDM system for communications over the indoor wireless optical channel," *IEE P.-Optoelectron.*, vol. 153, no. 4, pp. 139–144, Aug. 2006.
- [27] M. Z. Afgani, H. Haas, H. Elgala, and D. Knipp, "Visible Light Communication Using OFDM," in *International Conference on Testbeds and Research Infrastructures for the Development of Networks and Communities (TRIDENTCOM)*, Barcelona, 2006.
- [28] S. Hranilovic and F. R. Kschischang, "Optical Intensity-Modulated Direct Detection Channels: Signal Space and Lattice Codes," *IEEE Trans. Inf. Theory*, vol. 49, no. 6, pp. 1385–1399, Jun. 2003.
- [29] W. Mao and J. M. Kahn, "Lattice codes for amplified direct-detection optical systems," *IEEE Trans. Commun.*, vol. 56, no. 7, pp. 1137–1145, Jul. 2008.
- [30] J. Karout, G. Kramer, F. R. Kschischang, and E. Agrell, "A two-dimensional signal space for intensity-modulated channels," *IEEE Commun. Lett.*, vol. 16, no. 9, pp. 1361–1364, Sep. 2012.
- [31] F.-M. Wu, C.-T. Lin, C.-C. Wei, C.-W. Chen, Z.-Y. Chen, and K. Huang, "3.22-Gb/s WDM visible light communication of a single RGB LED employing carrier-less amplitude and phase modulation," in *Optical Fiber Communication Conference/National Fiber Optic Engineers Conference (OFC/NFOEC)*, no. OTh1G.4, Optical Society of America, Anaheim, CA, USA, Mar. 2013.
- [32] Y. Wang, X. Huang, J. Zhang, Y. Wang, and N. Chi, "Enhanced performance of visible light communication employing 512-QAM N-SC-FDE and DD-LMS," *Opt. Express*, vol. 22, no. 13, pp. 15 328–15 334, Jun. 2014.
- [33] D. Zhang and S. Hranilovic, "Bandlimited optical intensity modulation under average and peak power constraints," *IEEE Trans. Commun.*, vol. 64, no. 9, pp. 3820–3830, Sep. 2016.

- [34] J. Armstrong and A. J. Lowery, "Power efficient optical OFDM," *Electron. Lett.*, vol. 42, no. 6, pp. 370–372, 2006.
- [35] N. Fernando, Y. Hong, and E. Viterbo, "Flip-OFDM for unipolar communication systems," *IEEE Trans. Commun.*, vol. 60, no. 12, pp. 3726–3733, 2012.
- [36] D. Tsonev, S. Sinanović, and H. Haas, "Novel unipolar orthogonal frequency division multiplexing (U-OFDM) for optical wireless," in *IEEE Vehicular Technology Conference (VTC Spring)*, Yokohama, 2012.
- [37] D. Tsonev, S. Videv, and H. Haas, "Light fidelity (Li-Fi): Towards all-optical networking," in *Proc. SPIE 9007, Broadband Access Communication Technologies VIII*, Feb. 2014, pp. 900702.1–10.
- [38] A. Lapidoth and S. M. Moser, "On the capacity of the discrete-time poisson channel," *IEEE Trans. Inf. Theory*, vol. 55, no. 1, pp. 303–322, Jan. 2009.
- [39] A. Lapidoth, S. M. Moser, and M. A. Wigger, "On the capacity of free-space optical intensity channels," *IEEE Trans. Inf. Theory*, vol. 55, no. 10, pp. 4449–4461, Oct. 2009.
- [40] S. M. Moser, "Capacity results of an optical intensity channel with input-dependent gaussian noise," *IEEE Trans. Inf. Theory*, vol. 58, no. 1, pp. 207–223, 2012.
- [41] V. Jungnickel, M. Uysal, N. Serafimovski, T. Baykas, D. O'Brien, E. Ciaramella, Z. Ghassemlooy, R. Green, H. Haas, P. A. Haigh, V. P. Gil Jimenez, F. Miramirkhani, M. Wolf, and S. Zvánovec, "A European View on the Next Generation Optical Wireless Communication Standard," in *2015 IEEE Conference on Standards for Communications and Networking (CSCN)*, Tokyo, Japan, 2015, pp. 106–111.
- [42] T. Koonen, "Optical wireless systems: Technology, trends and applications," *J. Lightw. Technol.*, vol. 36, no. 8, pp. 1459–1467, Apr. 2018.
- [43] D. Schulz, P. Wilke Berenguer, J. Hilt, P. Hellwig, A. Paraskevopoulos, R. Freund, and V. Jungnickel, "Use cases for optical wireless communication," in *Optical Fiber Communications Conference and Exposition (OFC)*, no. M1F.3, San Diego, CA, USA, Mar. 2018.
- [44] J. Hou and D. O'Brien, "Vertical handover-decision-making algorithm using fuzzy logic for the integrated radio-and-OW system," *IEEE Trans. Wireless Commun.*, vol. 5, no. 1, pp. 176–185, Jan. 2006.
- [45] S. Shao, A. Khreishah, M. Ayyash, M. B. Rahaim, H. Elgala, V. Jungnickel, D. Schulz, T. D. C. Little, J. Hilt, and R. Freund, "Design and Analysis of a Visible-Light-Communication Enhanced WiFi System," *J. Opt. Commun. Netw.*, vol. 7, no. 10, pp. 960–973, Oct. 2015.
- [46] *Industrial communication networks - fieldbus specifications - part 1: Overview and guidance for the IEC 61158 and IEC 61784 series*, IEC Specification 61158, May 2014.

- [47] 5G PPP, “5G and the factories of the future,” 5G PPP, Tech. Rep., Oct. 2015, White Paper.
- [48] F. De Pellegrini, D. Miorandi, S. Vitturi, and A. Zanella, “On the use of wireless networks at low level of factory automation systems,” *IEEE Trans. Ind. Informat.*, vol. 2, no. 2, pp. 129–143, May 2006.
- [49] M. Weiner, M. Jorgovanovic, A. Sahai, and B. Nikolić, “Design of a low-latency, high-reliability wireless communication system for control applications,” in *IEEE International Conference on Communications (ICC)*, IEEE, Sydney, Australia, Jun. 2014, pp. 3829–3835.
- [50] P. Fite-Georgel, “Is there a reality in industrial augmented reality?” In *IEEE International Symposium on Mixed and Augmented Reality (ISMAR)*, IEEE, Basel, Switzerland, Oct. 2011, pp. 201–210.
- [51] M. Schneider, J. Rambach, and D. Stricker, “Augmented reality based on edge computing using the example of remote live support,” in *IEEE International Conference on Industrial Technology (ICIT)*, IEEE, Toronto, Canada, Mar. 2017, pp. 1277–1282.
- [52] L. Thames and D. Schaefer, “Software-defined cloud manufacturing for industry 4.0,” *Procedia CIRP*, vol. 52, pp. 12–17, 2016.
- [53] D. Wesemann, S. Witte, A. Schmelter, and R. Heß, “Flexible factory automation: Potentials of contactless transmission systems, combining state-of-the-art technologies,” in *IEEE World Conference on Factory Communication Systems (WFCS)*, IEEE, Aveiro, Portugal, May 2016.
- [54] (2017). Plattform industrie 4.0. 04-Jul-2017, [Online]. Available: <http://www.plattform-i40.de/I40/Navigation/EN/Home/home.html>.
- [55] (2017). Industrial internet consortium. 04-Jul-2017, [Online]. Available: <http://www.iiconsortium.org/>.
- [56] *Industrial networks - wireless communication network and communication profiles - WirelessHART™*, IEC Specification 62591, Mar. 2016.
- [57] *Industrial networks - wireless communication network and communication profiles - ISA 100.11a*, IEC Specification 62734, Oct. 2014.
- [58] P. Wu and N. Jindal, “Coding versus ARQ in fading channels: How reliable should the PHY be?” *IEEE Trans. Commun.*, vol. 59, no. 12, pp. 3363–3374, Dec. 2011.
- [59] A. Willig, “Redundancy concepts to increase transmission reliability in wireless industrial LANs,” *IEEE Trans. Ind. Informat.*, vol. 1, no. 3, pp. 173–182, Aug. 2005.
- [60] —, “How to exploit spatial diversity in wireless industrial networks,” *Annual Reviews in Control*, vol. 32, no. 1, pp. 49–57, Apr. 2008.

- [61] C. Dombrowski and J. Gross, "EchoRing: A low-latency, reliable token-passing MAC protocol for wireless industrial networks," in *European Wireless Conference*, VDE, Budapest, Hungary, May 2015, pp. 342–349.
- [62] A. Lozano and N. Jindal, "Transmit diversity vs. spatial multiplexing in modern MIMO systems," *IEEE Trans. Wireless Commun.*, vol. 9, no. 1, pp. 186–197, Jan. 2010.
- [63] B. Holfeld, D. Wieruch, T. Wirth, L. Thiele, S. A. Ashraf, J. Huschke, I. Aktas, and J. Ansari, "Wireless communication for factory automation: An opportunity for LTE and 5G systems," *IEEE Commun. Mag.*, vol. 54, no. 6, pp. 36–43, Jun. 2016.
- [64] A. Lessard and M. Gerla, "Wireless communications in the automated factory environment," *IEEE Netw.*, vol. 2, no. 3, pp. 64–69, May 1988.
- [65] A. Willig, K. Matheus, and A. Wolisz, "Wireless technology in industrial networks," *Proc. IEEE*, vol. 93, no. 6, pp. 1130–1151, Jun. 2005.
- [66] Cree. (2018). Cree XLamp XP-E LEDs, [Online]. Available: <http://www.cree.com/led-components/media/documents/XLampXPE.pdf>.
- [67] Osram. (Aug. 2016). SFH 4715AS IR LED, [Online]. Available: [https://dammedia.osram.info/media/resource/hires/osram-dam-5580411/SFH%204715AS\\_EN.pdf](https://dammedia.osram.info/media/resource/hires/osram-dam-5580411/SFH%204715AS_EN.pdf).
- [68] Hamamatsu. (2018). Hamamatsu S6801, S6968 Si PIN photodiodes, [Online]. Available: [http://www.hamamatsu.com/resources/pdf/ssd/s6801\\_etc\\_kpin1046e.pdf](http://www.hamamatsu.com/resources/pdf/ssd/s6801_etc_kpin1046e.pdf).
- [69] A. J. C. Moreira, R. T. Valadas, and A. M. de Oliveira Duarte, "Optical interference produced by artificial light," *Wireless Networks*, vol. 3, no. 2, pp. 131–140, May 1997.
- [70] J. Vučić, "Adaptive Modulation Technique for Broadband Communication in Indoor Optical Wireless Systems," Ph.D. dissertation, Technische Universität Berlin, Berlin, 2009.
- [71] E. F. Zalewski, "Handbook of optics," in M. Bass, Ed., 2nd ed. MacGraw-Hill, Inc., 1995, vol. 2, ch. Radiometry and Photometry, pp. 24.3–24.51.
- [72] J. R. Barry and J. M. Kahn, "Link design for nondirected wireless infrared communications," *Appl. Opt.*, vol. 34, no. 19, pp. 3764–3776, Jul. 1995.
- [73] K.-P. Ho and J. M. Kahn, "Compound parabolic concentrators for narrowband wireless infrared receivers," *Opt. Eng.*, vol. 34, no. 5, pp. 1385–1396, May 1995.
- [74] J. B. Carruthers and J. M. Kahn, "Angle diversity for nondirected wireless infrared communication," *IEEE Trans. Commun.*, vol. 48, no. 6, pp. 960–969, Jun. 2000.

- [75] Hamamatsu. (2018). Hamamatsu S2506, S26775, S6967 Si PIN photodiodes, [Online]. Available: [http://www.hamamatsu.com/resources/pdf/ssd/s2506-02\\_etc\\_kpin1048e.pdf](http://www.hamamatsu.com/resources/pdf/ssd/s2506-02_etc_kpin1048e.pdf).
- [76] A. V. Oppenheim, R. W. Schaefer, and J. R. Buck, *Discrete-time signal processing*, 2nd ed., M. Horton, Ed. Upper Saddle River, New Jersey: Prentice-Hall, Inc., 1999.
- [77] S. H. Y. Wong, H. Yang, S. Lu, and V. Bharghavan, "Robust rate adaptation for 802.11 wireless networks," in *12th Annual International Conference on Mobile Computing and Networking (MobiCom)*, Los Angeles, CA, USA, Sep. 2006, pp. 146–157.
- [78] I. Haratcherev, K. Langendoen, R. Lagendijk, and H. Sips, "Hybrid rate control for IEEE 802.11," in *2nd International Workshop on Mobility Management and Wireless Access Protocols*, Philadelphia, PA, USA, Oct. 2004, pp. 10–18.
- [79] L. Deek, E. Garcia-Villegas, E. Belding, S.-J. Lee, and K. Almeroth, "A practical framework for 802.11 MIMO rate adaptation," *Computer Networks*, vol. 83, pp. 332–348, Apr. 2015.
- [80] J. Zhang, X. Zhang, and G. Wu, "Dancing with light: Predictive in-frame rate selection for visible light networks," in *IEEE Conference on Computer Communications (INFOCOM)*, IEEE, Kowloon, Hong Kong, Apr. 2015, pp. 2434–2442.
- [81] J. B. Carruthers and J. M. Kahn, "Modeling of nondirected wireless infrared channels," *IEEE Transactions on Communications*, vol. 45, no. 10, pp. 1260–1268, Oct. 1997.
- [82] V. Pohl, V. Jungnickel, and C. Von Helmolt, "A channel model for wireless infrared communication," in *IEEE International Symposium on Personal, Indoor and Mobile Radio Communications (PIMRC)*, London, UK, United Kingdom, Sep. 2000, pp. 297–303.
- [83] V. Jungnickel, V. Pohl, S. Nönning, and C. von Helmolt, "A Physical Model of the Wireless Infrared Communication Channel," *IEEE J. Sel. Areas Commun.*, vol. 20, no. 3, pp. 631–640, Apr. 2002.
- [84] J. Grubor, V. Jungnickel, and K.-D. Langer, "Capacity analysis in indoor wireless infrared communication using adaptive multiple subcarrier transmission," in *2005 7th International Conference on Transparent Optical Networks (ICTON)*, IEEE, Barcelona, Spain, Jul. 2005, pp. 171–174.
- [85] H. Schulze, "Frequency-Domain Simulation of the Indoor Wireless Optical Communication Channel," *IEEE Trans. Commun.*, vol. 64, no. 6, pp. 2551–2562, Jun. 2016.
- [86] J. R. Barry, J. M. Kahn, W. J. Krause, E. A. Lee, and D. G. Messerschmitt, "Simulation of multipath impulse response for indoor wireless optical channels," *IEEE J. Sel. Areas Commun.*, vol. 11, no. 3, pp. 367–379, Apr. 1993.
- [87] J. B. Carruthers and P. Kannan, "Iterative site-based modeling for wireless infrared channels," *IEEE Trans. Antennas Propag.*, vol. 50, no. 5, pp. 759–765, May 2002.

- [88] J. B. Carruthers, S. M. Carroll, and P. Kannan, "Propagation modelling for indoor optical wireless communications using fast multi-receiver channel estimation," *IEE P.-Optoelectron.*, vol. 150, no. 5, pp. 473–481, Oct. 2003.
- [89] Y. A. Alqudah and M. Kavehrad, "MIMO characterization of indoor wireless optical link using a diffuse-transmission configuration," *IEEE Trans. Commun.*, vol. 51, no. 9, pp. 1554–1560, Sep. 2003.
- [90] K. Lee, H. Park, and J. R. Barry, "Indoor Channel Characteristics for Visible Light Communications," *IEEE Commun. Lett.*, vol. 15, no. 2, pp. 217–219, Feb. 2011.
- [91] V. Pohl, V. Jungnickel, and C. Von Helmolt, "Integrating-sphere diffuser for wireless infrared communication," *IEE P.-Optoelectron.*, vol. 147, no. 4, pp. 281–285, Aug. 2000.
- [92] F. J. Lopez-Hernandez, R. Perez-Jimenez, and A. Santamaria, "Ray-tracing algorithms for fast calculation of the channel impulse response on diffuse IR wireless indoor channels," *Opt. Eng.*, vol. 39, no. 10, pp. 2775–2781, Oct. 2000.
- [93] S. Rodríguez Pérez, R. Pérez Jiménez, F. J. López Hernández, O. B. González Hernández, and A. J. Ayala Alfonso, "Reflection model for calculation of the impulse response on IR-wireless indoor channels using ray-tracing algorithm," *Microwave Opt. Technol. Lett.*, vol. 32, no. 4, pp. 296–300, Feb. 2002.
- [94] S. Rodríguez Pérez, R. Pérez Jiménez, B. Rodríguez Mendoza, F. J. López Hernández, and A. J. Ayala Alfonso, "Simulation of impulse response for indoor visible light communications using 3D CAD models," *EURASIP Journal on Wireless Communications and Networking*, vol. 2013, no. 7, Nov. 2013.
- [95] M. Uysal, T. Baykas, F. Miramirkhani, N. Serafimovski, and V. Jungnickel. (Sep. 2015). TG7r1 channel model document for high-rate PD communications, [Online]. Available: <https://mentor.ieee.org/802.15/dcn/15/15-15-0746-01-007a-tg7r1-channel-model-documentfor-high-rate-pd-communications.pdf>.
- [96] —, (Sep. 2015). TG7r1 CIRs channel model document for high-rate PD communications, [Online]. Available: <https://mentor.ieee.org/802.15/dcn/15/15-15-0747-00-007a-tg7r1-cirs-channel-model-document-for-high-rate-pd-communications.zip>.
- [97] J. M. Kahn, W. J. Krause, and J. B. Carruthers, "Experimental characterization of non-directed indoor infrared channels," *IEEE Trans. Commun.*, vol. 43, no. 2/3/4, pp. 1613–1623, 1995.
- [98] *Unified high-speed wireline-based home networking transceivers – system architecture and physical layer specification*, ITU-T Recommendation G.9960, 2015.
- [99] J. G. Smith, "Odd-bit quadrature amplitude-shift keying," *IEEE Trans. Commun.*, vol. 23, no. 3, pp. 385–389, Mar. 1975.

- [100] J. Proakis, *Digital Communications*, 4th ed. McGrawHill, 2000, p. 1024.
- [101] S. Haykin, *Communication systems*, 4th ed., B. Zobrist, Ed. John Wiley & Sons, 2001.
- [102] H. Minn, V. K. Bhargava, and K. B. Letaief, "A Robust Timing and Frequency Synchronization for OFDM Systems," *IEEE Trans. Wireless Commun.*, vol. 2, no. 4, pp. 822–839, Jul. 2003.
- [103] K.-D. Kammeyer, "Nachrichtenübertragung," in H. Wollstadt, Ed., 4th ed. Wiesbaden, Germany: Vieweg+Teubner Verlag, 2008, ch. 16 Mehrträger-Modulation, pp. 581–635.
- [104] S. Schiffermüller and V. Jungnickel, "Practical Channel Interpolation for OFDMA," in *IEEE Global Communications Conference (GLOBECOM)*, San Francisco, Dec. 2006.
- [105] B. S. Krongold, K. Ramchandran, and D. L. Jones, "Computationally efficient optimal power allocation algorithms for multicarrier communication systems," *IEEE Trans. Commun.*, vol. 48, no. 1, pp. 23–27, 2000.
- [106] D. C. Chu, "Polyphase codes with good periodic correlation properties (corresp.)," *IEEE Trans. Inf. Theory*, vol. 18, no. 4, pp. 531–532, Jul. 1972.
- [107] K.-D. Kammeyer, "Nachrichtenübertragung," in H. Wollstadt, Ed., 4th ed. Wiesbaden, Germany: Vieweg+Teubner Verlag, 2008, ch. 14 Kanalschätzung, pp. 519–557.
- [108] —, "Nachrichtenübertragung," in H. Wollstadt, Ed., 4th ed. Wiesbaden, Germany: Vieweg+Teubner Verlag, 2008, ch. 12 Entzerrung, pp. 397–481.
- [109] T. Pfau, S. Hoffmann, and R. Noe, "Hardware-Efficient Coherent Digital Receiver Concept With Feedforward Carrier Recovery for M-QAM Constellations," *J. Lightw. Technol.*, vol. 27, no. 8, pp. 989–999, Apr. 2009.
- [110] K. Asatani and T. Kimura, "Analyses of LED nonlinear distortions," *IEEE J. Solid-State Circuits*, vol. SC-13, no. 1, pp. 125–133, Feb. 1978.
- [111] —, "Linearization of LED Nonlinearity by Predistortions," *IEEE J. Solid-State Circuits*, vol. SC-13, no. 1, pp. 133–138, Feb. 1978.
- [112] R. Mesleh, H. Elgala, and H. Haas, "LED nonlinearity mitigation techniques in optical wireless OFDM communication systems," *IEEE J. Opt. Commun. Netw.*, vol. 4, no. 11, pp. 865–875, Nov. 2012.
- [113] H. Elgala, R. Mesleh, and H. Haas, "Predistortion in optical wireless transmission using OFDM," in *International Conference on Hybrid Intelligent Systems (HIS)*, Shenyang, China, Aug. 2009, pp. 184–189.
- [114] H. Elgala, "A Study on the Impact of Nonlinear Characteristics of LEDs on Optical OFDM," Ph.D. dissertation, School of Engineering and Science, Jacobs University, Bremen, 2010.

- [115] X. Deng, S. Mardanikorani, Y. Wu, K. Arulandu, B. Chen, A. M. Khalid, and J.-P. M. G. Linnartz, "Mitigating LED nonlinearity to enhance visible light communications," *IEEE Trans. Commun.*, vol. 66, no. 11, pp. 5593–5607, Nov. 2018.
- [116] G. Stepniak, J. Siuzdak, and P. Zwierko, "Compensation of a VLC Phosphorescent White LED Nonlinearity by Means of Volterra DFE," *IEEE Photon. Technol. Lett.*, vol. 25, no. 16, pp. 1597–1600, Aug. 2013.
- [117] H. Qian, S. J. Yao, S. Z. Cai, and T. Zhou, "Adaptive postdistortion for nonlinear LEDs in visible light communications," *IEEE Photonics J.*, vol. 6, no. 4, p. 7901508, Aug. 2014, no. 7901508.
- [118] P. Wilke Berenguer, P. Hellwig, D. Schulz, J. Hilt, G. Kleinpeter, J. K. Fischer, and V. Jungnickel, "Real-time optical wireless mobile communication with high physical layer reliability," *J. Lightw. Technol.*, vol. 37, no. 6, pp. 1638–1646, Mar. 2019.
- [119] M. Schetzen (1980), *The Volterra and Wiener Theories of Nonlinear Systems*, Reprint. Malabar, Florida: Krieger Publishing Company, 2006.
- [120] S.-W. Nam and E. J. Powers, "Application of higher order spectral analysis to cubically nonlinear system identification," *IEEE Trans. Signal Process.*, vol. 42, no. 7, pp. 1746–1765, Jul. 1994.
- [121] M. J. Korenberg and I. W. Hunter, "The identification of nonlinear biological systems: Volterra kernel approaches," *Ann. Biomed. Eng.*, vol. 24, no. 4, pp. 250–268, 1996.
- [122] R. D. Nowak, "Volterra filter identification using penalized least squares," in *IEEE International Conference on Acoustics, Speech, and Signal Processing (ICASSP)*, Atlanta, USA, May 1996, pp. 2813–2816.
- [123] —, "Penalized Least Squares Estimation of Volterra Filters and Higher Order Statistics," *IEEE Trans. Signal Process.*, vol. 46, no. 2, pp. 419–428, Feb. 1998.
- [124] E. Aschbacher, M. Steinmair, and M. Rupp, "Iterative linearization methods suited for digital pre-distortion of power amplifiers," in *Asilomar Conference on Signals, Systems and Computers*, Pacific Grove, CA, USA, Nov. 2004, pp. 2198–2202.
- [125] R. D. Nowak and B. D. Van Veen, "Tensor product basis approximations for volterra filters," *IEEE Trans. Signal Process.*, vol. 44, no. 1, pp. 36–50, Jan. 1996.
- [126] D. G. Luenberger and Y. Ye, "Linear and nonlinear programming," in F. S. Hillier, Ed., 3rd ed. New York: Springer Science + Business Media, 2008, ch. 13 Penalty and Barrier Methods, pp. 401–435.
- [127] P. Wilke Berenguer, V. Jungnickel, and J. K. Fischer, "The benefit of frequency-selective rate adaptation for optical wireless communications," in *2016 10th International Symposium on Communication Systems, Networks and Digital Signal Processing (CSNDSP)*, Prague, Jun. 2016.

- [128] P. Wilke Berenguer, D. Schulz, J. Hilt, P. Hellwig, G. Kleinpeter, J. K. Fischer, and V. Jungnickel, "Optical wireless MIMO experiments in an industrial environment," *IEEE J. Sel. Areas Commun.*, vol. 36, no. 1, pp. 185–193, Jan. 2018.
- [129] G. D. Durgin, T. S. Rappaport, and D. A. De Wolf, "New analytical models and probability density functions for fading in wireless communications," *IEEE Trans. Commun.*, vol. 50, no. 6, pp. 1005–1015, Jun. 2002.
- [130] T. Chen, Z. Zhen, L. Liu, and W. Hu, "High-Diversity Space Division Multiplexing Visible Light Communication Utilizing a Fisheye-Lens-Based Imaging Receiver," in *Optical Fiber Communication Conference (OFC)*, Los Angeles, CA, USA, 2015, Tu2G.3.
- [131] J. Shi, X. Huang, Y. Wang, L. Tao, and N. Chi, "Improved Performance of a high speed 2 x 2 MIMO VLC network Based on EGC-STBC," in *European Conference and Exhibition on Optical Communication (ECOC)*, Valencia, Spain, 2015, Th.2.3.3.
- [132] A. Willig, "Recent and emerging topics in wireless industrial communications: A selection," *IEEE Trans. Ind. Inf.*, vol. 4, no. 2, pp. 102–124, May 2008.
- [133] *Digital Video Broadcasting (DVB); framing structure, channel coding and modulation for digital terrestrial television*, ETSI Standard EN 300 744, Oct. 2015.
- [134] ETSI TR 101 190, "Digital Video Broadcasting (DVB); implementation guidelines for DVB terrestrial services; transmission aspects," ETSI, Tech. Rep., May 2011.
- [135] D. J. Love and R. W. Heath, "Equal gain transmission in multiple-input multiple-output wireless systems," *IEEE Trans. Commun.*, vol. 51, no. 7, pp. 1102–1110, Jul. 2003.
- [136] D. G. Luenberger and Y. Ye, *Linear and nonlinear programming*, 3rd ed., F. S. Hillier, Ed. New York: Springer Science + Business Media, 2008.
- [137] D. Hömberg, "Nichtlineare Optimierung," Technische Universität Berlin, lecture notes, Jun. 2016.
- [138] H. Ochiai and H. Imai, "Performance analysis of deliberately clipped OFDM signals," *IEEE Trans. Commun.*, vol. 50, no. 1, pp. 89–101, Jan. 2002.
- [139] H. Zhang, Y. Yuan, and W. Xu, "PAPR reduction for DCO-OFDM visible light communications via semidefinite relaxation," *IEEE Photon. Technol. Lett.*, vol. 26, no. 17, pp. 1718–1721, Sep. 2014.
- [140] D. G. Brennan, "Linear diversity combining techniques," *Proc. IRE*, vol. 47, no. 6, pp. 1075–1102, Jun. 1959.
- [141] Atmel. (Jun. 2011). Atmega128, [Online]. Available: <http://ww1.microchip.com/downloads/en/DeviceDoc/doc2467.pdf>.

- [142] *Unified high-speed wireline-based home networking transceivers – data link layer specification*, ITU-T Recommendation G.9961, 2015.
- [143] P. C. D. Hobbs, “Photodiode front ends: The real story,” *Optics and Photonics News*, vol. 12, no. 4, pp. 42–45, Apr. 2001.
- [144] (2018). 18-05-2018, Colour and Vision Research Laboratory, [Online]. Available: <http://www.cvrl.org/>.
- [145] J. A. Nelder and R. Mead, “A simplex method for function minimization,” *The Computer Journal*, vol. 7, no. 4, pp. 308–313, 1965.
- [146] J. C. Lagarias, J. A. Reeds, M. H. Wright, and P. E. Wright, “Convergence properties of the nelder–mead simplex method in low dimensions,” *SIAM J. Optim.*, vol. 9, no. 1, pp. 112–147, 1998.

## AUTHOR'S BIBLIOGRAPHY

---

- [PWB1] S. Alreesh, J. K. Fischer, P. Wilke Berenguer, and C. Schubert, "Blind adaptive equalization for 6PolSK-QPSK signals," in *European Conference and Exhibition on Optical Communication (ECOC)*, no. Mo.4.D.3, London, 2013.
- [PWB2] C. Schmidt-Langhorst, F. Frey, M. Nölle, R. Elschner, C. Meuer, P. Wilke Berenguer, and C. Schubert, "Optimization of subcarrier spacing of 400-Gb/s dual-carrier nyquist PDM-16QAM in a flex-grid scenario," in *European Conference and Exhibition on Optical Communication (ECOC)*, no. P.5.1, London, 2013.
- [PWB3] J. K. Fischer, C. Schmidt-Langhorst, S. Alreesh, R. Elschner, F. Frey, P. Wilke Berenguer, L. Molle, M. Nölle, and C. Schubert, "Transmission of 512SP-QAM Nyquist-WDM signals," in *European Conference on Optical Communication (ECOC)*, no. Tu.3.3.2, Cannes, France, 2014.
- [PWB4] S. Alreesh, C. Schmidt-Langhorst, R. Elschner, F. Frey, P. Wilke Berenguer, L. Molle, M. Nölle, C. Schubert, and J. K. Fischer, "Transmission of 2048SP-QAM Nyquist-WDM signals," in *16. ITG Symposium Photonic Networks*, Leipzig, Germany, May 2015, pp. 88–91.
- [PWB5] S. Alreesh, C. Schmidt-Langhorst, F. Frey, P. Wilke Berenguer, C. Schubert, and J. K. Fischer, "Transmission performance of 4D 128SP-QAM with forward error correction coding," *IEEE Photon. Technol. Lett.*, vol. 27, no. 7, pp. 744–747, Apr. 2015.
- [PWB6] T. A. Eriksson, S. Alreesh, C. Schmidt-Langhorst, F. Frey, P. Wilke Berenguer, C. Schubert, J. K. Fischer, P. A. Andrekson, M. Karlsson, and E. Agrell, "Experimental investigation of a four-dimensional 256-ary lattice-based modulation format," in *Optical Fiber Communication Conference (OFC)*, no. W4K.3, Los Angeles, 2015.
- [PWB7] J. K. Fischer, C. Schmidt-Langhorst, S. Alreesh, R. Elschner, F. Frey, P. Wilke Berenguer, L. Molle, M. Nölle, and C. Schubert, "Generation, transmission, and detection of 4-d set-partitioning qam signals," *J. Lightw. Technol.*, vol. 33, no. 7, pp. 1445–1451, Apr. 2015.
- [PWB8] P. Wilke Berenguer, T. Rahman, A. Napoli, M. Nölle, C. Schubert, and J. K. Fischer, "Nonlinear digital pre-distortion of transmitter components," in *European Conference on Optical Communication (ECOC)*, Valencia, Spain, Sep. 2015, Th.2.6.3.
- [PWB9] P. Wilke Berenguer, I. Sackey, C. Schubert, and J. K. Fischer, "Quantization of volterra kernel coefficients for reduced complexity nonlinear compensators," in *16. ITG Symposium Photonic Networks*, Leipzig, Germany, May 2015, pp. 162–166.

- [PWB10] A. Aimone, P. Wilke Berenguer, C. Meuer, M. Gruner, J. K. Fischer, C. Schubert, and M. Schell, "DAC-free 320 Gb/s 2-carrier Nyquist-space DP PAM-4 transmission by resonant InP MZM," *IEEE Photon. Technol. Lett.*, vol. 28, no. 7, pp. 775–777, Apr. 2016.
- [PWB11] S. Alreesh, C. Schmidt-Langhorst, R. Emmerich, P. Wilke Berenguer, C. Schubert, and J. K. Fischer, "Four-dimensional trellis coded modulation for flexible optical transponders," in *European Conference on Optical Communication (ECOC)*, no. W.1.C.4, Düsseldorf, 2016.
- [PWB12] L. Fernández del Rosal, K. Habel, S. Weide, P. Wilke Berenguer, V. Jungnickel, P. Farkas, and R. Freund, "Multi-gigabit real-time signal processing for future converged networks," in *10th ITG-Symposium Broadband Coverage in Germany*, VDE, Berlin, Germany, Apr. 2016, pp. 107–111.
- [PWB13] A. Napoli, T. Rahman, G. Khanna, P. Wilke Berenguer, B. Spinnler, S. Calabro, J. Fischer, and M. Bohn, "Digital pre-distortion techniques for next generation bandwidth variable transponders," in *Signal Processing in Photonic Communications (SPPCOM)*, Optical Society of America, Vancouver, Canada, Jul. 2016.
- [PWB14] P. Wilke Berenguer, V. Jungnickel, and J. K. Fischer, "The benefit of frequency-selective rate adaptation for optical wireless communications," in *2016 10th International Symposium on Communication Systems, Networks and Digital Signal Processing (CSNDSP)*, Prague, Jun. 2016.
- [PWB15] P. Wilke Berenguer, M. Nolle, L. Molle, T. Raman, A. Napoli, C. Schubert, and J. K. Fischer, "Nonlinear digital pre-distortion of transmitter components," *J. Lightw. Technol.*, vol. 34, no. 8, pp. 1739–1745, Apr. 2016.
- [PWB16] S. Alreesh, C. Schmidt-Langhorst, R. Emmerich, P. Wilke Berenguer, C. Schubert, and J. K. Fischer, "Four-dimensional trellis coded modulation for flexible optical communications," *J. Lightw. Technol.*, vol. 35, no. 2, pp. 152–158, Jan. 2017.
- [PWB17] M. Jazayerifar, I. Sackey, R. Elschner, T. Richter, L. Molle, P. Wilke Berenguer, C. Schubert, K. Jamshidi, and K. Petermann, "Impact of brillouin backscattering on signal distortions in single-fiber diversity loop based polarization-insensitive FOPAs," *J. Lightw. Technol.*, vol. 35, no. 19, pp. 4137–4144, Oct. 2017.
- [PWB18] A. Napoli, P. Wilke Berenguer, T. Rahman, G. Khanna, M. M. Mezghanni, L. Gardian, E. Riccardi, A. C. Piat, S. Calabrò, S. Dris, A. Richter, J. K. Fischer, B. Sommerkorn-Krombholz, and B. Spinnler, "Digital pre-compensation techniques enabling high-capacity bandwidth variable transponders," *Optics Communications*, vol. 409, pp. 52–65, Feb. 2017.

- [PWB19] P. Wilke Berenguer, D. Schulz, J. K. Fischer, and V. Jungnickel, "Distributed 8x6 MIMO experiments for optical wireless communications," in *European Conference and Exhibition on Optical Communication (ECOC)*, Gothenburg, Sweden, Sep. 2017, Tu.2.B.3.
- [PWB20] —, "Optical wireless communications in industrial production environments," in *IEEE Photonics Conference (IPC)*, Orlando, FL, USA, Oct. 2017, pp. 125–126.
- [PWB21] Z. Zheng, F. Frey, P. Wilke Berenguer, and J. K. Fischer, "Low-complexity equalization scheme for multicarrier offset-QAM systems," *IEEE Photon. Technol. Lett.*, vol. 29, no. 23, pp. 2075–2078, Dec. 2017.
- [PWB22] D. Schulz, P. Wilke Berenguer, J. Hilt, P. Hellwig, A. Paraskevopoulos, R. Freund, and V. Jungnickel, "Use cases for optical wireless communication," in *Optical Fiber Communications Conference and Exposition (OFC)*, no. M1F.3, San Diego, CA, USA, Mar. 2018.
- [PWB23] P. Wilke Berenguer, P. Hellwig, D. Schulz, J. Hilt, G. Kleinpeter, J. K. Fischer, and V. Jungnickel, "Real-time optical wireless communication: Field-trial in an industrial production environment," in *European Conference on Optical Communication (ECOC)*, Rome, Italy, Sep. 2018, Th.1.B.1.
- [PWB24] P. Wilke Berenguer, J. Hilt, P. Hellwig, D. Schulz, J. K. Fischer, and V. Jungnickel, "Analog antenna diversity for reliable optical wireless communication systems," in *Global LIFI Congress (GLC)*, IEEE, Paris, France, Feb. 2018.
- [PWB25] P. Wilke Berenguer, D. Schulz, J. Hilt, P. Hellwig, G. Kleinpeter, J. K. Fischer, and V. Jungnickel, "Optical wireless MIMO experiments in an industrial environment," *IEEE J. Sel. Areas Commun.*, vol. 36, no. 1, pp. 185–193, Jan. 2018.
- [PWB26] M. Düngen, T. Hansen, R. Croonenbroeck, R. Kays, B. Holfeld, D. Wieruch, P. Wilke Berenguer, V. Jungnickel, D. Block, U. Meier, and H. Schulze, "Channel measurement campaigns for wireless industrial automation," *at-Automatisierungstechnik*, vol. 67, no. 1, pp. 7–28, Jan. 2019.
- [PWB27] P. Wilke Berenguer, P. Hellwig, D. Schulz, J. Hilt, G. Kleinpeter, J. K. Fischer, and V. Jungnickel, "Real-time optical wireless mobile communication with high physical layer reliability," *J. Lightw. Technol.*, vol. 37, no. 6, pp. 1638–1646, Mar. 2019.